A MULTISCALE COMPUTATIONAL MODELING PLATFORM FOR DESIGN AND ANALYSIS OF ELECTRICAL NEURAL STIMULATION

by

Kyle Loizos

A dissertation submitted to the faculty of
The University of Utah
in partial fulfillment of the requirements for the degree of

Doctor of Philosophy

Department of Electrical and Computer Engineering

The University of Utah

May 2017

The University of Utah Graduate School

STATEMENT OF DISSERTATION APPROVAL

The dissertation of **Kyle Loizos**
has been approved by the following supervisory committee members:

Gianluca Lazzi ,	Chair(s)	**January 30, 2017** Date Approved
Christopher R. Butson ,	Member	**January 30, 2017** Date Approved
Ross M. Walker ,	Member	**January 30, 2017** Date Approved
Christopher R. Johnson ,	Member	**January 30, 2017** Date Approved
Florian Solzbacher ,	Member	**January 30, 2017** Date Approved

by **Gianluca Lazzi** , Chair/Dean of
the Department/College/School of **Electrical and Computer Engineering**
and by **David B. Kieda** , Dean of The Graduate School.

ABSTRACT

The goal of this work is to construct a simulation toolset for studying and improving neuroprosthetic devices for restoring neural functionality to patients with neural disorders or diseases. This involves the construction and validation of coupled electromagnetic-neural computational models of retina and hippocampus, compiling knowledge from a broad multidisciplinary background into a single computational platform, with features specific to implant electronics, bulk tissue, cellular and neural network behavior, and diseased tissue.

The application of a retina prosthetic device for restoring partial vision to patients blinded by degenerative diseases was first considered. This began with the conceptualization of the retina model, translating features of a connectome, implant electronics, and medical images into a computational model that was "degenerated." It was then applied to the design of novel electrode geometries towards increasing the resolution of induced visual percept, and of stimulation waveform shapes for increasing control of induced neural activity in diseased retina. Throughout this process, features of the simulation toolset itself were modified to increase the precision of the results, leading to a novel method for computing effective bulk resistivity for use in such multiscale modeling.

This simulation strategy was then extended to the application of a hippocampus prosthetic device, which has been proposed to restore and/or enhance memory in patients with memory disorders such as Alzheimer's disease or dementia. Using this multiscale modeling approach, we are able to provide recommendations for electrode geometry, placement, and stimulation magnitude for increased safety and efficacy in future experimental trials. In attempt to model neural activity in dense hippocampal tissue, a simulation platform for considering the effects the electrical activity of neural networks have on the extracellular electric field, and therefore have on their neighboring cells, was constructed, further increasing the predictive ability of the proposed methodology for modeling electrical stimulation of neural tissue.

For my parents, Chris and Sheri.

CONTENTS

LIST OF FIGURES

LIST OF TABLES

ACKNOWLEDGEMENTS

First of all, I would like to thank my advisor, Gianluca Lazzi. Since meeting him as an undergraduate student, he has been patient, trusting, and encouraging, with his guidance exceeding the work in this dissertation and helping define my career path. I would also like to thank Carlos Cela for his mentorship, and my committee members, Christopher Butson, Ross Walker, Christopher Johnson, and Florian Solzbacher for their invaluable advice and interest in my work.

This work would not have been possible without the dedication and interest of collaborators and coauthors. Thank you to Robert Marc, James Anderson, Bryan Jones, Phillip Hendrickson, Gene Yu, Clayton Bingham, Ted Berger, Boshuo Wang, James Weiland, Mavin Martin, Andrew Gilbert, and Anil RamRakhyani. Lastly, thank you to my family and friends for their support and aid in balancing life throughout this time, including my parents Chris and Sheri, my sisters Kelsey and Corinne, Danielle Cushing, Hyunu Kim, Erik Gamez, and many others.

CHAPTER 1

INTRODUCTION

1.1 Background

1.1.1 Computational Modeling

Computational modeling is commonly used for designing and analyzing the efficacy of neuroprosthetic electrodes used as therapeutic and/or rehabilitative devices for treating patients with neural disorders. In order to design effective biomimetic devices for restoring functionality to impaired neural tissue, an understanding of the tissue's natural behavior, its response to stimulation, and any changes to the tissue's behavior due to the impairment is required. Computational modeling provides a means to investigate each of these points, with tools existing for modeling neural tissue, matching experimental results, as well as tools for modeling induced electric field in neural tissue due to an externally applied stimulus. As computational ability increases and more therapeutic neuroprosthetic devices are introduced, computational tools continue to evolve. Traditionally, modeling has been focused to individual disciplines. At a larger spatial scale (order of μm to cm), numerical techniques in electromagnetics (EM) are used to estimate the electric field in biological tissue due to given stimulus parameters, using methods such finite-difference-time-domain (FDTD), finite element modeling (FEM), or the admittance method (AM). While advantageous in their ability to predict electric field patterns in biological tissue with complex heterogeneous anatomy, anisotropic dielectric properties, and complex electrode geometries and electrical properties, such modeling approaches neglect underlying neural behavior. An early approach to estimating neural activity resulting from the change in extracellular electric field was through the application of the activating function [4]. This function was derived from the Hodgkin-Huxley model, noting that neural activation depends on the rate of change of extracellular electric field with respect to distance along an axon. While useful for initial comparisons of different electrodes and predicting hyperpolarization or depolarization of neural segments, the

shape of the electric field pattern in extracellular space is certainly not the only factor in neural activation. Inherent features of the neural tissue have been shown to greatly affect the response to electrical stimulation, including accurate cellular morphology, network connectivity (including excitatory synapses, inhibitory synapses, and/or gap junctions), and biophysical properties. So, at a finer scale (pm to nm), computational techniques for modeling nonlinear dynamics of cells and cellular networks, using tools such as NEURON [5], have been used. Models in literature with morphological and topological properties closely following experimental studies are widely available, allowing for cells of the tissue of interest to be studied. This addresses the concerns of using purely EM-based approaches for predicting the neural tissue's response to electrical stimulation. However, cellular models are typically considered in isotropic space, neglecting the effects of changes in the extracellular electric field.

Combining methodologies at both scales into multiscale models has become more common, consolidating the complexities of heterogeneous tissue and how the EM patterns at this scale affect the response at the cellular level. This approach is taken in this work, with the overall goal of combining quantitative data from research conducted over the past few decades into an effective predictive tool for understanding the interaction between neural tissue and electrical stimulation, and applying it towards the design and innovation of next generation neural stimulation devices. Specifically, a retina implant in human and an experimental setup of rat hippocampus stimulation serve as test benches, towards improving existing neuroprosthetics for treating blindness and memory disorders, respectively. However, the proposed methodology is intended to be scalable to any neural electrical stimulation application. This involves the construction and validation of such coupled electromagnetic-neural computational models, application to electrode design, and approaches to increasing the precision and efficiency of the computations.

1.1.2 Retina and Hippocampus Prosthetics

In diseases such as age-related macular degeneration (AMD) and retinitis pigmentosa (RP), the retina degenerates over time leading to blindness. Systematically stimulating surviving cells has been shown to restore partial vision, artificially inducing firing in retinal cells [6]. While this type of system is able to induce some percept of vision that is invalu-

able to blind patients, the goal of restoring their sight to a state of normal visual acuity has yet to be accomplished and the implementation remains relatively crude. Since the introduction of retina prosthetics, there has been research dedicated to increasing the resolution of the perceived vision [7, 8]. Research on electrode configurations, stimulation schemes, and pulse shapes provides steps towards the goal of high-resolution vision, equipping engineers with tools for designing the next generation of retina prosthetics. However, our belief is that insights into how to compile the results of different studies into the most useful stimulation strategy can be accomplished through large-scale, connectome-derived, multiscale modeling. In fact, to date the mentioned research has been conducted either empirically, using finite element simulations of bulk-tissue and stimulation electronics, single cell neural simulations, simplified networks of neural cells, or, in few cases, combinations of all above for multiscale approaches. Such approaches are oversimplified, neglecting anatomical and electrophysiological features of neural degeneration, such as cellular death and neural network remodeling, as discussed in more detail in Chapter 4. A more complex representation of the retina, for understanding the behavior of the retinal circuitry during both natural sight and in a diseased state, is essential when trying to replicate its functionality in a true biomimetic device. This allows for a virtual platform for studying algorithms for optimal stimulation, aiding in existing experimental studies [9, 10].

The hippocampus device considered in this work is a prosthetic for enhancing and/or restoring memory accuracy and retention in patients with memory disorders, such as Alzheimer's disease or dementia. The hippocampus has been shown to be vital in encoding and retaining long-term memory, with any impairment leading to memory deterioration. In order to address this and design a system to restore memory functionality, research has been conducted to understand the factors within the hippocampus that are involved in memory retention, concluding that the firing patterns between regions of the hippocampus are vital in the encoding of long-term memories. Berger et al. have designed a system to bypass impaired hippocampal regions [11]. This prosthetic records neural spiking patterns from two regions, predicts if a memory will be encoded properly or not, and uses an online model to predict the required firing patterns in the further upstream region for a properly encoded memory. Stimulating electrodes are then used in attempt to induce

the predicted patterns. This system has proven effective in restoring and/or enhancing memory retention in rodents and primates [12]. However, a clear understanding of ideal electrode placements, geometries, and stimulation patterns are relatively unknown, and current knowledge is mostly based on empirical observations. Research by Berger et al. has also been focused on understanding the neural circuitry in the hippocampus through simulations of large-scale compartmentalized neural network model construction [13]. This is providing data on the factors involved in neural communication in this region, and initial efforts to incorporate multiscale modeling of electrical stimulation with this neural model have been attempted and are described in Chapter 6. As we move closer to possible clinical trials for helping human patients with memory disorders, this computational modeling will prove useful as a predictive tool, aiding in the choice of ideal stimulation parameters while avoiding tissue damage.

1.2 Overview

The overall goal of this work was to construct computational tools for providing recommendations for improving neuroprosthetics that use electrical stimulation to restore neural functionality, focusing on retina and hippocampus prosthetic devices. Through this dissertation, features of the computational modeling approach are addressed individually, resulting in multiscale predictive models of retina and hippocampus. Through the construction of these models, simulation studies provided recommendations of stimulation waveform shape for increasing control of spiking patterns in diseased retina, an electrode array geometry for increasing the induced visual resolution, and electrode placement for hippocampus prosthetic experiments.

This involved first constructing a model with sufficient complexity and parameter space to model both neural activity and how neural tissue responds to electrical stimulation. Chapter 2 describes the conceptualization of this multiscale model of electrical stimulation of retina. This began with exporting a connectome dataset that contains accurate morphology from a segmented and transmission electron microscopy (TEM) imaged rabbit retina (at a nanoscale resolution). In addition, it has been annotated with cell and segment type at any given location, and all observed network connectivity, including synapse type, location, and weight. The dataset was reformatted and compartmentalized

in NEURON software [5], providing as realistic of a model of a retinal neural network as possible. Biophysical models with Hodgkin-Huxley kinetics were applied to this model and it was coupled with a three-dimensional (3D) heterogeneous model of retina and implant electrodes. A combination of the Admittance Method and NEURON software was used to simulate the neural network response to electrical stimulation. Chapter 3 discusses the bulk resistivity used in the model discussed in Chapter 2, illustrating the importance of the precision of the properties that the bulk-tissue is discretized by. A methodology for computing effective bulk resistive properties of the retinal layers through the knowledge of the cellular morphology was then proposed.

In the previous two chapters, biophysical models of retinal ganglion, amacrine, and cone bipolar cells from literature were applied to each respective cell. However, such biophysical models were constructed based on experiments using healthy retina that was not suffering from degenerative disease, due to the lack of available models of diseased retina. This is addressed in the work described in Chapter 4, in which the model was enhanced to include features of diseased retina. A computational study was then conducted in order to recommend a stimulation waveform shape tailored to retina that has undergone cellular death and some neural remodeling that reduces the effects of degeneration and provides higher level of control over induced spiking, increasing the efficacy of the electrical stimulation as a rehabilitative technique. Chapter 5 then proposes a new electrode array geometry for increasing the resolution of the electrode array without the need for added driver circuitry or additional physical electrodes through the addition of ”virtual” electrode sites on the array. The ability of this new design was illustrated using the model described in the previous chapters.

In Chapter 6, this methodology of coupling the Admittance Method with NEURON was translated to the hippocampus. A model of bulk hippocampal tissue was developed, incorporating electrodes used in recent experiments for enhancing and/or restoring memory functionality. This was coupled with a pyramidal cell from literature and was used to predict the most advantageous electrode placement that would require the least stimulus current to cause a stimulation, to provide baseline stimulation magnitude and electrode placement for future experiments. This model was then extended to include an existing large-scale cellular network model of the dentate gyrus in the hippocampus to incorporate

network functionality. The electrode placement for increased stimulation efficiency was investigated, leading to proposed locations for inducing population firing with minimal stimulation intensity.

A limitation of this study is the lack of incorporating how the electrical activity of each cell affects its neighboring cells. This is an important consideration in hippocampus, due to the high cellular density. The AM and NEURON were coupled in a feedforward fashion, with the electric field from stimulating electrodes being computed then applied to a neural network or single cell without consideration of how cellular behavior affects extracellular electric field. In Chapter 7, a methodology is proposed for coupling the two toolsets into a closed-loop simulation strategy, allowing for cellular behavior to alter the extracellular electric field. Findings of the effects this may have on population firing behavior and efficiency of stimulation are discussed.

1.3 Significance

The work in this dissertation resulted in the most applicable and precise multiscale model for studying the response of degenerated retina to electrical stimulation to date. By using connectome-derived modeling of the neural tissue, we were able to model the spatial and temporal characteristics of neural network activity in the retina, incorporating all connections observed within a volume of mammalian retina. Through the construction of a computational model based on this invaluable metadata, connections within a real sample of rabbit retina were considered and can be altered to mimic the remodeling and neurodegeneration that retina endures during AMD or RP. This provides knowledge of natural retina functionality that can aid in the next-generation of retina prosthetic stimulation. In addition, applicable effective resistive properties of the bulk retinal tissue were computed to properly link the tissue-level model to the cellular network model. The proposed methodology for computing the resistive properties also leads to a means of simulating recording electrode geometries, which may aid in the design of future measurement setups. The accuracy in the simulation methodology was also improved. Rather than an open-loop finite-element modeling (FEM) to NEURON simulation setup, as is often seen in existing multiscale models in literature, a custom closed-loop simulation framework was organized using the Admittance Method and NEURON, incorporating

neural activity in the computation of extracellular electric field.

In hippocampus, far fewer modeling of electrical stimulation exists in literature. This is likely due to the young stage of the memory-prosthetic that we are considering, which is still in experimental stages. However, large-scale computational models incorporating hundreds of thousands of virtual cells and synaptic activity have been developed [13]. Linking this with an AM model has resulted in a predictive tool for aiding in electrode design and placement in future experimental studies.

Overall, the proposed computational modeling framework provides a more complex representation of the retina, for understanding the behavior of the retinal circuitry during natural sight is essential when trying to replicate it, and of the hippocampus to serve as a predictive tool for animal studies towards a memory-rehabilitative prosthetic. Without computational models with the proposed sophistication, desired stimulation configurations are relatively unknown, and rehabilitative devices utilizing electrical stimulation for selectively stimulating different cells or regions cannot reach their full potential.

CHAPTER 2

COMBINED NEURAL NETWORK AND BULK-TISSUE MODEL OF THE RETINA

 K. Loizos, G. Lazzi, J. S. Lauritzen, J. Anderson, B. W. Jones, and R. Marc, "A multiscale computational model for the study of retinal prosthetic stimulation," *Proc. IEEE 36th Eng. Med. Biol. Soc. Conf.*, 2014, pp. 6100-6103.

2.1 Abstract

An implantable retinal prosthesis has been developed to restore vision to patients who have been blinded by degenerative diseases that destroy photoreceptors. By electrically stimulating the surviving retinal cells, the damaged photoreceptors may be bypassed and limited vision can be restored. While this has been shown to restore partial vision, the understanding of how cells react to this systematic electrical stimulation is largely unknown. Better predictive models and a deeper understanding of neural responses to electrical stimulation is necessary for designing a successful prosthesis. In this work, a computational model of an epi-retinal implant was built and simulated, spanning multiple spatial scales, including a large-scale model of the retina and implant electronics, as well as underlying neuronal networks.

2.2 Introduction

Many people lose their sight due to retina degenerative diseases, such as macular degeneration or retinitis pigmentosa, which destroy photoreceptors over time. However, many retinal cells further downstream in their vision system remain viable. Artificial stimulation of these cells via systematic electrical stimulation through an epi-retinal implanted electrode array has been shown to create some vision in blind patients [14]. Clinical trials have been conducted to study the most advantageous stimulus parameters for

such a system. The responses are based on the percept of the patient and have provided thresholds for the magnitude of current required to elicit a visual response, as well as described shapes and colors the subject sees [15]. These results are undeniably interesting and patients are given the ability to see some objects again. However, the system is lacking a correlation between the stimulus and the affected neural networks. The stimulation does not restore the lower-level processing that occurs in the retinal layers, which accounts for some contrast-detection, color, brightness, etc. [16] Simulations of the system that incorporate the complexity of the neural networks and the stimulation electronics could be used for estimating the response and optimizing the stimulus towards this goal. Numerical simulation methods, such as finite difference methods, have proven useful in studying the path of current due to a given stimulus by discretizing a retinal tissue model based on the tissue conductivity and solving for the voltage throughout the model. However, these simulations lack the complexity and nonlinearity of the underlying neural networks. Variations of cable equations have been used for studying the complex nonlinear behaviors of single cells and networks of cells, predicting how they will respond to stimulation [5]. However, they usually consider the cell to be in a homogeneous medium and do not consider an accurate representation of the extracellular fields. Combining these two techniques, we create a multiscale approach to modeling the affect of electrical stimulation on retinal tissue, taking advantage of the benefits of both systems. By including the complexity at the spatio-temporal scales of cellular networks, as well as the field calculations throughout the tissue and implant electronics, we essentially link the system level with the cellular level of the vision process in a single model. We apply a novel Admittance Method for the extracellular voltage calculations [17], and NEURON software [5] for calculating the effect at the cellular network level, using cellular models that are translated from a retina connectome. This connectome is derived from Transmission Electron Microscopy (TEM) images of rabbit retina [18], from which all observed cells and their morphological features are labeled according to cell type and geometry, and all observed connections are noted. Extracting this dataset and transforming it into a computational model has allowed for a realistic application of spatially distributed electric field due to a stimulating electrode, as well as resulting neural activity due to any existing interconnectivity. Software was written to link these simulation platforms, providing the Admittance Method voltage results as

boundary conditions for the extracellular space in NEURON simulations. NEURON is then used to model the cellular activity. This model may serve as a platform for studying retinal prosthesis design at a high level of detail, with the overall goal of advancing epi-retinal prosthetic design to produce pseudo-natural vision to those who have lost their sight. In the following sections, the specifics of this model and how it may be used to simulate and study specific stimulation parameters are described.

2.3 Model

The multiscale model consists of two main components, one describing the retina at a system level, and the other describing the cellular network level. Figure 2.1 provides plots of both models in a diagram describing how they are correlated.

2.3.1 Large-Scale System Level

First, a large-scale model was constructed, containing the layers of the retina, the vitreous humor, and an implanted electrode array. The model was discretized into a three-dimensional (3D) matrix of cubic voxels, each noted by a tag that is unique to a specific material type. The curvature of the retina and the depth of the layers were based on

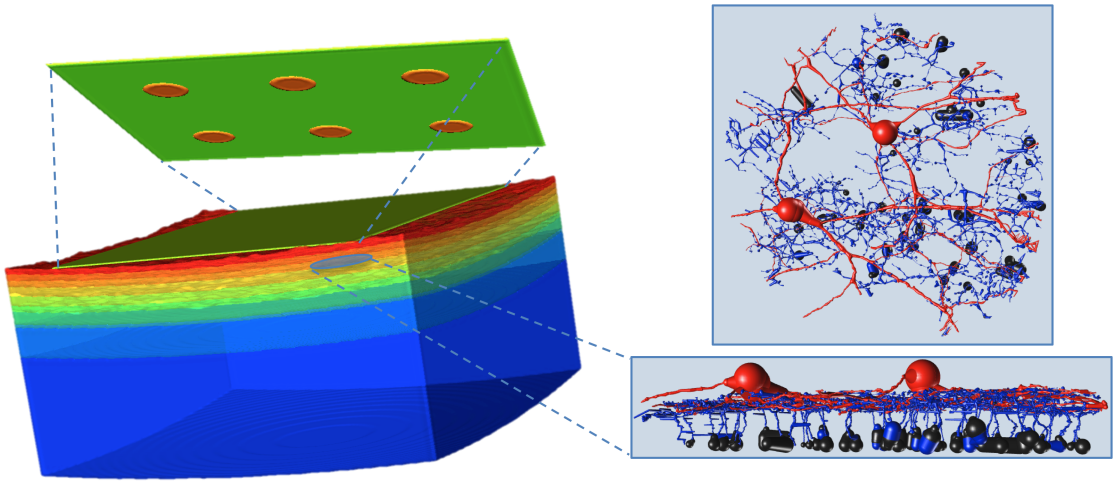

Figure 2.1. Diagram of multiscale model, including (a) 3D plot of the discretized model of the retina with an electrode array and (b) top and side-view plots of the morphology of a neural network considered for simulation, including two ON ganglion cells and 60 cone bipolar cells.

literature [17, 19]. The resolution of the model is 5 μm per voxel and the size is 400x400x300 voxels. Each retinal layer was rippled to represent a more accurate representation of the boundary between layers. This was accomplished by varying the height of the layer due to a given two-dimensional (2D) Gaussian plane. The height and width of the peaks in the plane were chosen based on approximate density and size of the cells inside each individual layer. After building the tissue model, a 2x3 electrode array was added on top of the optic nerve layer in the retina, as shown in Figure 2.1. The electrodes were based on the Argus-II design by Second Sight [20]. They are cylindrical with a diameter of 200 μm and a depth of 10 μm. Each voxel in the model is described by its resistivity. Values for the resistivity of the retinal layers are as found in literature for low frequency (below 100 Hz), and the electrodes were approximated with the properties of platinum. The resistivity values for all tissues are shown in Table 2.1 [17].

2.3.2 Small-Scale Cellular Network

A computational model of a cellular network in the inner plexiform layer of the retina was built using highly anatomically and physiologically-accurate connectome data. These data are based on nanoscale Transmission Electron Microscopy (TEM) images of rabbit retina, augmented by picoscale ultrastructural reimaging [21, 22]. Thousands of observed connections between cells in a 250 μm diameter sub volume of the inner plexiform layer were quantified, providing accurate data for use in a computational model. For the pur-

Table 2.1. Tissue Resistivities

Tissue	Resistivity (Ω m)
Photoreceptors	50.50
Outer Nuclear Layer	60.00
Outer Plexiform Layer	70.00
Inner Nuclear Layer	65.00
Inner Plexiform Layer	18.00
Ganglion Cell Layer	70.00
Optic Nerve Layer	70.00

poses of this work, sixty cone bipolar cells that communicate with two ON ganglion cells were selected to be modeled and are shown in Figure 2.1. This 250 μm diameter model was considered to be placed in the proper layers of the large-scale tissue model, residing in the cell-body layers in the bipolar and ganglion cell layers, as well as the inner plexiform layer between them, in which most of the communication between the two layers occurs. By duplicating the cellular model, the entire ganglion, bipolar, and inner plexiform layers in this model were populated with cone bipolar and ganglion cells. The morphology of the cells was then compartmentalized for use with NEURON software, as discussed in the next section.

2.4 Simulation Methods

2.4.1 Admittance Method

To simulate the electric field magnitude throughout the tissue-level model, a time-stepping multiresolution variant of the admittance method (AM) was used [17]. In this method, a matrix describing the admittance (G), or resistance, throughout the model is defined. The diagonal of the matrix defines the resistance at each node, while the surrounding values define the resistances between nodes, producing a sparse, diagonal matrix. The admittance is described in terms of the conductivity and the distance in the x, y, and z directions, as shown for the x direction in the equation below.

$$g_x^{i,j,k} = \sigma_x^{i,j,k} \tag{2.1}$$

A current vector (I) is then defined, with current values applied to whichever nodes contain a source. A voltage vector (V) can then be solved for using G and I in the equation below. The linear system of equations is solved using a biconjugate gradient algorithm.

$$G * V = I \tag{2.2}$$

Prior to building and solving this system, a 3D multiresolution meshing algorithm is applied to the model. It maintains minimal resolution surrounding boundaries, and increases the voxel size further away where the fine resolution is unnecessary. For example, near the boundaries between retinal layers, the resolution would remain 5 μm per voxel, whereas towards the center of the layers, the resolution may be as low as 20 μm per voxel.

By decreasing the number of nodes and edges, the computational complexity of the system is decreased.

2.4.2 NEURON Modeling

The response to the electrical stimulation at the neural network level is solved for using NEURON software. In NEURON, cellular segments are compartmentalized for solving for membrane and axial parameters. The model is split into compartments based on the type of neuronal branch and the change in geometry. Each compartment is modeled as a tapered cylinder with a cable circuit model, describing the intra- cellular and membrane properties as circuital elements. The user can define the conductance, resistance, etc., for each compartment, as well as synaptic properties between cells. The retina connectome used for defining the cellular morphology and network connectivity was reformatted for importing in NEURON. All connections within the model, including excitatory ribbon synapses, inhibitory synapses, and gap junctions, were added to the model as discussed in Section 4.3.2. Each synapse was then tested by applying a current clamp to the cell that is the source for each synapse and recording at the synaptic location on the target cell, ensuring there was a response.

All cells were modeled using modified Hodgkin-Huxley cable equations based on models in literature, with details provided in the appendix in Chapter 3.

2.4.3 Connecting to NEURON

The results from the AM simulation were applied to this model as boundary conditions. NEURON has a built-in mechanism called ”extracellular,” which allows for two extra layers of potentials and resistances to be added in series with each compartment [5]. One of these layers was utilized. Three-dimensional linear interpolation was used to estimate the voltage at the center of each compartment based on the surrounding eight nodes in the AM model. This voltage was set to the extracellular potential value in this model for each time step. A diagram describing the link between these tools is shown in Figure 2.2. NEURON can then simulate the effect those voltages at each compartment have on the membrane and axial voltage, showing whether or not specific cells spike.

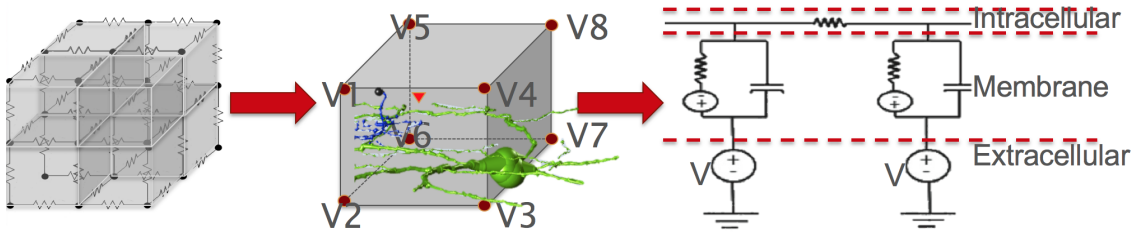

Figure 2.2. Diagram of the link between the admittance method results and NEURON. An extracellular voltage for each compartment (V) is estimated by 3D linear interpolation of the voltages at the nearest surrounding nodes from the admittance method simulation results.

2.5 Results

An example simulation was conducted to test the model. A single cycle of a sinusoidal current pulse with a magnitude of 10 μA and a frequency of 10 Hz was applied to one of the electrodes in the large-scale model shown in Figure 2.1 over 20 time steps. The voltages throughout the model were solved for using the admittance method. The voltage results were interpolated to produce an extracellular voltage value for each compartment in the NEURON model for the ON ganglion and bipolar network. A NEURON simulation was run, producing a membrane voltage value for every compartment at every millisecond. A plot showing the resulting membrane voltage for 1, 3, and 5 ms after the sinusoidal pulse stimulation on a ganglion cell and a bipolar cell are shown in Figure 2.3. The compartments are plotted as cylinders, which are color-coded based on the membrane voltage. Blue is the resting voltage defined as -60 mV and red is a voltage above +20 mV.

2.6 Discussion

This multiscale computational model for a retinal prosthetic is just one step towards advancing the prosthesis design. It can serve as a testbench for testing many different parameters, such as the effect of the location of the ground or firing electrodes, stimulus magnitude or shape, etc. One specific application that is currently being pursued is optimizing the stimulus to stimulate certain types of cells. This directly applies to the goal of mimicking natural vision. Driving color percepts will require differentially stimulating surviving midget pathways previously linked to a color network. Modeling such networks will, in turn, require access to primate or human connectomes. If a person is in bright

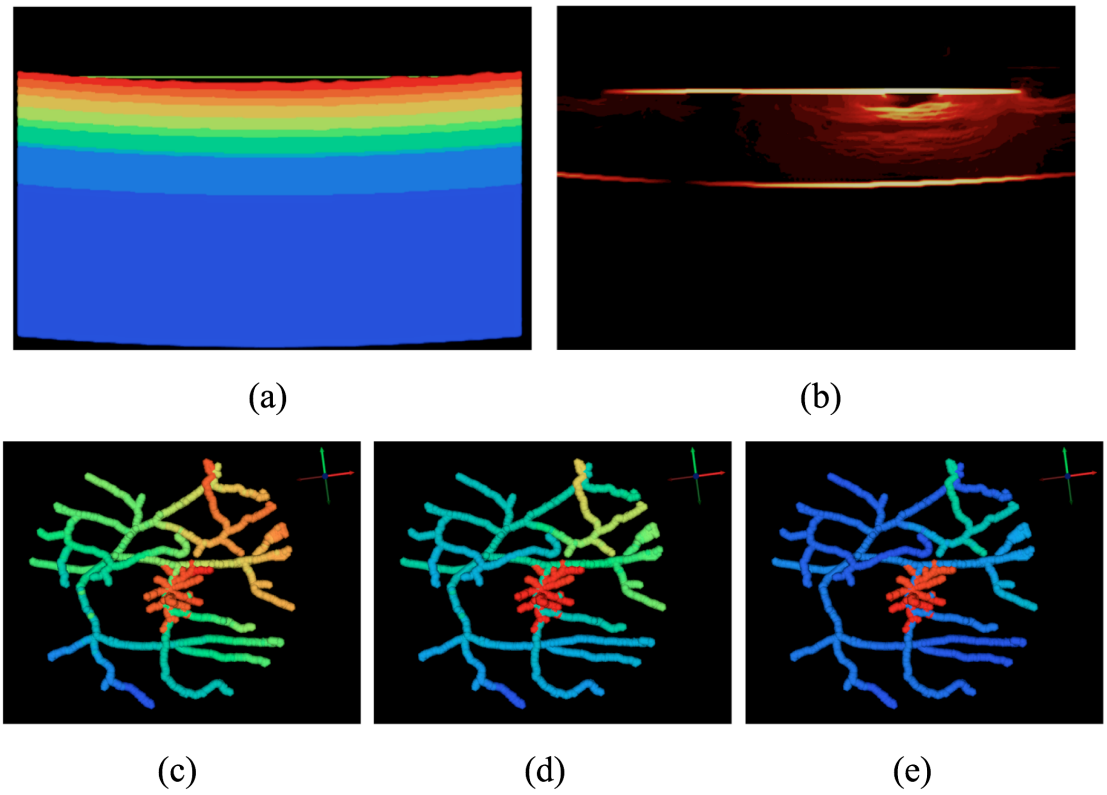

Figure 2.3. Simulation results. (a) Reference 2D slice, (b) Electric field magnitude at one time step during an admittance method simulation, (c-e) Color-coded membrane potential on a single ganglion and bipolar cell at 1, 3, and 5 ms, respectively.

light during the day, mostly circuits involving cones would need to be stimulated, and mostly those with rods in the case of less lighting [16]. This will require applying more complex channel mechanisms to describe the frequency dependence of specific cell types [23], and further research for deciding on the choice of stimuli that may elicit a response in a desired cell type, but not others. The model can also be expanded to include more interesting neural circuits that have been observed during the connectome research used to build the neural network models. There are far more circuits than ON-ganglion cell networks that can be incorporated [21]. There is feedforward and feedback inhibition, electrical coupling between bipolar cells, sheets of amacrine cells, etc. In addition, the cells shown and discussed that are part of this connectome model do not include axons. These may be added to the computational model since they are likely the location of extracellular electrical stimulation. More spatial scales can be integrated as well, including smaller scales down to the molecular level for describing the synapses and channel mechanisms

with even higher complexity. It has been shown that small changes at the molecular level can have an impact on the neural-level reaction to electrical activity [24]. Through these modifications, a highly accurate model for studying many different research topics involving circuitry in the retina may be studied. For example, variations in system performance induced by pathologic network remodeling [25] can be assessed by comparison to this normal retinal framework. This approach can be extended to neuropathologies in general. The model described in this paper combines two spatio-temporal scales of retina that are prevalent in literature. Linking them creates a simulation tool that will hopefully prove useful across multiple disciplines, in understanding the interaction between electric fields and tissue reaction, as well as the underlying electrophysiological phenomena.

CHAPTER 3

ON THE COMPUTATION OF A RETINA RESISTIVITY PROFILE FOR APPLICATIONS IN MULTISCALE MODELING OF ELECTRICAL STIMULATION AND ABSORPTION

 K. Loizos, A.K. RamRakhyani, J. Anderson, R. Marc, and G. Lazzi, "On the computation of a retina resistivity profile for applications in multiscale modeling of electrical stimulation and absorption," *Phys. Med. Biol.*, vol. 61, no. 12, pp. 4491-4505, 2016.

3.1 Abstract

This study proposes a methodology for computationally estimating resistive properties of tissue in multiscale computational models, used for studying the interaction of electromagnetic fields with neural tissue, with applications to both dosimetry and neuroprosthetics. Traditionally, models at bulk-tissue- and cellular-level scales are solved independently, linking resulting voltage from existing resistive tissue-scale models as extracellular sources to cellular models. This allows for solving for the effects that external electric fields have on cellular activity. There are two major limitations to this approach: first, the resistive properties of the tissue need to be chosen, of which there are contradicting measurements in literature; second, the measurements of resistivity themselves may be inaccurate, leading to the mentioned contradicting results found across different studies. Our proposed methodology allows for constructing computed resistivity profiles using knowledge of only the neural morphology within the multiscale model, resulting in a practical implementation of the effective medium theory; this bypasses concerns regarding the choice of

resistive properties and accuracy of measurement setups. A multiscale model of retina is constructed with an external electrode to serve as a test bench for analyzing existing and resulting resistivity profiles, and validation is presented through the reconstruction of a published resistivity profile of retina tissue. Results include a computed resistivity profile of retina tissue for use with a retina multiscale model used to analyze effects of external electric fields on neural activity.

3.2 Introduction

Computational modeling is commonly used for designing and analyzing the efficacy of neuroprosthetic electrodes as well as for safety implications of electromagnetic fields, and to understand physiology and anatomy of underlying neural cells. Model design varies, simplifying the domain in order to analyze the role of different parameters. The resolution ranges across a large spatial scale, from specific ionic current activity at the cellular membrane or a synapse (pm to μm), to large-scale models considering the current distribution across prosthetic electrode arrays and bulk-tissue (μm to cm). For example, in the retina, single cell models based on measured morphologies and membrane properties have been used to analyze the passive and active properties of cell membranes [26][27], the dynamics of voltage-gated ion channels [23][28], the stimulation region due to external electrodes [29], and for modeling observed cell-type-specific phenomena [3][30]. These models have quantified the cellular behavior, and have given insight as to what their roles may be in retinal circuitry. Consolidating findings from these single cell studies into cellular network models can then be used to analyze the role of connectivity [31][32][33]. Other studies have focused instead on prosthetic designs rather than anatomy and physiology, considering geometry and placement of electrodes, differentiating existing devices and suggesting future design constraints. [8][34][35][36] Work has also been done to more accurately represent the cellular composition of tightly packed cells and confined extracellular space, as shown in [37][38]. In this work, the authors propose a mean-field volume conductor model and a multidomain modeling framework that includes the effects of cellular composition on extracellular potential by modeling the neural tissue with an admittivity kernel, which can be incorporated into large-scale finite element simulation software.

As computational ability increases, and efforts in cellular physiology modeling and

electrode design/electromagnetic (EM) modeling evolve, combining methodologies at both scales into multiscale models has become more common. This consolidates the complexities of heterogeneous tissue in the extracellular space, and how the electromagnetic field patterns at this scale affect the response at the cellular level [34] [39][40][24][41]. However, existing models typically characterize the bulk extracellular resistive properties with resistivity values extracted from measurements of the involved tissue found in literature, which may not be accurate for the specific neural models considered due to measurements being taken from a different animal, the measurement setup conducted in different environments (controlled in vitro), or inaccuracies in the measurements themselves due, in part, to the small dimensions of the considered tissue. Also, the process of inserting a probe into neural tissue in attempt to measure at a fine spatial scale can damage the cells and possibly alter the morphology and resulting measurements.

The goal of such measurements is to provide data for EM models for analyzing implications of electrical stimulation. In this paper, we propose a method for reversing this process, using computational models to predict the resistivity of the tissue. This is essentially a practical realization of effective medium theory [42], using assumptions of resistive properties of microscale local elements to estimate effective bulk properties at a global scale. In order to link the EM model to a cellular model appropriately, we take exact morphological data from the cellular network model into consideration for reconstructing a resistivity profile of the bulk retina tissue. This process allows for ideal recording electrode placements, without the complications of measurement setups (electrode probe construction, segmenting neural tissue, modeling the electrical effects of the electrode interface, etc.).

First, to provide motive for the resistivity calculations, stimulation thresholds were calculated using two measured resistivity profiles from literature, exposing an order of magnitude difference in required current magnitude for stimulating the retina cellular network and variation in the spike initiation location for the same pulse width. A multiscale simulation process was used for simulating neural activity resulting from current source(s) applied to electrodes with realistic geometry and placement, following the process proposed in previous work, described in [41]. The Admittance Method is used to calculate voltage throughout a multiresolution mesh, at a scale on the order of microns, representing

bulk-tissue that is discretized by resistivity. The resulting voltages are interpolated to obtain values at the center of each neural compartment within a retina neural network, and are applied as extracellular sources to observe resulting neural activity. A sensitivity analysis of the resistive properties of the model is conducted in this paper, using this multiscale approach to simulate the neural response to epi-retinal electrical stimulation, comparing the responses when the tissue described using different resistivity profiles from literature. Differing from the work proposed in [41], a more complete model of the neural network is utilized, incorporating amacrine cells (making a total of 163 cells) and observed synaptic connections, a higher resolution Admittance Method model with a resolution as fine as 1 μm, and different representations of the retina tissue, as described in further detail in the second section of this paper.

Further, and differing from [41], the focus of the present manuscript is to propose a method for calculating the resistivity profile of the retina to address the discrepancies in neural activity between results of simulations determined using different empirical data, with the overall goal of increasing the accuracy of multiscale simulation setups for analyzing electrical stimulation of retinal tissue. To do this, the cellular network was discretized and incorporated into a model that was used to calculate the resistance at various layers in the retina network using the Admittance Method. The methodology for the resistivity calculations was validated by simulating a resistivity profile of a currently used bipolar impedance probe in retinal tissue [43], matching the probe dimensions and experimental setup, resulting in a closely-matched profile. This validates the simulation methodology and shows application of this simulation setup as a predictive tool for resistivity measurements. By modifying the geometry and placement of the electrodes within the model, inaccuracies may be predicted and used as an aid in designing effective measurement probes and measurement setups. This is in addition to the overall goal of this work of leading to increased accuracy within multiscale models, and therefore allowing for accurate estimation of current magnitude thresholds for electrical stimuli, aiding in decisions for current injection limits and innovative electrode design.

3.3 Simulation Methods

First, simulations were run to provide a context for the need to calculate effective bulk resistivity of retina tissue. As mentioned in the introduction, a multiscale modeling approach is taken for analyzing electrical stimulation of the retina. The retina model consists of two independent computational models. The first describes the retina at a μm-resolution, including an implant electrode and layered representation of retinal tissue. The retina layers are discretized by resistivity, and are defined here using two different empirical datasets from literature to assess the sensitivity of the resistivity profile within this model when analyzing electric field throughout the tissue or neural activity. The transient voltage response to a time-stepping current source applied to the electrode was calculated throughout this model using the Admittance Method [44]. The second describes the underlying cells at a nm-resolution, incorporating morphological and synaptic data into a compartmentalized model, used for simulating induced neural activity using NEURON software [5]. The two are linked together by interpolating the voltage results to apply as extracellular sources to the neural segments, creating a complex multiscale model. These methods are described in detail within this section. Section 3.3.3 then describes a proposed computational method for estimating effective resistivity directly applicable to this multiscale model, addressing discrepancy in electric field and neural activity results due to resistivity variation in the model.

3.3.1 Bulk-Tissue Level Model

The large-scale model consists of a three-dimensional hexahedral multiresolution mesh, with a resolution defined here to be as fine as 1 μm. It is discretized based on the dielectric properties of the tissue each voxel represents. These properties for the retina are described as layers of homogeneous resistivity, following measured values and layer depth found in literature. Two different resistivity profiles were considered to illustrate the variation that can occur in resulting electric field, and therefore variation in neural spiking activity, due to the choice of resistivity properties [1][2]. Two separate models were constructed for this comparative study. The first profile was the result of measurements taken with a bipolar electrode impedance probe, inserted into a rat retina sample at increments of 20 μm [1]. The results produced a profile with a monotonically-increasing

resistance with depth. This is unexpected, as the retina has a well-defined set of anatomical layers that would likely produce fluctuating resistance. The profile found is theorized to be due to the size of the electrode geometry, being orders of magnitude larger than the neuronal segments. The second profile is based on observed anatomical layers. Resistance measurements were averaged for each individual retina layer [2], resulting in higher resistance in the nuclear layers than in the plexiform layers. A single planar disk electrode was placed epi-retinally within both models, against the surface of the retina, in order to simulate electrical stimulation. It has a diameter of 200 µm and is flush with insulation, following dimensions of a currently-used retina prosthetic device [45]. A rendering of the model, created in SCIRun [46], and plots of the two considered resistivity profiles are given in Figure 3.1.

A multiresolution variant of the admittance method was used to simulate electric potential fields within the model. The admittance method (AM) is a quasi-static electromagnetic field solver. It takes an admittance matrix (G) as input, which describes the admittance seen at, and in between, each node in the model. With a given set of current source(s) defined in a vector (I), a vector (V) containing the voltage at each node may be solved for using Kirchoff's Current Law. A Krylov sub-space iterative solver is used for

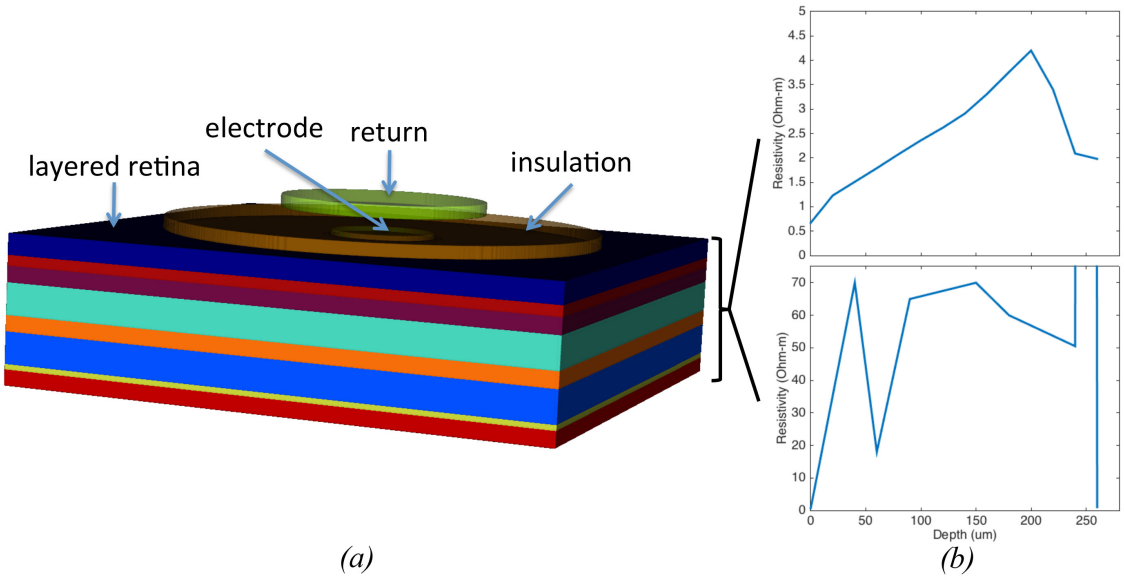

Figure 3.1. Bulk-tissue level model of retina. (a) 3D Rendering of discretized model of retina tissue and electrode setup, and (b) resistivity profiles considered for discretizing tissue layers based on studies [1] (top) and [2] (bottom).

solving this linear system for node voltages. In-house code written in C++ was used for constructing the 3D models, the multiresolution hexahedral meshing, solving the system for node voltages, and post-processing. Further details of the methodology are presented in [44][17]. This method has multiple benefits appropriate to this study: a multiresolution mesh allows for decreased computational complexity while allowing for fine resolution in locations requiring it, and the setup as a circuit topology allows for the addition of individual circuit components in the model. Both of these features could be useful for modeling small-dimension neural segments and confined extracellular space [37]. Also, as mentioned in the introduction, the ability to model electrodes of any geometry and placement for resistivity measurements allows for ideal systems that are impractical in experimental setups.

3.3.2 Cellular Network Model

While the AM solution can provide voltages throughout the tissue due to the induced field, it disregards any activity that is occurring in the neuronal networks, which is vital in understanding the retinal response to an electrical stimulus. Therefore, a neural network model was developed using a subset of a connectome dataset based on nanoscale Transmission Electron Microscopy (TEM) images [25][21]. Extracted connectomics data provided the means for modeling neural networks within the retina, consisting of accurate morphologic and synaptic data. It was compartmentalized for use with NEURON software [5], modeling individual segments as tapered cylinders with an electrical description defined with a modified cable model, as discussed in Chapter 2.

For the purposes of this paper, an ON-ganglion cell network was considered, containing 163 cells, along with all observed gap junctions,and synapses. A rendering of the morphology of this network is provided in Figure 3.2. Complex ionic mechanisms were applied to each compartment, following published measurements and models. Varying parameters were applied depending on neuronal segment type (soma, axon, dendrite) and cell type, differentiating them as either ganglion, cone bipolar, rod bipolar, or amacrine (or horizontal) cells. Ganglion cell properties follow the conductance and rate equations given for a multicompartmental cell by Fohlmeister et al. [30]. Bipolar and amacrine cell properties are as listed in the network computational model given by Publio et al. [31].

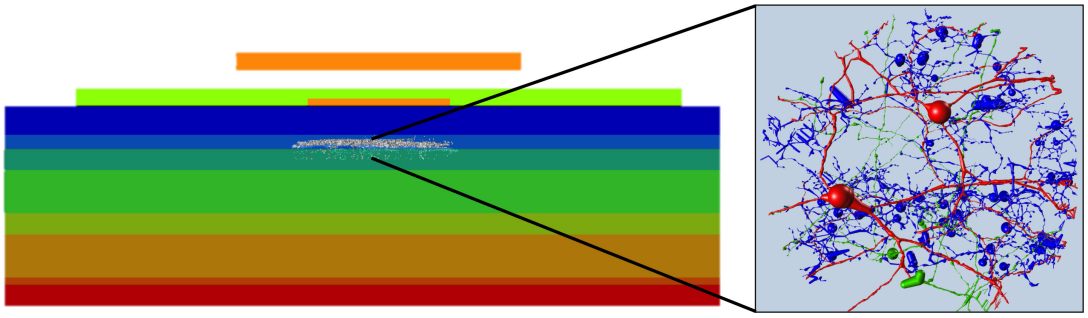

Figure 3.2. Slice of the retina admittance model with placement of the neural network extracted from the connectome dataset, and the cellular morphologies.

Ionic channel equations and gating rate constants are provided in the appendix, with further details on the current mechanisms provided in [27][30] [31]. The functionality of the active and passive cellular properties was validated by applying voltage and current clamps to each, and comparing the resulting membrane voltage and current with those given in the papers the values were taken from.

3.3.3 Current Threshold Calculation

The effect that extracellular stimulation via epi-retinal electrodes has on the neural network was simulated. The AM simulations provide voltage potential fields throughout a model of retina and surrounding tissue for a time-stepping current input, which was applied as a 1ms-wide cathodic pulse. By translating the NEURON model coordinates to a proper location within this retina model, about 50 μm into the retina beneath the surface of the electrode, as shown in Figure 3.2, the voltage values at the membrane of each compartment may be interpolated and extracted. The coordinates for the center of each neural segment were extracted from the NEURON model, and a script was written to interpolate voltages from the nodes surrounding each of these coordinates within the Admittance Method results. These values are applied as a voltage source in series with the cell membrane, using the built-in 'extracellular' function in NEURON. This function allows for applying up to two layers of extracellular voltage in series with the membrane in the cable model. One node per neural segment was utilized for applying voltage that was interpolated to the location of the center of the neural segment. Resulting membrane voltage is then solved for in NEURON. The current magnitude threshold was found by

scaling the input current to the nearest mA required for a ganglion cell in the network to activate.

The resulting current magnitude thresholds for activation of the ON ganglion cell network, as well as the voltage and electric field patterns throughout the bulk-tissue resulting from Admittance Method simulations, were compared for these two setups to analyze differences found when applying different published retina resistivity representations.

3.4 Computing Resistivity

3.4.1 Simulation Strategy

After analyzing the variation in stimulation threshold that resulted from the choice of retina resistivity properties, a method was devised for constructing a resistivity profile of the tissue containing the cells in the connectome dataset used for creating the NEURON model. A 3D model was constructed with two planar electrodes on either side of the tissue, which was given a thickness of 50 μm, the height of the connectome retina sample. The x- and y-dimensions of the electrodes match the dimensions of the model, with a current source placed across the two, producing an ideal current source across the tissue. Thus, the resulting resistance of the tissue between the electrodes is found by solving for the voltage across the electrodes using the admittance method, and dividing it by the injected current, following Ohm's Law, and the resistivity using Pouillet's Law. The meshing of this discretized 3D model and admittance method simulation was done using in-house admittance method code, as discussed in the Simulation Methods section. The methodology was tested by setting the inter-electrode tissue homogeneous properties with a known resistivity, and ensuring that the solution resistivity matched the defined value. A diagram of this method is shown in Figure 3.3.

The morphological data for the connectome dataset was then voxelized and merged with this model, populating the inter-electrode space with the cellular network. The density of cells within the model was increased by duplicating the ON-ganglion cell network and populating the tissue space. This was done to more closely match the cellular density in the entire sample, rather than just including a single network. Assumptions regarding the resistivity of the cellular features at a micron-scale were based on the highly-resistive properties of inactive cellular membrane, set to 0.1 MΩm. The extracellular material was

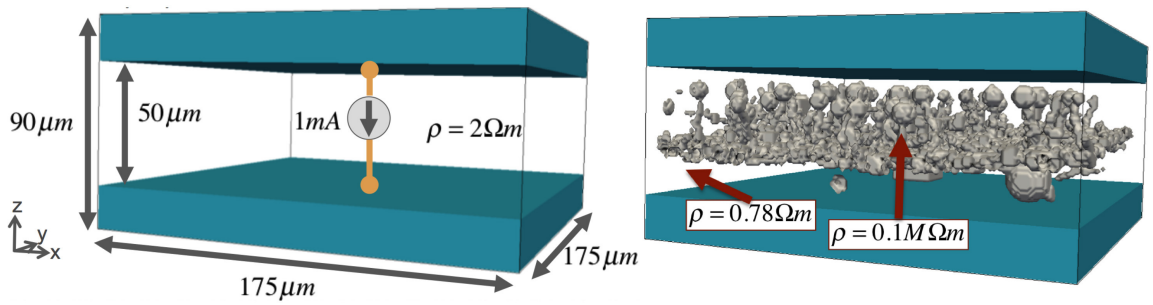

Figure 3.3. Diagram of the admittance model used to estimate resistivity of tissue, with homogeneous (left) and inhomogeneous (right) properties.

set a resistivity of saline, 0.78 Ωm. Rerunning the simulation with these new geometric features and resistive properties would produce the effective bulk resistivity of the tissue. This process was then repeated with segmented sections of the retina model. It was split into three sections: bipolar cell, inner plexiform, and ganglion cell layers, providing computed effective resistivity of the tissue using the exact neural network for the simulations described in the first section of this paper. This simulation setup was identical to the setup described above and shown in Figure 3.3, except that the volume of tissue was cropped in the z-direction, leaving only the ganglion cell layer of retina tissue, and moving the electrodes to the z-boundaries of this layer. This was then repeated for the inner plexiform and bipolar cell layers. While a parallel plate electrode placement used here is impractical in an experimental setup, due to challenges associated with segmenting retina at this fine of a scale and unavoidable damage to each layer that would occur from segmentation, it is perfectly fine in simulation. The electrode placement was chosen to achieve as ideal as possible of a setup for calculating the resistivity. By placing electrodes above and below each volume of tissue of which the resistivity is to be calculated, current can only travel through this tissue, leading to an accurate description of the resistance of each simulated volume. This is illustrated in this study by segmenting individual layers of the retina that have observable anatomical differences.

3.4.2 Validation of Methodology

The methodology used for computing effective resistivity for use with our simulations of electrical stimulation in retinal tissue was validated by recreating a resistivity measure-

ment profile found experimentally [43], modifying the setup shown in Figure 3.3 such that the electrode geometry and placement matched that of the experimental setup. A bipolar electrode probe was used, with a pencil-shaped tip. The 25 μm tip served as the anode, and a ring 25 μm up as the cathode. A model of this electrode probe was built, following the dimensions in [43], and placed within the model of the cells described in the previous section, with the parallel plate electrodes removed. A rendering of this model is given in Figure 3.4. Their process followed the Peak Resistance Frequency (PRF) method, in which the resistance across the two leads is measured and scaled based on a k factor to calculate the resistivity. This k-value is found experimentally, measuring the resistance in a medium of known resistivity and calculating the scalar (units of cm^{-1}) that would result in the expected resistivity value. Simulations were run first without the cells included in order to compare the simulated k-value with the value found experimentally. The tissue was given a resistivity value of 0.637 Ωm, matching that of the solution used in the experimental study. Simulations were then repeated with the cellular network included, with the probe translated 10 μm further into the neural network with each successive run. The correlation between these results and the experimental data was analyzed, ensuring the ability of this method to predict measurements that would be seen experimentally.

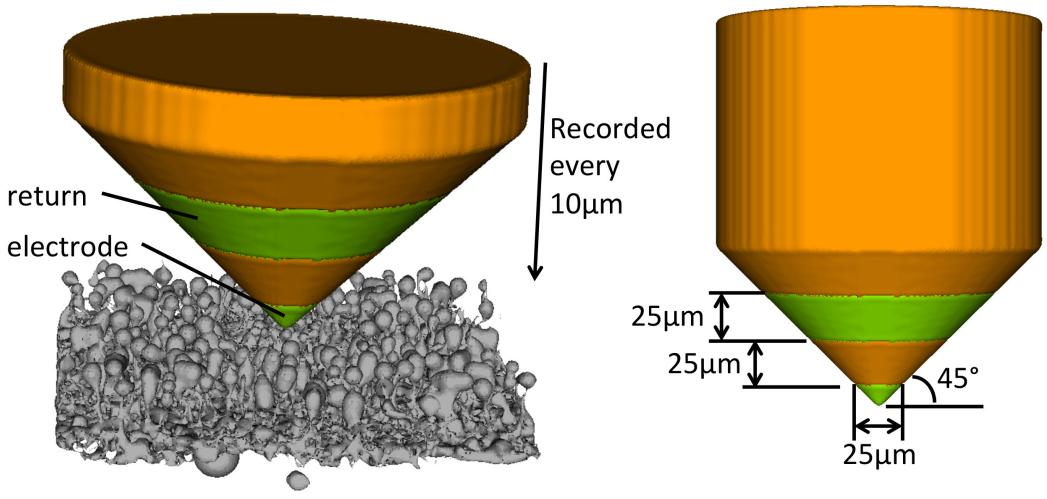

Figure 3.4. Rendering of admittance model including concentric bipolar electrode probe and cellular morphology.

3.5 Results

3.5.1 Current Thresholds

The resulting current magnitude thresholds varied considerably between the two models with different resistivity profiles. For the first model, utilizing the profile with monotonically-increasing resistivity every 20 μm produced a current threshold of 78 μA in a ganglion cell. If the synapses and gap junctions were removed, the threshold was reduced to 71 μA. This is likely due to the exclusion of inhibitory input from the amacrine cells in the network. For the second model, with a resistivity profile varying based on measured resistivity of anatomical layers, the threshold was an order of magnitude lower, 2.7 μA and 2.87 μA for a ganglion cell with and without synaptic projections, respectively. This lower threshold is likely due to the observed increase in curvature of voltage, as seen in Figure 3.5.a, which follows the metric for analyzing activation of neural segments given

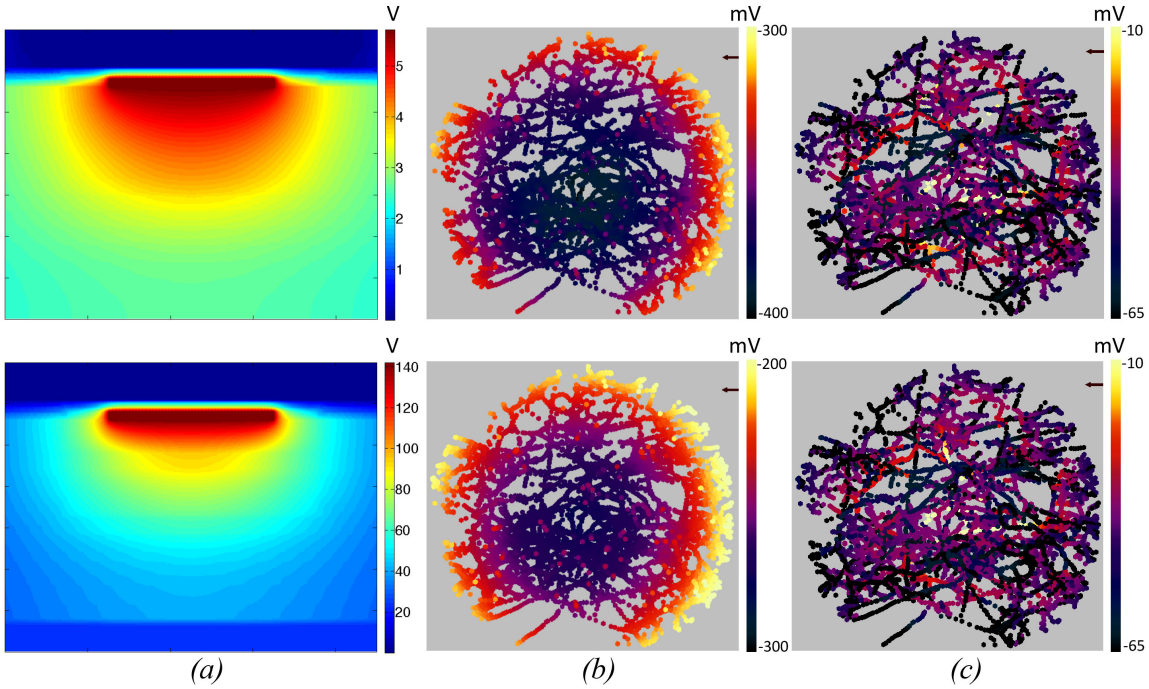

Figure 3.5. Simulation results after applied cathodic pulse at threshold current magnitude with pulse width of 1 ms for both resistivity profiles shown in Figure 3.1, the top results considering resistivity based on [1] and the bottom considering the resistivity based on [2]. (a) Slices of voltage through the center of the firing electrode, (b) interpolated extracellular voltages at each compartment in cellular network, and (c) membrane voltage at every compartment resulting from the extracellular voltages during ganglion cell spike initiation.

by the activating function [4]. In addition, the spike initiation occurs in different cells for both models. This is shown in Figure 3.5.c, and is noted by higher membrane voltage at the soma of different cells.

The results from the first model are consistent with some clinical trials for patients newly implanted with an array of electrodes with the dimensions modeled here [15]. However, the array is known to lift-off of the retina surface and is likely not completely flush with the retina surface to begin with, as they are tacked to the retina without any means for disallowing conductive vitreous fluid to fill a space between the tissue and electrode[15][47]. This would lead to an increased threshold, as the vitreous humor has a high conductivity, serving as a likely path for the injected current to flow rather than traveling directly into the tissue. Thus, for an ideal case, as modeled in this work, where the electrode is completely flush with the tissue, a lower threshold would be expected. However, without linking the model appropriately, considering the underlying cellular morphology, an accurate estimated threshold cannot be realized.

3.5.2 Validation of Methodology

The results for the model using a bipolar probe, used for validating the methodology for calculating resistivity proposed in Section 3.2, closely match that of the measurements, staying within the standard deviation of the measured resistivity values. The simulated curve comprises a similar effect as the probe reaches the tissue, with an increasing resistance tens of μm before actually inserting into the cellular network, likely due to the geometry of the electrodes and the approaching boundary of the tissue. The resistivity increases monotonically as expected throughout the volume. However, the entire retina is not considered in this computational model. So, the resistivity drops off after the 50 μm slice, encompassing ganglion cells, bipolar cells, amacrine cells, and the inner plexiform layer. A plot of the simulated and measured curves are shown on the left in Figure 3.6 for the region of retina containing the section of retina included in the computational model. A plot of the reported measured resistivity values across an entire retina slice are given on the right in Figure 3.6. If an entire retina volume was used in the simulation, the resulting resistivity profile would be expected to match for the remaining sections of retina given in this plot as well.

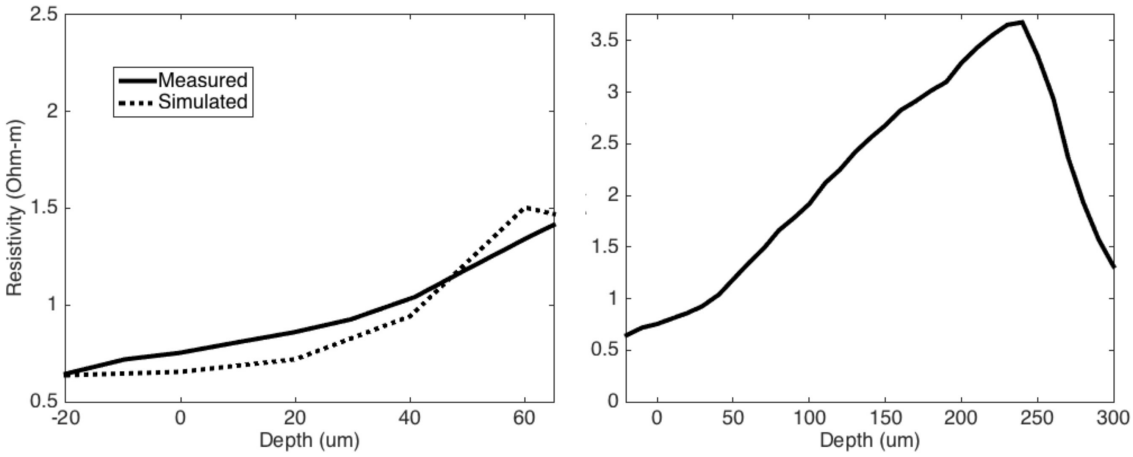

Figure 3.6. (Left) Resistivity computed using concentric bipolar electrode probe, compared with experimental measurements. The simulation included the 50 μm-thick cellular network extracted from a connectome dataset while the measurements were taken of a sectioned rat retina. (Right) Experimental measurements of the entire volume of a sectioned rat retina.

In comparison with the two resistivity profiles shown in Figure 3.1 that were used for exposing variability in neural activity results due to electrical stimulation with different resistivity, note that the shape and magnitude of the resistivity profile used in this validation study match the first resistivity profile closely. This is expected, since both studies utilized a bipolar electrode setup, with the two leads on a probe in a vertical placement with respect to the retina surface. Both studies resulted in a retina resistivity profile that increases monotonically with increased depth in the retina. As mentioned in Section 3.2, this shape of resistivity profile is unexpected for the retina, since it contains distinct anatomical layers that would be expected to have layer-specific resistivity. This unexpected result is likely due to the geometry of the electrodes. In Figure 3.4, a plot of the electrode geometry for this validation study is shown for the initial placement of the probe above the neural network, drawn to scale. The electrode leads and inter-electrode distance are nearly as large as this retina sample. Therefore, the dimensions may not be small enough to realize resistivity changes at a scale as fine as retina anatomy. This leads to a useful application of our proposed resistivity calculation, allowing for the prediction of a resistivity profile using specific electrode geometry and experimental setup.

3.5.3 Computed Resistivity

Differing from the electrode setup in the validation study above, the resistivity computations proposed in this work were in as ideal of a setup as possible. Parallel plate electrodes were placed on either side of the ganglion cell, the inner plexiform, and the bipolar cell layers in the retina volume used in this study. The computed resistivity of the the individual ganglion cell, inner plexiform, and bipolar cell layers are 0.9196 Ωm, 2.4255 Ωm, and 0.966 Ωm, respectively. Thus, the resistivity was found to be higher in the plexiform layer than in the nuclear layers. In addition, the ganglion cell layer and bipolar cell layer resistivity are within 10% of each other. The result was as hypothesized prior to conducting the computational study. As compared to the bipolar cell layer, the ganglion cell layer includes cells that are larger in diameter but with a smaller cellular density. By representing the cells as highly resistive elements, the resulting bulk resistivity is expected to match closely. Within the inner plexiform layer between the two, there is a high density of dendritic trees from both the bipolar and ganglion cell layers. Therefore, by the same highly resistive approximation, this layer was expected to have a higher resistivity.

3.6 Discussion

3.6.1 Scalability of Methodology

While this study was conducted using the example of an implemented retinal electrode, the methodology is scalable to any neural tissue. The benefit of the organization of this process is that it requires no prior knowledge of the bulk resistivity of the tissue. The cells used in multiscale models themselves may be used to construct resistivity profiles for use with EM modeling. For cases in which electrical stimulation is involved in tissue that is hard to measure in vivo, this process allows for an estimation of properties for calculation of stimuli parameters. For example, for the case with hippocampus electrical stimulation, large-scale neural models are available that may be used to calculate unknown resistive properties for application in multiscale models for refining and evolving the stimulation tools and processes [48].

3.6.2 Factors of Resistivity Variation

The methodology included here may be expanded to include the cells themselves into the multiscale modeling, rather than using bulk resistive properties. When observing the current density resulting from the simulation used for solving for resistivity, there is a clear peak in gaps between neuronal features, as seen in the normalized slice of current density shown in Figure 3.7. The increased variation in current density may itself be responsible for spike initiation, following the mentioned activating function metric. One of the main reasons for utilizing bulk properties rather than merging the cells into the model is the additional computational complexity introduced by the fine resolution required for incorporating cellular features. For a single network, it is feasible. However, as larger sections of retina, or other neural tissue, are considered, it becomes more difficult. Regardless, the effects of the varying current density magnitude should be considered.

3.6.3 Safety Implications

This study was conducted in order to increase the accuracy of currently-used predictive multiscale models for analyzing electrical neurostimulation. The current threshold study presented in this paper proves how vital accurate resistive properties become in such predictive studies. Without an accurately linked multiscale model, there may be inaccuracies in the resulting implications of advantages of proposed electrode geometry, current stimuli, etc. Implementing arbitrary resistivity profiles from literature without incorporating a

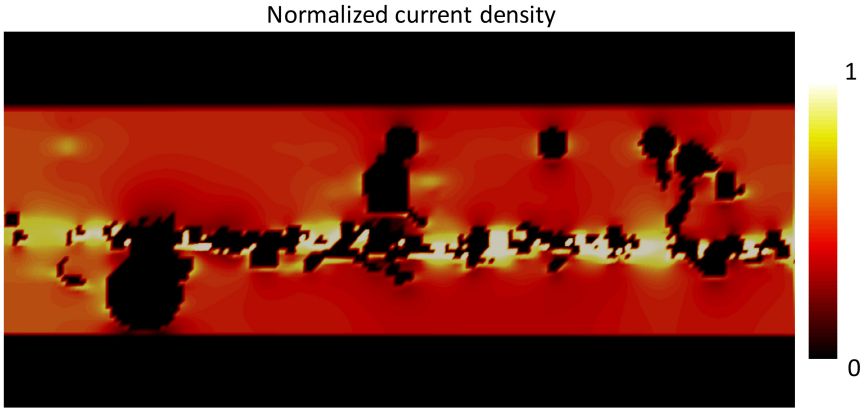

Figure 3.7. Slice of normalized current density resulting from an admittance method simulation used for estimating bulk resistivity of the tissue sample.

study to match the resistive properties of the cellular network to the bulk-tissue can lead to inaccurate predictions of current magnitude thresholds. Such predictions are crucial in considering current injection limits for clinical applications.

3.7 Conclusion

Prior to this work, there has been minimal parameter-matching across spatial scales within multiscale models for stimulation of the effects of specific neurostimulation processes (from bulk-tissue-level to cellular level). Authors typically choose a homogeneous representation of the resistance of the tissue encompassing the cells whose activity they are modeling. Appropriately linking models on both scales is vital in producing accurate realizations of the underlying cellular activity to the resulting electric fields based on the defined current injection. In this paper, a sensitivity analysis of the resistivity profile choice for neural tissue in a multiscale model, and its effects on resulting simulated neural activity, was conducted, emphasizing the importance of accurate resistivity. The proposed methodology for calculating resistivity based on knowledge of the morphology of the underlying cells can lead to a more accurate approach to investigating advantageous electrode geometry and current stimuli in neurostimulation systems. In addition, this methodology can be used as a predictive tool for designing resistivity measurement probes and validating experimental measurements.

3.8 Acknowledgements

Research reported in this publication was supported by the National Institute of General Medical Sciences of the National Institutes of Health under award number 1U01GM104604-01, the National Institutes of Health under grants R01 EY02576, R01 EY015128, P30 EY14800, and Research to Prevent Blindness. Helpful discussions with Boshuo Wang and James Weiland are gratefully acknowledged.

3.9 Appendix

The ganglion cell membrane model follows the five ionic-current model given by Fohlmeister et al. [30] The membrane current is found using Kirchhoff's current law, giving the equation below:

$$\begin{aligned} CdV/dt = -(g_{Na}m^3h(V - V_{Na}) + g_{Ca}c^3(V - V_{Ca}) \\ +(g_K n^4 + g_A a^3 h_A + g_{K,Ca})(V - V_K)), \end{aligned} \tag{3.1}$$

where $I_{K,Ca} = g_{K,Ca}(\frac{[Ca^{2+}]_i/0.001}{1+[Ca^{2+}]_i/0.001})(V - V_K)$, $[Ca^{2+}] = 0.0001mM$, $V = voltage$, $C = capacitance$, $V_{Na} = 35mV$, and $V_K = -75mV$. The gating rate constants x (m, n, h, c, a, h_A) are found using the following equation:

$$dx/dt = -(\alpha_x + \beta_x)x + \alpha_x, \tag{3.2}$$

with α and β given in Table 3.1 and conductances given in Table 3.2. More information on the ganglion cell model is given in [30].

The bipolar cell model contains five ionic currents ($I_h, I_{Ca}, I_K, I_{K,A}, I_{K,Ca}$), with their active properties and conductances as described in further detail in [27]. The conductances are given in Table 3.2, with the rate equations α and β given in Table 3.3, with the ionic

Table 3.1. Rate Constants for the Ganglion Cell Ionic Mechanisms

Na	$\alpha_m = \frac{-0.6(E+30)}{e^{-0.1(E+30)}-1}$	$\beta_m = 20e^{-(E+55)/18}$
	$\alpha_h = 0.4e^{-(E+50)/20}$	$\beta_h = \frac{6}{e^{-0.1(E+20)}+1}$
Ca	$\alpha_c = \frac{-0.3(E+13)}{e^{-0.1(E+13)}-1}$	$\beta_c = 10e^{-(E+38)/18}$
K	$\alpha_n = \frac{-0.02(E+40)}{e^{-0.1(E+40)}-1}$	$\beta_n = 0.4e^{-(E+50)/80}$
A	$\alpha_A = \frac{-0.006(E+90)}{e^{-0.1(E+90)}-1}$	$\beta_A = 0.1e^{-(E+30)/10}$
	$\alpha_{h_A} = 0.04e^{-(E+70)/20}$	$\beta_{h_A} = \frac{0.6}{e^{-0.1(E+40)}+1}$

Table 3.2. Conductances for Each Ionic Mechanism for All Cells

Conductance	Ganglion Cells		Bipolar	Amacrine
(mS/cm^2)	Soma	Dendrites	Cells	Cells
$\bar{g}_{passive}$	0.10	0.10	0.77	0.10
$\bar{g}_{Na}$	72.00	79.50	-	2.60
$\bar{g}_K$	50.40	23.40	0.318	0.26
$\bar{g}_A$	36.00	36.00	5.6	-
$\bar{g}_{Ca}$	1.20	1.20	2.00	-
$\bar{g}_{K,Ca}$	0.05	0.05	1.4	-
$\bar{g}_h$	-	-	31.1	-

Table 3.3. Rate Constants for the Bipolar Cell Ionic Mechanisms

K	$\alpha_{mK} = \frac{400}{e^{-(E-15)/36}+1}$	$\beta_{mK} = e^{-E/13}$
	$\alpha_{hK} = 0.0003e^{-E/7}$	$\beta_{hK} = \frac{80}{e^{(E+115)/15}+1} + 0.02$
Ca	$\alpha_{mCa} = \frac{12000(120-E)}{e^{(E-120)/25}-1}$	$\beta_{mCa} = \frac{40000}{e^{(E+68)/25}+1}$
K, Ca	$\alpha_{mKCa} = \frac{100(230-E)}{e^{(230-E)/52}-1}$	$\beta_{mKCa} = 120e^{-E/95}$
A	$\alpha_{mA} = \frac{1200}{e^{(E-50)/28}+1}$	$\beta_{mA} = 6e^{-E/10}$
	$\alpha_{h_A} = 0.045e^{-E/13}$	$\beta_{h_A} = \frac{75}{e^{(E+50)/15}+1}$
h	$\alpha_h = \frac{3}{e^{(E+110)/15}+1}$	$\beta_h = \frac{1.5}{e^{-(E+115)/15}+1}$

current found using Kirchoff's current law, as with the ganglion cell model, with the sum of the membrane currents given by I below.

$$\begin{aligned} I = g_K m_K^3 h_K (V - V_K) + g_{Ca} m_{Ca}^4 h_{Ca} (V - V_{Ca}) + g_A m_A^3 h_A (V - V_K) \\ + g_{K,Ca} m_{KCa}^2 m_{KCa1} (V - V_K) + g_h m_h (V - V_h) \end{aligned} \tag{3.3}$$

Additional information on the ionic current mechanisms for the bipolar cell membrane model are given in [27]. The amacrine cells were described to have only sodium and potassium channels, described using a basic Hodgkin-Huxley formulation, which allows the cells to spike, but without the repetitive firing ability of the ganglion cells. These amacrine and bipolar cell membrane models were taken from [31].

CHAPTER 4

INCREASING ELECTRICAL STIMULATION EFFICACY IN DEGENERATED RETINA - STIMULUS WAVEFORM DESIGN

K. Loizos, R. Marc, M. Humayun, J. R. Anderson, B. W. Jones, and G. Lazzi, "Increasing electrical stimulation efficacy in degenerated retina: Stimulus waveform design in a multiscale computational model," Submitted to IEEE Trans. Neural Syst. Rehabil. Eng., 2017.

4.1 Abstract

A computational model of electrical stimulation of the retina is proposed for investigating current waveforms used in prosthetic devices for restoring partial vision lost to retina degenerative diseases. The model framework combines a connectome-based neural network model characterized by accurate morphological and synaptic properties with an Admittance Method model of bulk-tissue and prosthetic electronics. In this model, the retina was computationally "degenerated," considering cellular death and anatomical changes that occur early in disease, as well as altered neural behavior that develops throughout the neurodegeneration and is likely interfering with current attempts at restoring vision. A resulting analysis of stimulation range and threshold of ON ganglion cells within retina that are either healthy or in beginning stages of degeneration is presented for currently-used stimulation waveforms, and an asymmetric biphasic current stimulation for subduing spontaneous firing to allow increased control over ganglion cell firing patterns in degenerated retina is proposed. Results show that stimulation thresholds of retinal ganglion cells do not notably vary after beginning stages of retina degeneration. In addition, simulation of proposed asymmetric waveforms showed the ability to enhance the control of ganglion cell firing via electrical stimulation.

4.2 Introduction

Retina prosthetic devices that use electrical stimulation have been designed in attempt to restore some vision in patients with degenerative diseases, such as retinitis pigmentosa (RP) or age-related macular degeneration (AMD). These devices function by using electrodes to stimulate local regions of retina tissue, approximating spatiotemporal patterns for representing the image facing the patient, intending to induce a pixelized percept. This has proven effective and has led to the design of multiple different prosthetic devices, as reviewed by Weiland and Humayun [14]. Various devices are either employed in trials or have been recently commercialized. Most notably, the Argus II by Second Sight Medical Products Inc. (Sylmar, CA) in clinical trials provided subjects with sufficient visual perception to recognize objects and discern some letters of the alphabet. However, the best measured acuity is (20/1260) and only 55% of the individual electrodes have been able to provoke a light perception within safety limits, implying the inability to locally stimulate cells and require contribution from adjacent electrodes to cause stimulation [14]. With an array that has 60 electrodes, this further limits the already limited resolution. While the current implementations are encouraging and can provide an invaluable increase in functional vision to blind subjects [6, 49], strategies for improvement should be investigated.

Research has been conducted in attempt to improve the efficiency and effectiveness of the stimulus waveform, considering shapes for decreasing the required injected current magnitude [50, 51], or precisely recreating desired spiking rates in retinal ganglion cells [10]. Attempts have been made to design clever waveforms for focusing current to locations away from physical electrodes [7, 34, 52], allowing for more stimulating sites on an array without requiring more physical electrodes or drivers, and for selectively stimulating different cell types [23, 53–56]. Additionally, studies of the electrodes themselves have considered the impact of the electrode size, placement, geometry, or the site of activation [8, 29, 39, 57].

A limitation of previous work towards the design of effective electrical stimuli is the exclusion of features of degenerated retina, with computational and experimental studies of electrical stimulation considering healthy retina (or beginning stages of degeneration) and/or excluding neural activity, considering the membrane voltage to be at a constant resting potential during electrical stimulation. There are multiple possible reasons for this.

First, there is limited availability of parameters of degenerated retina. In fact, computational descriptions of retina tissue depend on experimental studies: bulk-tissue dielectric property measurements for simulating electric field patterns and biophysical and morphological descriptions of cells for modeling cellular behavior, both of which originate from experiments that involve healthy retina in order to understand cellular or network properties of retina that are not necessarily focused on retina degeneration, for example, in [27, 28, 31, 58]. Second, when studies of degenerated retina are considered, they typically include early stages of degeneration [1, 59]. This is simply due to the lifespan of the animals used, such as mice and rats, not being sufficiently long to observe the degrees of degeneration observed in human subjects. Using a Tg P347L rabbit (a model of human dominant RP), which has a lifespan four times longer than a mouse has shown that retinal remodeling is relentlessly progressive, continuing until greater than 90% of neurons are gone [60]. Third, computational studies of electrical stimulation often have a limited scope, simplifying the parameter space to decrease computational complexity and possibility for error, by approximating extracellular space as having homogeneous electrical properties or simplifying the retina circuitry to a cellular or even cellular segment level, disregarding morphology, cell type, connectivity, or degeneration.

Properties of degeneration are clinically relevant and important to include in computational approaches for improving rehabilitative techniques. Degeneration can be broken down into four phases, as shown in the diagram in Figure 4.1. Throughout the first two phases, up to a year in the rabbit model, photoreceptors are stressed and cellular death oc-

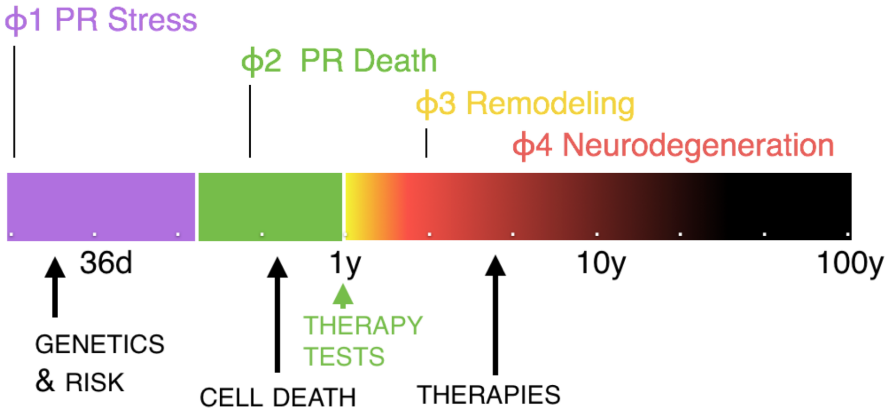

Figure 4.1. Diagram of the timeline of retina degeneration.

curs. This can be addressed in computational models by disregarding photoreceptors completely and either considering direct stimulation of ganglion cells or indirect stimulation of ganglion cells through the stimulation of presynaptic circuitry, as is done for example in [40, 41, 56]. However, photoreceptor death does not mark the end of the disease, occurs early on, and has electrophysiological effects beyond photoreceptors no longer providing light-induced input to retina circuitry. As disease progresses towards patients becoming completely blind, there is extensive remodeling of the retina, including cell migration and spontaneous neural activity [61, 62]. During this remodeling phase of degeneration, spontaneous firing and oscillatory behavior has been observed in the surviving neural networks [25, 63]. Thus, removing the input from light-sensitive cells does not remove neural activity in the retina, and instead alters it. One source of spontaneous activity is believed to be the coupling between AII amacrine and cone bipolar cells [64, 65], in which the lack of presynaptic input from the now-degenerated photoreceptors, leads to oscillatory membrane voltage in the coupled AII and cone bipolar cells and subsequent phasic bursting in ganglion cells. Studies have shown that blocking gap junctions can eliminate such activity, helping to validate this claim [3, 63]. Such spontaneous neural activity can be sufficient to interrupt attempts at systematic electrical stimulation for restoring vision, leading to ineffective prosthetic stimulation.

Towards improving the efficacy of the electrical stimulation, we provide a simulation framework for understanding the response of degenerating retina to currently used electrical stimuli and for designing new electrode geometries and stimuli waveforms. This framework is based on a multiscale multiphysics platform, using the Admittance Method for computing the electric field within a model of tissue [44], and NEURON [5] for simulating the resulting response in a neural network, following the authors' previous work [66].

From a connectomics dataset [21], a model of a ganglion cell network, consisting of realistic cellular morphology and synaptic type, distribution, and weight is constructed in NEURON. Biophysical data from literature were incorporated in each individual cell, and a script for applying the extracellular electric field from Admittance Method simulations to observe resulting network and cellular behavior to a given input was written. To induce spontaneous neural activity indicative of degenerated retina, the intrinsic properties of

AII amacrine cells within this model were altered to produce an oscillatory membrane potential, following Choi et al. [3]. Translating a connectome dataset to a computational model is a uniquely qualified approach for this study, as it is comprised of real imaged morphology and observed connections that allows for as accurate as possible of a representation of a retina neural network and resultant network behavior, reducing the need for assumptions regarding interconnectivity. This serves as a tool for further considering cellular death within the inner plexiform layer by "degenerating" the computational retina and decreasing the strength of individual synapses or gap junctions, and number of cells.

At a larger spatial scale, a model of bulk-tissue and prosthetic electronics was constructed using the Admittance Method, which was used to compute extracellular electric field due to anatomical changes in early stages of degeneration. Coupling this Admittance Method model of extracellular space with the connectome-based NEURON model combines the ability to change the anatomical structure of the retina, integrate implant electronics, and alter the biophysical properties of the cells and interconnectivity to virtually degenerate the retina.

This leads to the most detailed modeling framework for studying electrical stimulation of degenerated retina to date, effectively coupling decades of research of retina stimulation, including electrophysiological studies of cellular behavior, the connectivity map from connectomics, geometrical and electrical features of prosthetic electrode arrays, clinical and experimental data on degeneration of retina, and computational electromagnetics into a single simulation platform. In this paper, stimulation threshold and range are computed for varying degrees of degeneration and neural network complexity, and a stimulation waveform that reduces spontaneous activity within a degenerated retina and provides more effective control over ganglion cell stimulation is proposed.

4.3 Methods

4.3.1 Constructing Model of Bulk Retina Tissue and Electronics

To simulate extracellular electric field due to an applied current stimuli, a discretized bulk-tissue level model of retina tissue and a prosthetic electrode array was constructed using in-house software. A section of retina tissue, with dimensions of 6.25 mm x 4.25 mm was described as layers of homogeneous medium, following the anatomy of healthy

mammalian retina. It was voxelized with a resolution of 10 μm and discretized based on bulk-tissue resistivity. For the inner band, including the ganglion cell layer, inner plexiform layer, and inner nuclear layer, the resistivity and layer thickness were given properties that were assigned using knowledge of the cellular morphology, applying values reported in [66]. In this method, the morphological data from the connectome dataset that was translated to a NEURON model for this study, as discussed in the next section, was voxelized and segmented into these three retina layers. Electrodes were placed on either side of the tissue. The Admittance Method [17, 44] was then used to apply a current source through the tissue, and the voltage across the electrodes was computed and used to calculate the resistivity. This was using morphology from the exact connectome dataset used in this study, making these effective resistivity values for bulk-tissue as precise as possible for considering stimulation of this cellular network. The middle band, including the photoreceptor and outer plexiform layers was lumped into a single layer, applying properties reported for retina tissue [67], and the pigment epithelium, choroid, and sclera were given properties as reported by Gabriel et al.[67]. The resistivity and layer thickness are reported in Table 4.1.

A 6x10 array of 200 μm electrodes was placed epi-retinally, against the retina surface. The electrodes were given resistivity of platinum (10.6×10^{-8} Ω m), which were considered

Table 4.1. Retina Layer Discretization

Layer	Resistivity (Ω m)	Layer Thickness Healthy (μm)	Layer Thickness Degenerated (μm)
Vitreous	0.667	-	-
GCL	0.912	50	40
IPL	2.43	30	30
INL	0.97	50	30
OPL and ONL	1.98	150	30
PE	3200	10	10
Choroid/Sclera	1.98	-	-

flush with insulating material, given resistivity of 10^7 Ω m. A rendering of the model is shown in Figure 4.2. For simulating resulting voltage throughout this model for one or more of the electrodes injecting current, a multiresolution Admittance Method [44] was used, following [41].

This model was then modified to take into account anatomical changes that occur during early stages of degenerative disease, shrinking the middle band of the retina considerably, and mildly shrinking the inner band, following measurements from rat retina before and after photoreceptor degeneration from [68]. The resulting layer thickness is provided in Table 4.1.

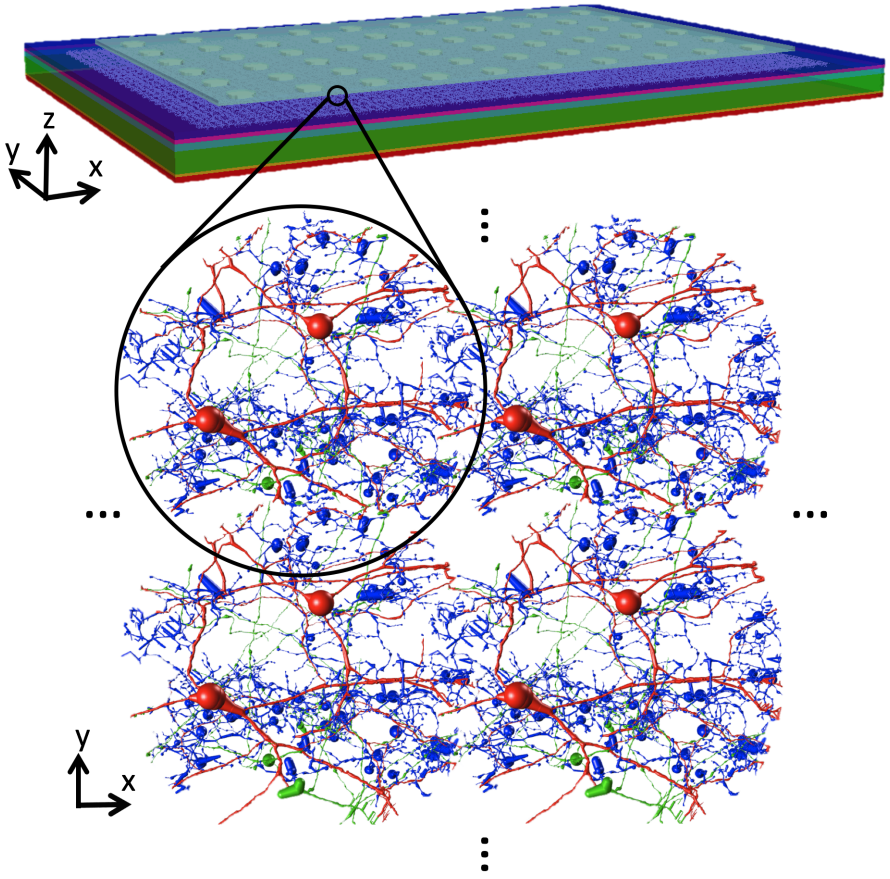

Figure 4.2. Diagram of the multiscale model of electrical stimulation of retinal tissue, including (top) a discretized Admittance Method model consisting of a layered structure describing the retina and a 6x10 electrode array placed 0.05 mm away from the retina surface, and (bottom) a rendering of the NEURON model of an ON ganglion cell network, which was tiled to populate the entire ganglion cell, inner plexiform, and bipolar cell layers beneath the electrode array. This resulted in 888 cellular networks, each simulated independently.

4.3.2 Translating Retina Connectome to NEURON Model

Morphological data for a neural network extracted from a connectome dataset of rabbit retina was converted into SWC format for importing to NEURON software [5] as a compartmentalized model, following the authors' previous work [41, 66]. This connectome is basically a connectivity map originating from transmission electron microscopy (TEM) images of rabbit retina, that has been manually annotated to populate a dataset containing morphology, cell type, receptor distribution and type, etc. [22] The extracted network used in this study consists of an ON transient ganglion cell and every cell that it directly communicates with, considering a total of 117 cells that are either ganglion, cone bipolar, or inhibitory amacrine cells. A rendering of the morphology of this cellular network is given in Figure 4.2, and a map of the connectivity of this network is given in Figure 4.3. This network model was then tiled to populate the entire inner band of retina within

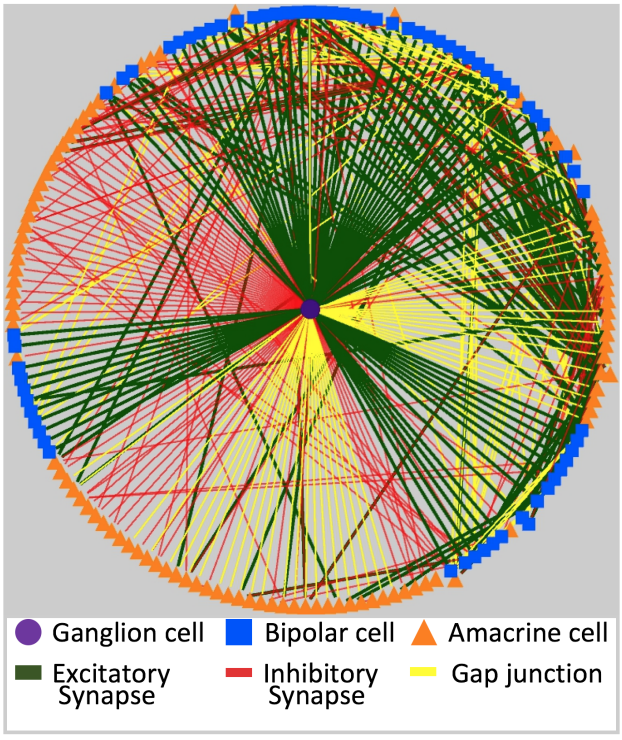

Figure 4.3. Connectivity diagram of the neural network model, showing the ON ganglion cell considered in this study and every presynaptic cell (with the morphology depicted in Figure 4.1.c), as extracted from the connectomics dataset. The node at the center is the ON ganglion cell and the nodes on the outside of the circular diagram are bipolar cells (blue) and amacrine cells (orange). The edges represent connections, including ribbon synapses (green), conventional synapses (red), and gap junctions (yellow).

the Admittance Method model described in the previous section, filling the entire region beneath the electrode array to allow for simulating the stimulation range and threshold for given inputs. The center-to-center distance between adjacent cellular networks was set to 150 μm. This resulted in 888 cellular networks for a total of over 100k cells and 10.75 million compartments.

Biophysical properties from literature were added to each cell in the NEURON model in order to include the cellular response. This includes the five ionic channel model of Fohlmeister and Miller [30, 58] for the ganglion cells, a five ionic channel model for cone bipolar cells [27, 31], and a Hodgkin-Huxley model for the amacrine cells [31], with more detail provided in [66]. A complex ribbon synapse model was implemented for all ribbon synapses in the model [69], which did not provide any discernible difference in the stimulation threshold or range simulations from using a graded synapse model following that of Publio et al. [31]. Synapse conductance was weighted based on the area of the synaptic terminal, as observed during construction of the connectome dataset, taking the minimum area of the presynaptic and postsynaptic terminals. This resulted in the inclusion of over 500 projections within the model, including ribbon synapses, conventional synapses, and gap junctions. A diagram of all of the connections considered is provided in Figure 4.3, providing a qualitative illustration of the extent of connectivity.

A script was written for extracting the location of the center of each compartment within the NEURON model, interpolating resulting voltage from Admittance Method simulations at these locations, and applying them as extracellular voltage sources using the "extracellular" mechanism that is built in to NEURON, adding them in series with the membrane. This allowed for the simulation of the effects of electrical stimulation in realistic electrodes in heterogenous tissue on neural network behavior.

4.3.3 Impact of Anatomical Changes on Computational Results

4.3.3.1 Stimulation Threshold

The current magnitude stimulation threshold was computed for a single ganglion cell network for four cases: considering a single electrode firing and all electrodes firing to see any effects on threshold from using combined electrode stimulation for both anatomical models of retina tissue described in Section 4.3.1, considering retina before and after early

degeneration by shrinking the layer thickness as shown in Table 4.1. This was conducted for a stimulation waveform that is currently used in devices such as the Argus II as reported in literature [6, 15]: a 1 ms wide cathode-first biphasic pulse with a 1 ms interphase delay. The Admittance Method was used for calculating the voltage throughout the model for this waveform for a magnitude of 10 μA, applied at either one of the center electrodes or all 60 electrodes simultaneously. The result was interpolated and applied to the neural network that was centered beneath the single firing electrode.

A script was written in NEURON for then scaling the input linearly in order to find the stimulation threshold. It takes a guess for the range of scaling factors that would include the stimulation threshold as an input. The maximum is applied, scaling all extracellularly applied voltage in the model, and the NEURON simulation is run. If there is no action potential (defined by the membrane potential of the ganglion cell in the network exceeding 20mV), then this value is doubled until an action potential is observed, setting the previous value as the minimum of the starting range. This process is then repeated for the minimum value, cutting the scaling factor in half until no action potential is observed. The average of the two scaling factors is then attempted, and is set as either the new maximum (if resulting in an action potential) or the new minimum (if there is no action potential). This process is repeated until the difference between the maximum and minimum is less than a predefined residue (using 1 nA here).

It has been observed experimentally that stimulation threshold is higher in degenerated retina vs. healthy retina. Weiland and Humayun mention in their review [14] that not considering indirect stimulation, there is likely no change in thresholds for degenerated vs. healthy retina, based on results by Sekirnjak et al.[70]. We explore this hypothesis here, considering the stimulation threshold with and without synaptic connectivity in order to model direct and/or indirect stimulation of ganglion cells.

4.3.3.2 Stimulation Range

The range of stimulation from a single electrode in the center of the array was simulated by running Admittance Method simulation, with values guided by the resulting stimulation thresholds from the previous section. This study was conducted in a similar fashion, but considering a constant input, of either 75, 100, 125, or 150 μA, and applying

the resulting voltage to all 888 cellular networks in the tiled retina model shown in Figure 4.2.

4.3.4 Retina Degeneration - Spontaneous Activity

4.3.4.1 Inducing Spontaneous Firing

Oscillatory neural activity that arises from the coupling between AII amacrine and cone bipolar cells with lack of photoreceptor excitatory input was then added to the cellular network model [63, 64]. The model up to this point does not include AII cells, as the network extracted from the connectome only included an ON ganglion cell and the cells that directly communicate with it. So, the connectome was referenced again, noting each of the cone bipolar cells in this network coupled to an AII amacrine cell, finding 47 cells [71]. An AII model was built in NEURON, with morphology and intrinsic properties following exactly that of Choi et al. [3], including fast Na and slow M-type K conductances to create an oscillatory membrane potential that is seen in the experimental studies of Choi et al. [3]. Their model was constructed in MATLAB, so it was reimplemented in NEURON and coupled with the appropriate bipolar cells in the neural network model.

The results in their paper were first reconstructed, ensuring that for the same gap junction conductance between the AII and BCs that the same oscillating membrane voltage was achieved (matched frequency, magnitude, and offset voltage). In this study, the bipolar cell models were simplified to only include passive components as used in the study in Choi's paper. Excitatory synapses within the cellular network were added back into the model in order to see any phasic firing in the ganglion cells that result from this oscillatory activity in the coupled AII-BC network. This was done for a single AII and for all 47 AII cells. Inhibitory synapses and gap junctions existing in the network were then incorporated to study the effects neural connectivity may have on such behavior.

4.3.4.2 Stimulus Waveform Design to Address Spontaneous Activity

As shown in [3], a constant current source applied to the bipolar cells has the ability to eliminate oscillatory activity. This was repeated here to ensure that a sufficiently high current source would indeed eliminate spontaneous activity, and the magnitude of membrane potential was compared with that in [3] for various gap junction conductance.

Then, an L-type Ca ionic channel was added back into the bipolar cells, due to it being a possible reason for bipolar cells responding to wide pulses while ganglion cells do not respond (as shown by Freeman et al. [23, 53], using low-frequency sinusoidal stimulation). Simulations from the previous section were repeated to ensure that this did not interfere with the oscillatory membrane potential of the coupled AII and cone bipolar cells, and resulting phasic bursting in the ganglion cell due to excitatory synaptic input from these bipolar cells.

Sinusoidal simulation was attempted, with the motive being the ability to selectively stimulate bipolar cells with low-frequency sinusoidal stimulation (5-25 Hz), causing indirect stimulation [23, 53]. This was found to only induce spiking on the peaks of the sinusoids, effectively inducing the activity that is believed to already occur in the degenerating retina from these oscillatory membrane potential that is exhibited in bipolar cells from the coupling of AII to BC.

So, a biphasic pulse was revisited. A cathodic pulse that is tall and narrow (similar to what is currently used) is used to stimulate the ganglion cell, followed by a wide anodic pulse that is long enough that ganglion cells do not respond, but bipolar cells can be sufficiently stimulated to eliminate their oscillatory behavior. The magnitude of the waveforms are modified appropriately to ensure a charge balanced stimulus, using the stimulation thresholds from Section 4.3.3.1 as a guideline for the cathodic pulse, and a minimum pulse width of 10ms for the anodic pulse, maintaining sufficiently wide pulses to not stimulate the ganglion cells while still eliminating the oscillatory behavior. This is based on the study by Freeman et al., showing stimulation frequency of less than 100 Hz to not cause direct stimulation of ganglion cells.

This proposed waveform would allow control over ganglion cell firing, eliminating spontaneous bursts of action potentials in ganglion cells and only allowing action potentials when desired. In addition, this type of asymmetric biphasic pulse was also suggested as a more efficient waveform for retina stimulation, decreasing the total charge injection while maintaining stimulation, following a set of experimental studies given in [51].

4.4 Results

4.4.1 Stimulation Threshold

The resulting stimulation thresholds for the ganglion cell in this network shows that the lowest threshold is in the degenerated bulk-tissue model with synaptic connectivity. This makes sense intuitively: by reducing the thickness of the retina, current density becomes higher within the inner layers of the retina, spreading through a larger range of tissue, and therefore, reducing the stimulation threshold. Slices of the voltage profile through the firing electrode for both bulk-tissue models are included in Figure 4.4. to illustrate this point. Including synaptic activity also allows for the stimulation of presynaptic circuitry that can indirectly contribute to the stimulation of the ganglion cell. When synaptic activity is removed, considering only direct stimulation of the ganglion cells, the threshold increases. This leads to a similar stimulation threshold for the healthy anatomical model including synaptic activity and the degenerated anatomical model with loss of synaptic activity. This preliminary result supports Weiland's claim in [14] that by including indirect stimulation, the stimulation thresholds of ganglion cells do not vary by a notable amount between healthy and degenerated retina once the synaptic loss due to degeneration is considered. In addition, the stimulation threshold is reduced significantly by considering simultaneous current injection at all electrodes, as expected. A plot of these results is given in Figure 4.5.

4.4.2 Stimulation Range

Near the stimulation threshold computed in the previous section for direct stimulation of ganglion cells, considering a magnitude of 75 μA applied to a single electrode, a total

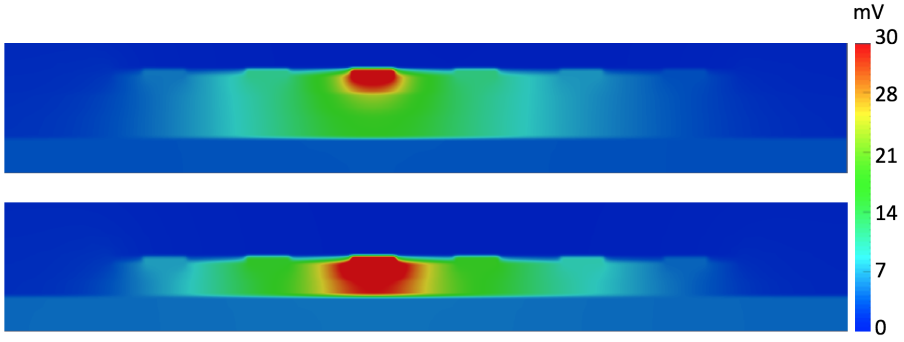

Figure 4.4. Slice of the resulting voltage for a single electrode stimulation for a healthy retina (top) and degenerated retina (bottom).

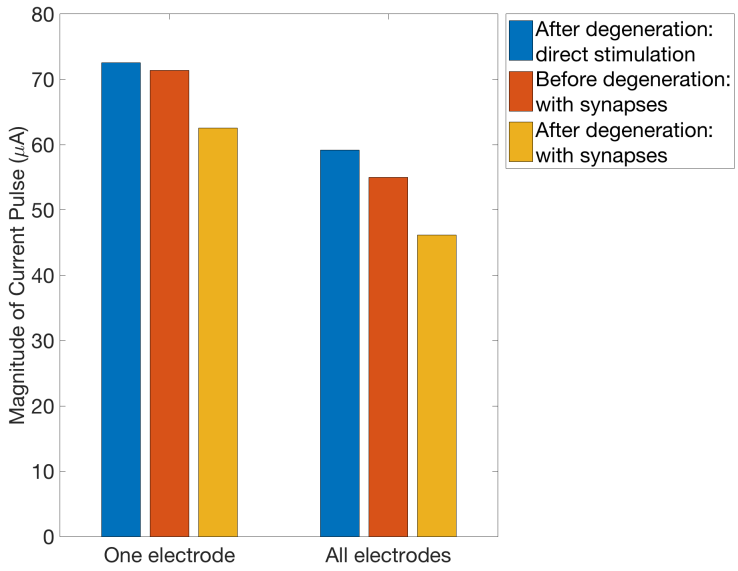

Figure 4.5. Computed stimulation threshold for a given 1ms biphasic pulse for a single electrode, or simultaneous 60-electrode stimulation, considering direct and/or indirect stimulation for retina before and after early degeneration by considering modified retina layer thickness as given in Table 4.I.

of nine cells were activated for retina before degeneration and sixteen cells were activated after shrinking the thickness of retinal layers to represent beginning stages of degeneration. For increased current magnitude, the stimulation range increased, as expected. Figure 4.6 shows the number of ganglion cells stimulated for increased current magnitude, reaching as many as 50 for the degenerated retina at a magnitude of 150 μA, which is within the range of current magnitude used in currently implanted patients [6].

4.4.3 Spontaneous Neural Activity Due to Retina Degeneration

The induced oscillatory membrane voltage in AII cells and passive cone bipolar cells (CBC) matched that of [3] exactly. The response of a single coupled AII-CBC is shown in Figure 4.7.a. By adding excitatory synapses into the model, this oscillatory behavior led to phasic firing in the ganglion cell, with action potentials induced during the sinusoidal crests, as expected. When all 47 AII cells, and appropriate gap junctions with a conductance of 500 pS were included, there was a much higher firing rate during the bursts of ganglion cell activity, still during the crests of the sinusoids in the bipolar cells. Such activity can be tailored in this model by simply adjusting the gap junction conductance or number of cells that exhibit oscillatory behavior. By including inhibition and gap junctions

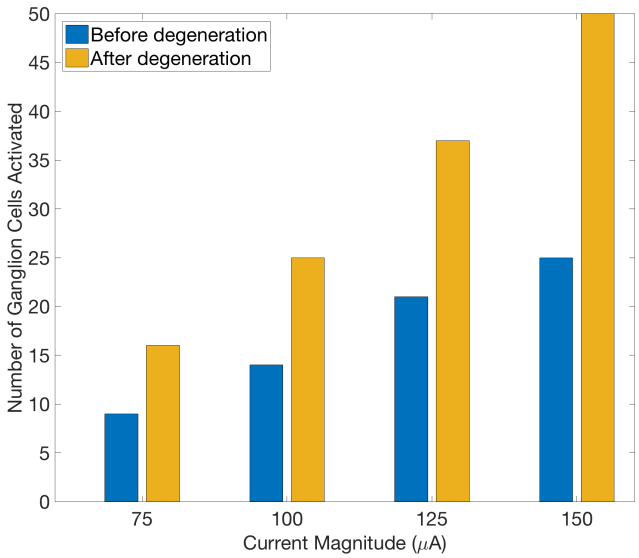

Figure 4.6. Computed stimulation range of ganglion cells, providing the number of ganglion cells stimulated for varying current magnitude and a 1ms wide biphasic pulse.

in the network, the response is a bit more interesting, creating a more spontaneous pattern of ganglion cell stimulation, allowing for indirect stimulation to occur within some of the inhibitory networks in the connectome. Resulting ganglion cell membrane potential for these cases is provided in Figure 4.7. As discussed by Abramian et al., inhibition is important in understanding response to epiretinal electrical stimulation, as in can significantly impact spatial firing patterns, and should be included in computational efforts [40]. In addition, gap junctions, active dendrites and coupling by electrical synapses is also important in order to consider dynamic range [31, 32]. Using this multiscale modeling platform, such features can be considered and altered, allowing for such observations of possible neural behavior in degenerating and electrically stimulated retina.

4.4.4 Stimulation Waveform Design

For designing stimuli for more effective stimulation, decreasing or eliminating spontaneous firing in ganglion cells in degenerating retina, the model in the previous section considering a single AII cell with oscillating membrane potential was considered. As mentioned, a constant-applied current stimuli can reduce oscillatory behavior in the coupled AII-CBC network sufficiently. This was tested, applying a current clamp with varying magnitude to the CBC with oscillating membrane voltage, finding above 20 pA to elim-

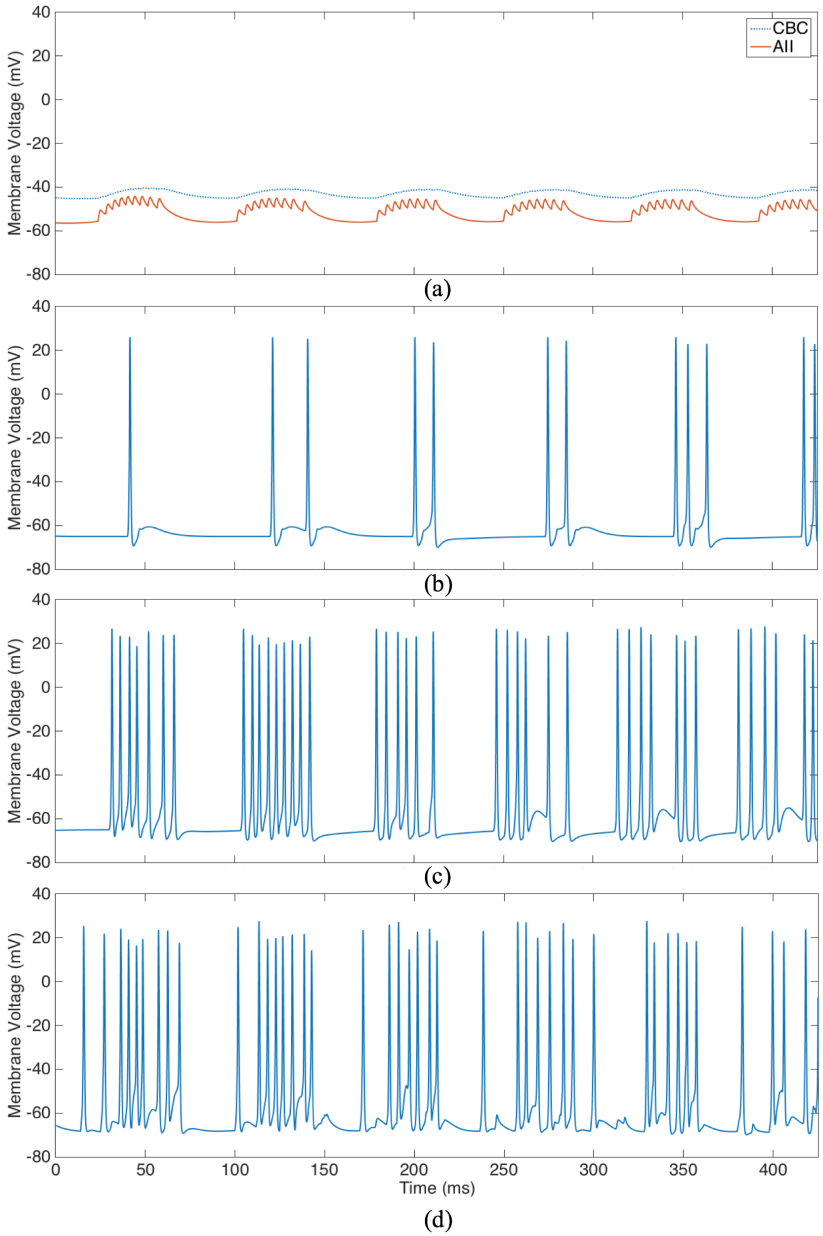

Figure 4.7. Induced spontaneous activity in the retina neural network model without electrical stimulation intervention, showing the membrane potential for (a) a single cone bipolar cell coupled to an AII cell (reproduction of results in [3] with gap junction conductance of 500 pS); (b) ganglion cell that is post-synaptic to the bipolar cell in (a), showing induced spontaneous firing; (c) the same ganglion cell as plotted in (b), but with all 47 AII amacrine cells integrated into the model, coupled with CBC's appropriately via gap junctions, and all excitatory synapses included in the neural network model showing increased firing; and (d) the same as in (c) but with all excitatory and inhibitory synapses and gap junctions included in the neural network model, showing additional spontaneous activity.

inate the low-frequency oscillatory behavior, matching results in [3]. In addition, when above 10 pA was applied, the resulting membrane potential offset and reduced oscillatory behavior was sufficient to completely eliminate spontaneous ganglion cell activity.

The proposed waveform in this paper is to use asymmetric biphasic pulses for stimulating ganglion cells. Wide anodic pulses with low, sub-threshold magnitude can be used to eliminate unwanted ganglion cell stimulation for the duration of the pulse, and narrow, tall, supra-threshold cathodic pulses can be used to cause single ganglion cell action potentials. This allows for increased control over ganglion cell temporal spiking behavior, considering possible oscillatory behavior existing within subjects' degenerated retina.

To study this pulse shape, Admittance Method simulations were run for various pulse widths and magnitudes. An example waveform is shown in Figure 4.8.a, consisting of a width of 1 ms for the cathodic pulse, following currently used stimulation parameters, similar to those used in [15] with a magnitude of 75 μA, which is sufficient to cause stimulation as found in previous results in this paper. The anodic pulse has a width of

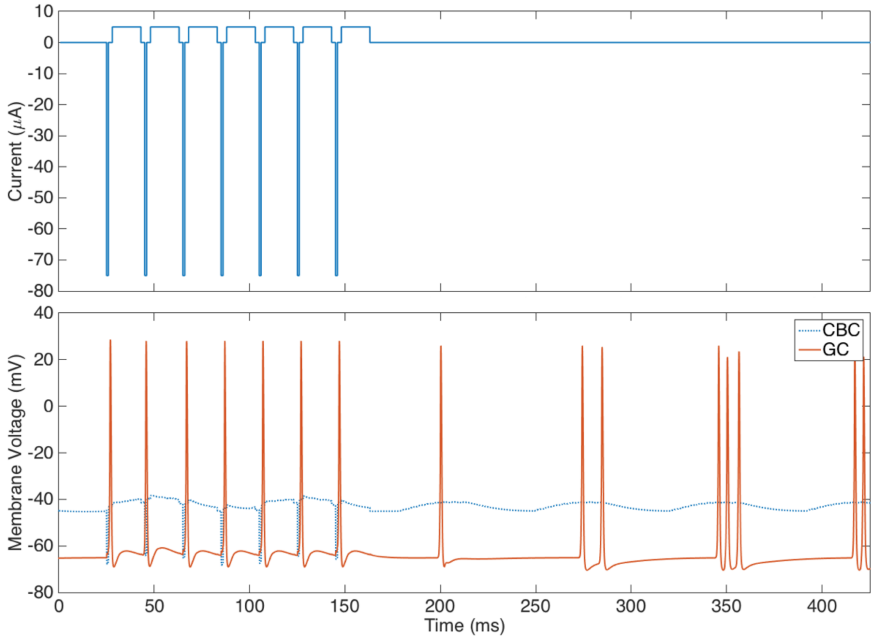

Figure 4.8. Proposed stimulation waveform. (Top) Current stimulus applied in Admittance Method simulation. (Bottom) Ganglion cell membrane voltage showing ability to control spiking, eliminating spontaneous firing and limiting action potential to single firing at the time of cathodic pulse

15 ms and magnitude of 5 μA, which is sufficiently long to stimulate the CBC and reduce oscillatory membrane potential. An interphase gap of 2 ms was considered, which has been shown to increase the efficiency of currently-used biphasic stimuli [51]. The resulting voltage was applied to the neural network model as was done in previous sections, and the resulting CBC, and ganglion cell membrane potential is shown in Figure 4.8.b. The result was, as expected, with spiking in the ganglion cell only occurring during direct stimulation by the cathodic pulse, while the spontaneous activity was subdued by the wide anodic pulses.

In addition to this waveform shape effectively subduing spontaneous activity during electrical stimulation, it is favorable to safety considerations. By choosing the magnitude and duration of the cathodic and anodic pulses appropriately, a charge-balanced waveform is maintained and total charge density and charge per phase remain unchanged from currently used stimuli, following criteria in [72, 73].

4.5 Discussion

4.5.1 Neural Network Modeling

While this modeling effort provides a substantial number of parameters for controlling the extent of neural connectivity and how it may affect the response of retina to electrical stimulation, it has limited horizontal communication. In the simulations for computing the range of stimulation, in which neural networks are tiled into a single model, as shown in Figure 4.2, each network acts independently. In reality, some of the cells in this neural network, including the ganglion cell and amacrine cells extend beyond the 0.25 mm diameter that the connectome used is limited to. Indeed, the ganglion cell dendritic arbor is likely about 0.5-0.7 mm in diameter [74]. In addition, there is horizontal communication across sheets of specific types of bipolar cells, horizontal or amacrine cells, gap junction-coupled ganglion cells, etc., in the retina, all of which may affect the stimulation range that is reported in this computational study. Such horizontal communication was limited in this study in attempt to only include actually observed connectivity as reported in the connectome. Future expansion of this modeling effort can be conducted for constructing a more accurate representation of retina neural tissue.

4.5.2 Retina Degeneration

In addition to the neural network modeling limitations, the bulk-tissue level models used for simulating extracellular voltage due to electrical stimulation maintains a layered structure for the retina. This is consistent with literature for early phases of degeneration, but does not extend to later phases, during which electrical stimulation prosthetic intervention is implemented. During the neural remodeling and continual neurodegeneration phases, there are substantial modifications to the retina anatomy, including cell migration, and cellular death that continues until nearly 90% of the cells are gone. This practically eliminates the structure of layered tissue with homogeneous electrical resistivity as seen here, as shown in Figure 4.9, and calls for a more complex heterogeneous representation of the tissue.

In addition to the added spontaneous ganglion cell activity that is considered in this paper, there are further molecular reprogramming events during remodeling, including completely new connections, glutamate receptor revisions and altered Muller cell functionality [75]. None of such features are incorporated into the modeling structure as of

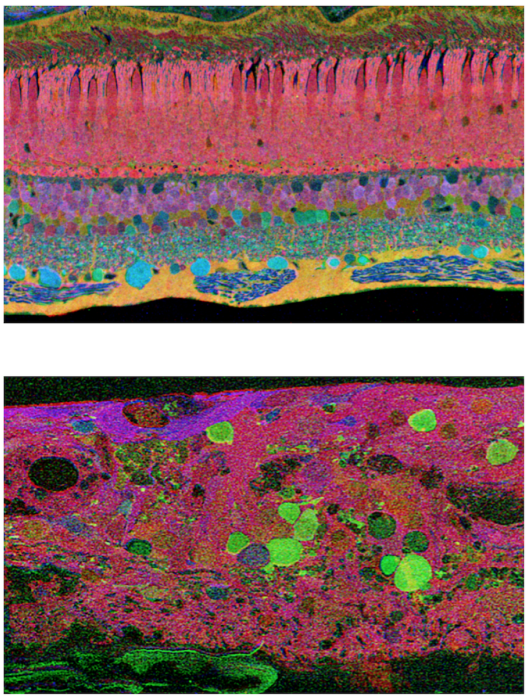

Figure 4.9. Images of retina, both before degeneration (top) and after extensive degeneration due to retinitis pigmentosa (bottom).

yet, and consequences on attempted electrical stimulation is unknown. The modeling framework presented here has the ability to include all mentioned features, altering the heterogeneity of the tissue and network connectivity.

4.5.3 Electrode Design

Comparing with clinical data, the stimulation thresholds reported from this computational study are on the lower end of what has been observed. A reason for this is likely the location of the electrodes in this model. As discussed in [6, 15], the distance between the retina surface and the electrode array can vary from patient to patient and can increase over time. This leads to an increased electrode impedance and stimulation threshold. This can certainly be considered in the modeling framework provided in this paper to study how the electrode distance affects the stimulation threshold and range.

4.5.4 Implications for Clinical Applications

Currently the timing of implantation is late in disease, after patients have undergone years of disease and have become blind. As such, extensive retina remodeling and neurodegeneration has occurred by the time electrical stimulation rehabilitative techniques are attempted. This makes the proposed waveform in this paper highly clinically relevant, considering some spontaneous behavior that occurs during remodeling in the design of the waveform. As discussed by Weiland and Humayun in [14], only 55% of electrodes in current patients are effective independently. Applying the waveform proposed here, this number can hopefully increase. Asymmetric biphasic pules have been considered in previous experimental studies [51]. However, the ability to scale this to clinical application still needs to be investigated to validate added effectivity.

4.6 Conclusion

In this paper, a multiscale multiphysics computational framework for modeling electrical stimulation of degenerated retina was proposed. Using this framework, the effects of cellular network connectivity, anatomical changes, and spontaneous activity observed in degenerated retina on electrical stimulation attempts were investigated. This provided computed stimulation threshold and range of ganglion cells for varying degrees of degeneration. Through observations of such studies, a waveform shape with increased ef-

fectivity in degenerated retina was proposed, applying asymmetric biphasic pulses for reducing spontaneous neural activity and allowing increased control over the timing of ganglion cell action potentials. The authors hope for such results to increase the effectivity of currently-implanted devices, and for the proposed modeling framework to continue to provide understanding of retina neural behavior, how it changes during degenerative disease, and provide additional recommendation for further increased stimulation efficiency and efficacy in prosthetic devices for restoring vision.

CHAPTER 5

VIRTUAL ELECTRODE DESIGN FOR INCREASING SPATIAL RESOLUTION IN RETINAL PROSTHESIS

Reproduced by permission of the Institution of Engineering and Technology, from: K. Loizos, C.J. Cela, R. Marc, and G. Lazzi, "Virtual electrode design for increasing spatial resolution in retinal prosthesis," *IET Healthcare Tech. Lett.*, vol. 3, no. 2, pp. 93-97, 2016.

5.1 Abstract

Retinal prostheses systems are currently used to restore partial vision to patients blinded by degenerative diseases by electrically stimulating surviving retinal cells. In order to obtain likely maximum resolution, electrode size is minimized, allowing for a large quantity on an array and localized stimulation regions. Besides the small size leading to fabrication difficulties and higher electrochemical charge density, there are challenges associated with the number of drivers needed for a large electrode count as well as the strategies to deliver sufficient power to these drivers wirelessly. In hopes to increase electrode resolution while avoiding these issues, we propose a new "virtual electrode" design to increase locations of likely stimulation. Passive metallization strategically placed between disk electrodes, combined with alternating surrounding stimuli, channel current into a location between electrodes, producing a virtual stimulation site. A computational study was conducted to optimize the passive metal element geometry, quantify the expected current density output, and simulate retinal ganglion cell activity due to virtual electrode stimulation. Results show this procedure leads to array geometry that focuses injected current and achieves retinal ganglion cell stimulation in a region beneath the "virtual electrode," creating an alternate stimulation site without additional drivers.

5.2 Introduction

Most of currently implemented epi-retinal prosthesis systems utilize arrays of surface electrodes placed against the retina. These electrically stimulate the neural tissue based on modulated input from an external camera [45]. This has produced encouraging results, allowing blind patients who have degenerative diseases to regain some visual perception [15, 47]. However, the resolution is not yet sufficient to accomplish important tasks, such as facial recognition, and it is widely believed that a larger number of electrodes would likely provide a more useful vision in this regard [8, 76]. There are restrictions on how many electrodes can be placed on these arrays and how small they can be. More importantly, there are significant limitations on how many electrodes can be driven by separate drivers and the power required by attempting to increase the electrode count through simply increasing the number of physical electrodes. Further, to fit a large number of electrodes, the size of the electrodes and the space between them needs to decrease. This leads to further constraints, since the smaller size has been shown to increase the impedance at the electrode surface, which increases the amount of charge density and the risk of damaging tissue and/or the electrodes themselves [8, 77]. Closer spatial proximity of electrodes also weakens the focus of stimuli, as charge injection from surrounding electrodes can affect the response beneath any individual electrode when they are concurrently utilized. This can lead to a large stimulation range and discredits the logic for increasing the number of electrodes [78].

Alternative stimulation strategies have been studied to create virtual stimulation sites beneath these electrode arrays, channeling current to locations in between electrodes [52, 79–81]. This bypasses concerns with building arrays with many small electrodes, and allows for currently implanted designs to continue to be used while providing higher resolution of stimulus locations. Computational and experimental studies have shown that using simultaneous monopolar stimulation of adjacent electrodes increases the field between them, and can theoretically be used to stimulate these regions [52, 80, 81]. Choosing different ground locations to channel current is another option [34, 81].

While these methods have been shown to increase the fields between electrodes and can cause stimulation, they do not create a focused current injection that would be expected if another electrode were placed in the center virtual location. This work introduces a

design for a virtual electrode configuration that channels current to the center of the array, producing as high of a current density beneath the virtual electrode as is seen under a firing electrode, while ensuring that the tissue beneath the electrodes does not respond to the injected current. This is accomplished through the usage of short pulses applied to perpendicular pairs of bipolar electrodes, and strategically placed passive metal elements for channeling the current to a specific location in the center of each set of four electrodes. Applying this electrode configuration can significantly increase the number of acting "electrodes" on an array. This can lead to improved array design, providing a means for increasing the resolution and for selectively stimulating cells within a small radius of tissue.

5.3 Virtual Electrode Methodology

The virtual electrode phenomenon is produced using a purposely designed configuration of passive metal elements placed in between active disk electrodes, in conjunction with a judicious choice of signal timing and shape of the adjacent electrodes. The design proposed in this work is shown in Figure 5.1. This is accomplished through the use of time-offset pulses, as in [79, 80], applying pulses with a short enough of a pulse-width that they are uninfluential on the tissue, but offset in time so that they create a wider pulse in the location between the electrodes. As described as well in [79, 80], applying a short stimulus to two adjacent electrodes, having one stimulus be a delayed by the width of the stimuli, produces a stimulus of twice the width in the center. If this pulse width is too narrow to elicit neural response, then the center location could be the sole location of neural stimulation. Differently from previous attempts at this strategy, bipolar stimulation is used rather than monopolar, using the diagonal, perpendicular pairs of electrodes in any given set of four electrodes for the two stimuli. A narrow anodic stimulus is applied to one pair, then immediately following it an identical stimulus is applied to the second pair.

This systematic current injection used in conjunction with the designed passive metal elements focus the current even further in order to produce sufficient charge density to cause a stimulus site in the center of the structure. The passive metal elements provide a highly conductive path from the positive electrode to the negative, forcing more of the current into this specific location. Incorporating a gap between the pieces of metal in the

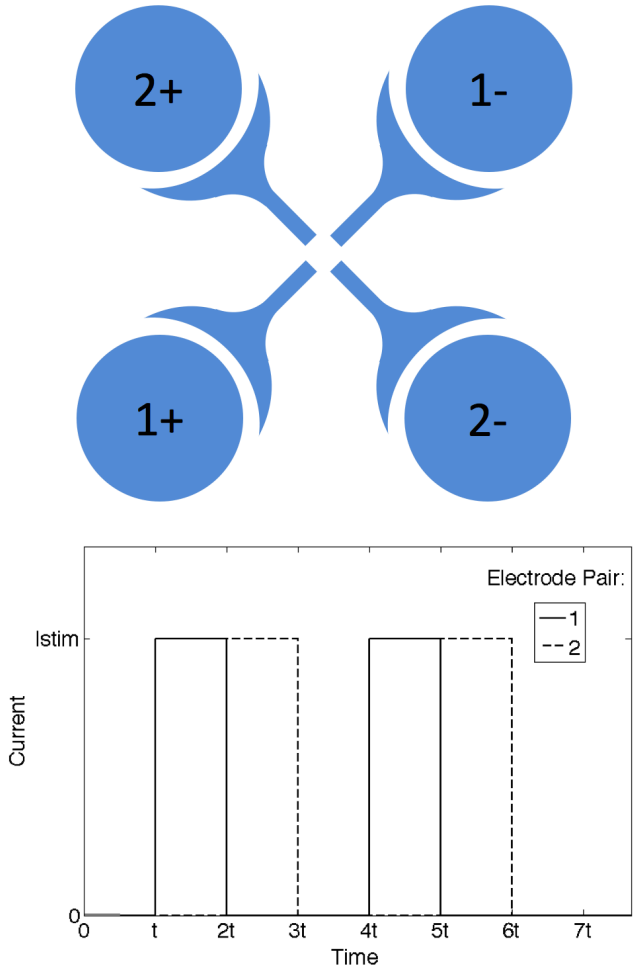

Figure 5.1. Virtual electrode system: Alternating pulses are applied to electrode pairs 1 and 2, with a pulse-width of t, creating a pulse-width of 2t in the center. Passive metal elements are incorporated to further focus the current.

center of the four electrodes provides capacitive pathways for the current, creating a high current density location in this center location. The initial idea for this methodology was based on the observation of current traveling through adjacent electrodes and then into the tissue when electrodes are placed in close proximity, since the electrodes nearby form a more conductive path to the current return than the tissue.

5.4 Electrode Array Model and Tools

For the purposes of designing the electrode configuration and simulating various geometries, a computational model was constructed with a size of 300x300x150 voxels for use with our multiresolution and multiscale admittance method, described in [17, 44]. Each

voxel is cubic with a width of 10μm and is given an integer value, each integer representing a different tissue or material resistive properties. A 2x2 electrode array was added, comprised of disk electrodes with a diameter of 200μm and a pitch of 400μm, embedded in insulating material, with the surface of the electrode flush with the surface. The electrode dimensions and placement were based on the retinal prosthesis system reported in [45].

The electrode array is placed flush with the retinal surface. The retina was described using multiple layers, with the resistivity varying every 20μm beneath the surface of the array corresponding to published measurements of rat retina [1]. The relative permittivity of all of the retinal tissue was varied based on the width of the time-step used for the bipolar stimulation, ranging from 4700 to 8200. The tissue surrounding the electrode array was given the properties of vitreous humor, with a relative permittivity of 98 [67].

The admittance method (AM) was used to compute resulting voltages due to defined current source(s). This method first meshes the model, combining voxels at locations further from boundaries and current source locations in order to decrease the number of nodes. Next, the meshed discretized model is used to build a circuit network based on the resistivity and permittivity values, describing each edge of a voxel as a resistance and capacitance. An admittance matrix is populated with the resulting admittance values seen at each node (G). By defining a current vector (I) that defines the initial current at each node, allowing for current sources to be defined, the resulting voltages throughout the model (V) can be solved for using the linear equation GV=I. These voltages may then be used to solve for the electric field magnitude in any direction by taking the ratio of the voltage drop between adjacent nodes and the distance between them. The current density may then also be considered by scaling the magnitude of the electric field at each voxel by the conductivity of the tissue the voxel represents [17, 44].

5.5 Passive Metal Element Design

The admittance method was used to optimize the geometry of the passive metal elements placed in between the electrodes. The metal geometries were designed to be 10μm thick, placed flush with the surface of the array without any sources connected. Simulations were run, applying a total of 4 anodic pulses, as shown in Figure 5.1, with a pulse width of 10μs. Many different configurations were considered: it was found that

having the metal surrounding the firing and return electrodes produced a higher density of current in the center and, as described in the later section, is most effective in causing neural activation in regions proximal to the center of the set of electrodes. By narrowing the metal elements, the amount of current that passed across proximate elements was decreased, channeling more current towards the center. Three notable patterns describing this conclusion are shown in Figure 5.2.a, with each subsequent pattern having a narrower geometry. Normalized current density accumulated after these four time-steps at a slice

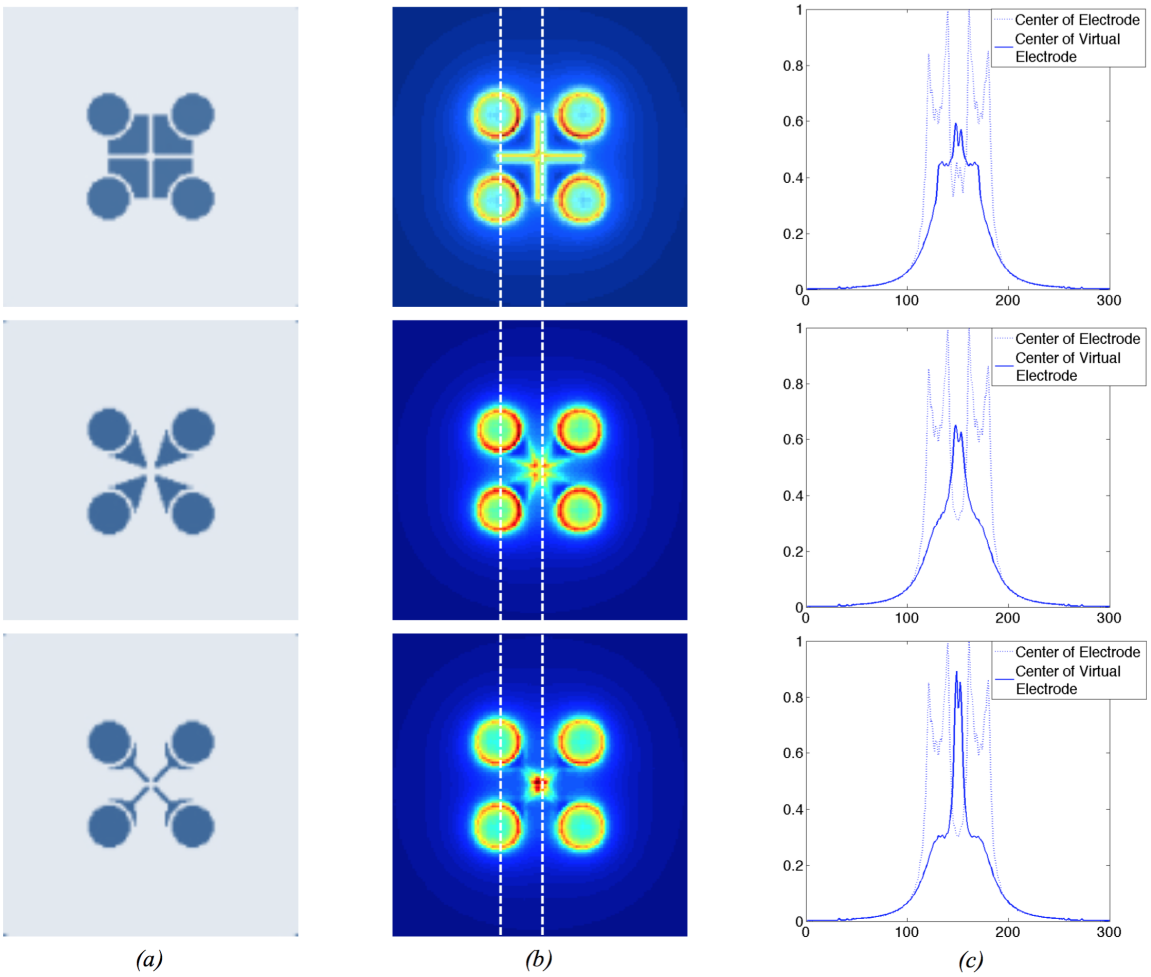

Figure 5.2. Three notable patterns of electrode and passive metal element and linear plots of normalised current density. (a) Electrode and passive metal element pattern; (b) normalised accumulated current density after four time steps (two pulses applied to each pair), taken 30 µm into the retinal tissue for each pattern; (c) linear plots of normalised current density comparing magnitude between firing electrodes and the virtual electrode (location given by white dotted lines in (b))

30μm into the retinal tissue is given in Figure 5.2.b. Figure 5.2.c provides linear plots of these slices, quantifying the difference between the accumulated current density through the electrodes and through the virtual electrode. All plots were normalized to the maximum current density magnitude in order to provide a comparison of the effective current channeling between the different configurations.

5.6 Neural Activation Modeling

The resulting accumulated current density analysis showed an interesting ability for this system to channel current towards the center of a square electrode configuration. However, the current density beneath the firing electrodes, built over the time of multiple pulses, remained at a similar magnitude to that under the virtual electrode location. The ability for this stimulation mechanism to be useful depends on the underlying retinal cells responding to the longer pulse width in the center, and not to the shorter pulses beneath the firing electrode locations. Thus, a further study was conducted to simulate the response of retinal ganglion cells. A multiscale approach was taken, applying the voltage results from the admittance method simulations to a model of a retinal ganglion cell. The cell was placed in multiple locations, using an otherwise identical model. Since the admittance mesh is a lumped representation of the underlying neural cells, this multiscale process sufficiently models the impedance of each individual cell. This approach allows for a comparative study of the stimulation threshold for cells in different locations beneath the electrode array.

A retinal ganglion cell (RGC) model was built from morphology extracted from a connectome dataset built off of high-resolution Transmission Electron Microscopy (TEM) images [18]. The RGC considered includes a cell body and the dendritic branches. The morphology was imported into NEURON software [5], in which it was split into compartments of tapered cylinders, each described electrically as a cable model. The active properties of the membrane were described using the passive properties and five-ionic current model as described by Fohlmeister et al. [58] The ionic gating rate constants and ionic channel conductances were given identical values to measurements given in [82]. The ability of this cellular morphology to behave as observed experimentally with these active properties applied was simulated by clamping the membrane to various current magnitudes, and

comparing the resulting spiking to the results given in [58].

This RGC was duplicated to create two models. The coordinates of the RGC's were translated in order to be centered 30µm into the admittance model described in the previous sections of this paper, with one cell being beneath one of the firing electrodes and another beneath the virtual electrode. Only the model with the electrode configuration shown in Figure 5.1 was considered since it resulted in the most focused current density in the virtual electrode location. The placement of the cells within the admittance model is shown in Figure 5.3. The voltages throughout the admittance model that resulted from

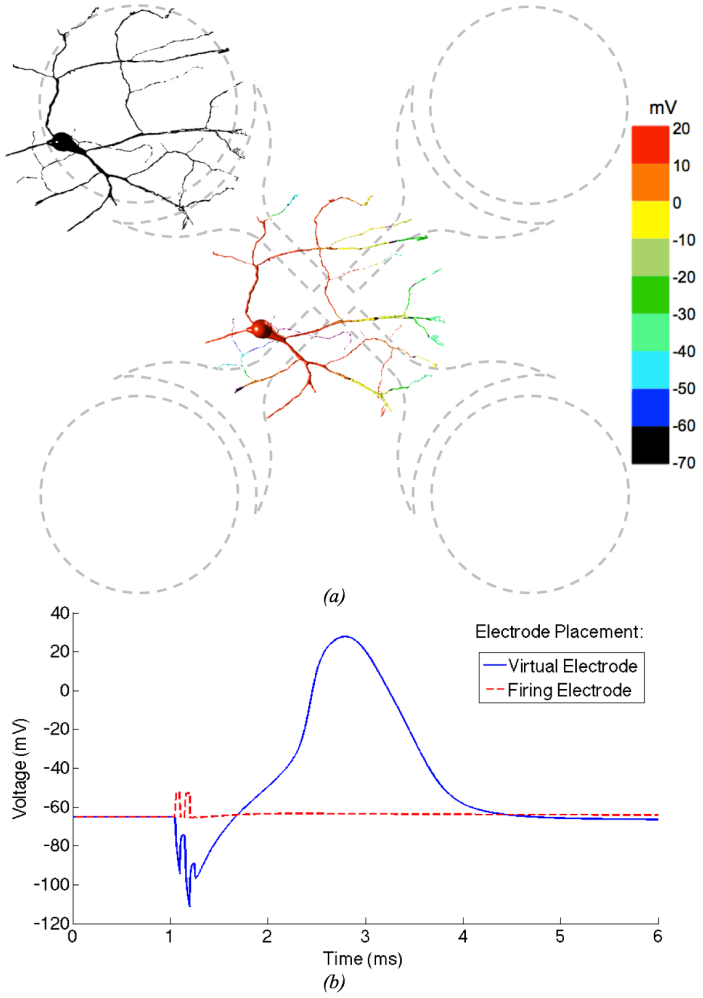

Figure 5.3. Placement of the cells within the admittance model. (a) Three-dimensional rendering of ganglion cells beneath virtual electrode and firing electrode, coloured according to membrane voltage 1.75 ms after 50 µs-wide 250 µA pulse applied, showing only activation in virtual location. (b) Membrane voltage over time for the same stimulus

the current density analysis were interpolated, providing a potential at each compartment of these two RGC models. These voltages were then applied as extracellular voltages, by placing voltage sources in series with the membrane circuit at each compartment. [41]

Simulations were then run, analyzing the cellular response to the voltages resulting from previous AM simulations. The input voltages were linearly scaled in NEURON until activation of both cells was observed. For this initial simulation with a pulse width of 10μs, a current magnitude of 1670 μA was required for the cell beneath the firing electrode to activate, while only 700 μA were required for the cell beneath the virtual electrode location. As expected, the shorter pulse width applied to the firing electrode required a much higher magnitude to cause stimulation than the wider pulse width in the center of the electrodes.

The AM simulations were repeated for different pulse widths, varying from 10μs to 100μs, modifying the permittivity values appropriately for each case. The magnitude of the interpolated extracellular voltages was again scaled until activation was observed to compute the stimulation threshold. Results of the threshold calculations are given in Figures 5.3 and 5.4, indicating that this configuration can provide a virtual electrode stimulus regardless of the pulse width.

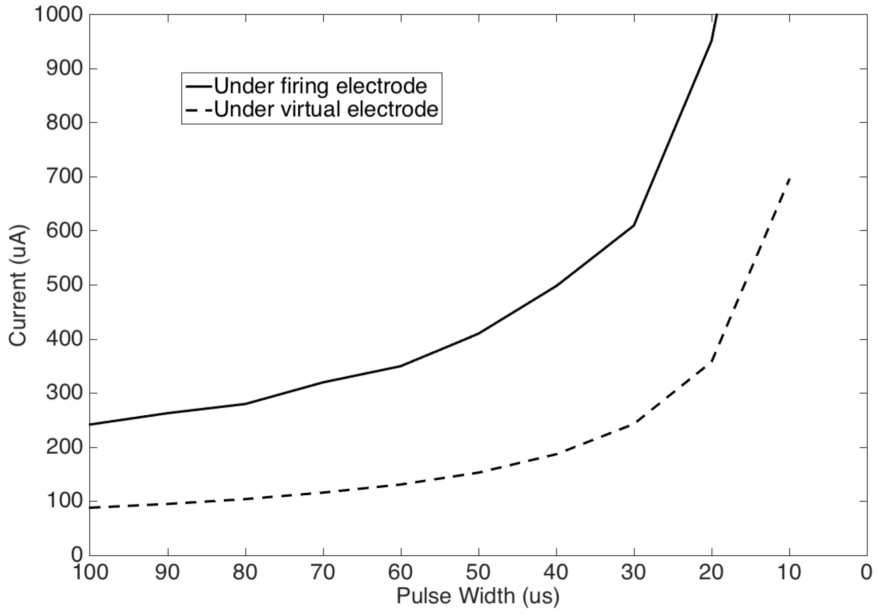

Figure 5.4. Minimum current magnitude necessary to be applied to the electrodes in the AM model in order to stimulate an RGC beneath a firing electrode and the virtual electrode for varying pulse width.

At these current thresholds, the charge density and charge per phase beneath the firing electrodes were computed to analyze potential safety implications, as these parameters have been shown as cofactors in potential neural tissue damage using disk electrodes [72]. The charge per phase was calculated by multiplying the current waveform pulse width by the magnitude of the pulse at the threshold. The charge density per phase was then calculated by dividing the charge per phase by the area of the electrode. All current threshold and pulse width combinations presented in this paper were well within the boundaries for safe stimulation as proposed in [72].

5.7 Conclusions

An electrode configuration for surface electrode arrays used in retinal prostheses systems was designed in order to provide an extra virtual stimulation site in the center of sets of electrodes. Through a computational study, the method of using alternating short pulses applied to perpendicular bipolar electrodes, with focusing passive metal elements, was shown to have the ability to create virtual electrodes. This could have significant implications for future implanted surface electrode arrays, being able to provide a finer resolution of selectively stimulated retinal cells without the necessity for more feed points, or drivers.

5.8 Funding and Declarations of Interest

This work was supported by the National Institute of General Medical Sciences of the National Institutes of Health under award number 1U01GM104604-01. Dr. Loizos, Dr. Cela, and Dr. Lazzi report grants from the U.S. Department of Energy during the conduct of this study and grants from Second Sight Medical Products (SSMP) Inc. outside this work. Dr. Marc reports grants from the National Eye Institute during the conduct of this study. Dr. Cela and Dr. Lazzi have a patent issued relevant to this work in US Patent No. 9,155,879 B2.

CHAPTER 6

HIPPOCAMPUS PROSTHETIC ELECTRODE PLACEMENT FOR INCREASED STIMULATION EFFICIENCY

 A. Gilbert, K. Loizos, A.K. Ram-Rakhyani, P. Hendrickson, G. Lazzi, and T.W. Berger, "A 3D admittance-level computational model of a rat hippocampus for improving prosthetic design," *Proc. IEEE 37th Eng. Med. Biol. Soc. Conf.*, 2015.

6.1 Abstract

Hippocampal prosthetic devices have been developed to bridge the gap between functioning portions of the hippocampus in order to restore lost memory functionality in those suffering from brain injury or diseases. An approach taken in recent neuroprosthetic design is to use a multiinput multioutput device that reads data from the CA3 in the hippocampus and electrically stimulates the CA1 in an attempt to mimic the appropriate firing pattern that would occur due to coupling between the two regions during normal memory function. However, further study is required to identify most advantageous electrode placement and stimulation parameters for inducing appropriate firing patterns. This chapter describes the creation and implementation of a computational model of the hippocampus to simulate the electric field and neural activation from external electrical stimulation, extending the modeling approach for studying retina prosthetic devices presented in previous chapters.

6.2 Introduction

The hippocampus is a segment of the medial temporal lobe associated with long-term memory creation. Any impairment of the hippocampus can lead to decreased memory accuracy, and has been shown to be linked to memory loss in those suffering from

Alzheimer's disease, dementia, cerebrovascular disease, or traumatic brain injury. While there exists a wide range in the severity of these diseases, they often result in long-term physical, emotional, and behavioral effects, with an accompanying decrease in quality of life. In order to address this and design a system to restore memory functionality, research has been conducted to understand the factors within the hippocampus that are involved in memory retention, concluding that the firing patterns between regions of the hippocampus are vital in the encoding of long-term memories. Berger et al. have designed a system to bypass impaired hippocampal regions [11]. This prosthetic records neural spiking patterns from two regions, predicts if a memory will be encoded properly or not, and uses an online model to estimate the required firing patterns in the further upstream region for a properly encoded memory. Stimulating electrodes are then used in attempt to induce the predicted patterns.

This system has proven effective in restoring and/or enhancing memory retention in rodents and primates [11, 12]. However, a clear understanding of ideal electrode placements and geometries, and stimulation patterns are relatively unknown, and current knowledge is mostly based on empirical observations. Before HPDs can transition to human clinical trials, it is crucial to understand current stimulation thresholds and the most advantageous electrode placement, providing the least-invasive implementation while minimizing charge injection and maximizing functionality. In this chapter, a computational model of rat hippocampus and implant electronics is constructed for modeling resulting electric field due to systematic electrical stimulation. This is coupled with a model of the underlying neural tissue to investigate resulting neural activity. CA1 pyramidal cells are considered, along with electrode geometry following that of the mentioned rat in vivo experiments showing memory restoration, with the goal of providing recommendation of the depth the microwire electrodes need to be placed at in the hippocampus for minimal injected current magnitude.

6.3 Methods

6.3.1 Model Construction

The hippocampus model used in this paper was created from a dataset based on MRI images of a rat hippocampus, classifying 10x 10 to the 6 different points according to their

position, section of hippocampus, and layer [83, 84]. Software was written to convert the data into a 16 μm resolution 3D matrix of cubic voxels. Each voxel was assigned a material index which corresponded to its section and layer, where the section refers to CA1, CA2, CA3, or DG, and the layer refers to either the the Lacunosum-Moleculare (LM), Radiatum (RAD), Pyramidal Cell (PC), or Oriens (OR) [83]. This segmentation is shown in Figure 6.1. Each material index was then assigned an electrical resistivity value based on its layer as shown in Figure 6.2 [85, 86]. Due to the unavailability of measured resistivity profiles in the dentate gyrus, the entire hippocampus resistivity was assigned parameters based on measurements taken in CA1, using values as reported by Lopez-Aguado et al. [87]. Many measurements were performed in these experimenters in the apical and basal dendritic regions, cell body layer, stratum lacunosum-moleculare, and the hippocampal fissure bordering the outer boundary of the dentate gyrus. The measurements showed remarkably similar resistivity in the molecular regions, around 2.7 μm, with approximately double the resistance in the cell-body regions. This led to the layered structure of this computational model, with each region having homogeneous resistivity.

Voxels that were undefined in the original dataset were interpolated and assigned a

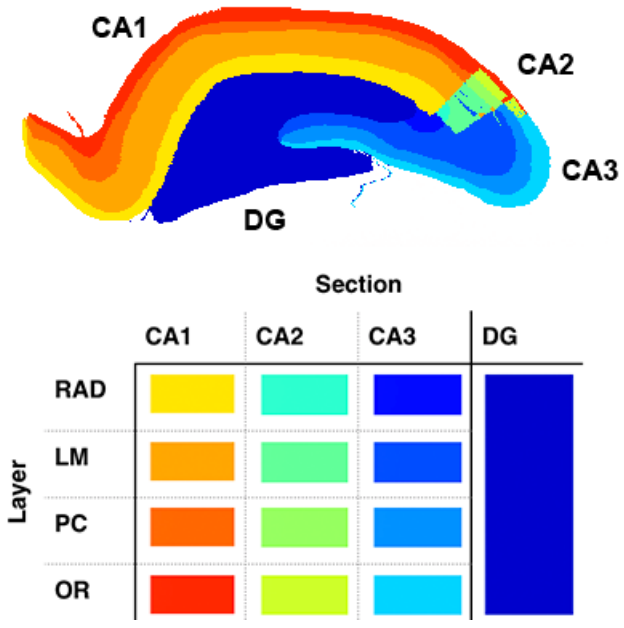

Figure 6.1. (Top) 2D slice of the Admittance Method hippocampus model, and (bottom) a chart with the definitions of the anatomical sections used to discretize the tissue.

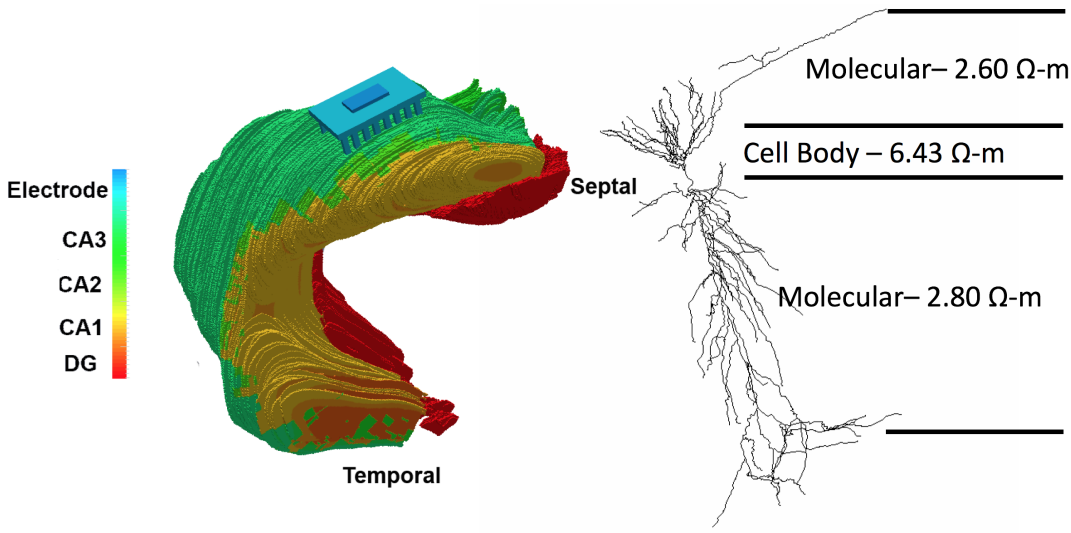

Figure 6.2. (Left) Rendering of 3D hippocampus Admittance Method model including an implanted electrode array, and (right) a rendering of the CA1 pyramidal cell considered in this study, annotated with the bulk resistivity value applied to the Admittance Method model based on cellular region.

tissue type based on the surrounding material. However, this method did not eliminate larger natural spaces that occur in the hippocampus due to irregularities or connections to surrounding tissue. The initial dataset also contained voxels that were separated by as little as 4 μm in the x and y dimensions and 16 μm in the z dimension. To increase computational speed and maintain uniform dimensions, the resolution was set to 16 μm in all dimensions. The final model size was 475x500x288 voxels.

An electrode model was constructed to replicate the physical device used in prior rat experiments [88], including a row of 8 recording microwire electrodes and a row of 8 stimulating microwire electrodes. The diameter of each electrode was set to be 48 μm. The electrode model was inserted into the hippocampus model so the first row (recording) ended in the CA3, while the second row (stimulating) ended in the CA1, near the cell body layers. A conductive plate was inserted above the electrode array to serve as a common ground for simulations. The 3D model of the hippocampus with the electrode array implanted is shown in Figure 6.2. Model and electrode creation methods were implemented in Python while merging methods were implemented with C++. The Admittance Method was then used for computing the voltage at each node in the model due to a given current stimulus applied across any pair of electrodes in the 8x2 array.

6.3.2 Linking with NEURON Model

To simulate stimulation thresholds, a model of a CA1 pyramidal cell was considered, developed by Poirazi et al. [89]. This is a complex model, using a modified Hodgkin-Huxley formulation similar to that of the previously mentioned retinal cells, with 17 ionic channel mechanisms. It had been characterized and calibrated based on a series of experimental studies, showing the ability to mimic the response to extracellular stimulation, when either a single pulse or train of pulses was applied. These features made it particularly attractive to this study, in which as realistic of a response to electrical stimulation is desired in order to provide computational results towards recommendations for stimulation parameters in future experiments. Before implementing the model in this study, the results provided by Poirazi et al. were replicated to ensure that the model functions as expected. It was then coupled with the bulk-tissue level model in the previous section in a similar manner as described in Chapter 2, by considering the cell to be translated to an appropriate location within the bulk-tissue, interpolating the extracellular voltage resulting from Admittance Method simulation at the locations of the center of each compartment within the NEURON model, and applying these voltages as extracellular sources. The positioning of the model was set to match the anatomy of the hippocampus, with the cell body centered in the cell body layer of the CA1 region, with the dendritic branches extending into the molecular regions, at an angle normal to the direction of the cell body layer. The size of the cell closely matched that of the CA1 region in the Admittance Method model, requiring no modifications to either model. Figure 6.2 provides a rendering of the cell.

6.3.3 Prosthetic Microwire Electrode Depth

One of the main goals of this work was to identify the most advantageous electrode placement for this hippocampus prosthetic device, referring to the ability to stimulate neural tissue in the area near the electrode surface while remaining minimally invasive and with minimal current injection. Requiring the electrodes to be inserted into the hippocampus can increase the risk of damaging the neural tissue, and is to be avoided if possible. The microwire electrode array described earlier in this section was shifted to various depths in the CA1 region of the hippocampus, considering locations near the

surface of the hippocampus, at the cell body layer, and at one and two thirds into the LM layer. Simulations were run, applying 50 μA 1 ms wide biphasic pulses. The resulting voltage was interpolated and applied to the CA1 cell model, which was positioned 48 μm offset from the microwires, to avoid the electrodes from running directly through the cell. The applied extracellular voltage was scaled until a threshold magnitude was found.

6.3.4 Neural Network Dynamics

The modeling in the previous sections provides results towards recommendation of electrode placement and stimulation thresholds for a single cell in the CA1. However, the cellular density in the hippocampus is high, containing millions of cells in a rat hippocampus [13, 48] along with neural network functionality that is neglected by considering only a single cell response. In order to investigate the impact this may have on computational results of electrical stimulation of hippocampal tissue, the model presented here was expanded to include a large-scale model of the dentate gyrus in the hippocampus, including over 1 million granule cells, feedback and feedforward input resulting from interneurons and perforant path axons that provide input from the entorhinal cortex and affect the dynamics of cells downstream in the dentate gyrus and CA sections. The dentate gyrus was considered due to the availability of a large-scale model that has not yet been extended to the CA. Using this model, approximated spatiotemporal dynamics are included in the estimation of induced activity due to electrical stimulation. This work was conducted in collaboration with Phillip Hendrickson, Clayton Bingham, Gene Yu, and Theodore Berger at the University of Southern California, and will be used in future work towards furthering the understanding of neural tissue response to such hippocampus prosthetic electrical stimulation as this neural network model is extended to the CA3 and CA1 sections of the hippocampus.

For this study, the 3D model of the hippocampus was reduced to a 400 μm thick slice of hippocampus, simplifying the computation time while still providing sufficient tissue to comprise the large-scale neural network model. A rendering of this model is given in Figure 6.3. The large-scale model originally had no spatial relevance, considering the C-shaped tissue of the dentate gyrus to be ”flattened” into a 2D plane. In order to estimate the location of each neural compartment, the coordinates of each compartment

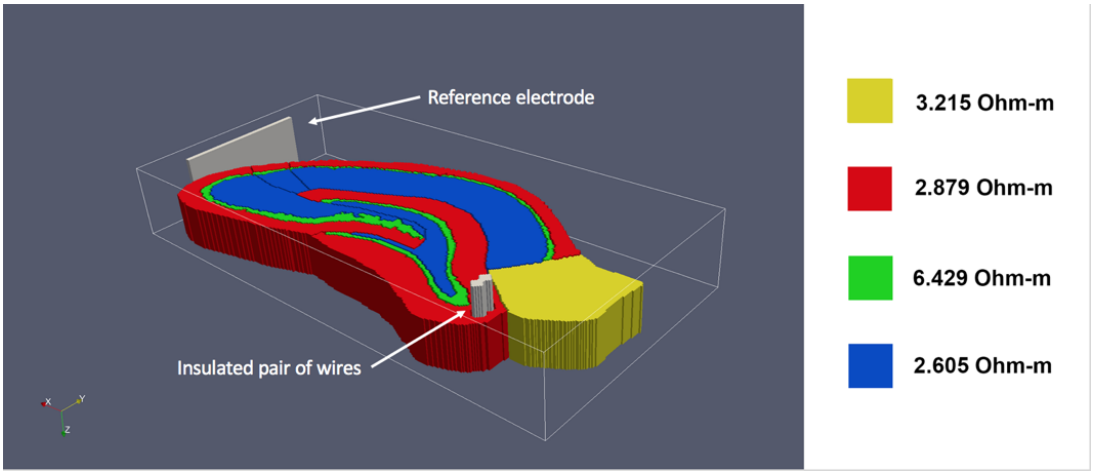

Figure 6.3. Rendering of the 3D model of a hippocampus slice with implant electrodes, used for simulating the dentate gyrus response to electrical stimulation towards predicting the electrode placement for the highest stimulation efficiency.

were considered to be translated to the cell body layer of the dentate gyrus in the 3D AM model, with the dendritic branches being rotated to an angle normal to the cell body layer at each respective position. Recording the coordinates of each compartment after translation and rotation, and noting which compartment each of the coordinates refer to allowed for the AM results to be interpolated and the resulting voltage to be applied to the large-scale neural network appropriately.

Electrodes were incorporated into the model in 9 different locations in the dentate gyrus, as shown in Figure 6.4, in order to find the most advantageous electrode placement for a given current magnitude, providing maximal population spiking. This included electrodes placed above the cell bodies and perforant path axons that provide input from the entorhinal cortex and travel along the length of the dentate gyrus in order to include the effects on cellular activation in downstream regions of the dentate gyrus.

6.3.5 Heterogeneous Resistivity

Because no knowledge of the dentate gyrus bulk resistivity is provided in literature, a study of how changing the resistivity heterogeneity can affect the response to electrical stimulation was conducted. The resistivity was initialized to that of the CA sections, based on the CA1 measurements used for the remaining sections of the hippocampus, applying homogeneous resistivity to the cell body and molecular layers, with the cell body

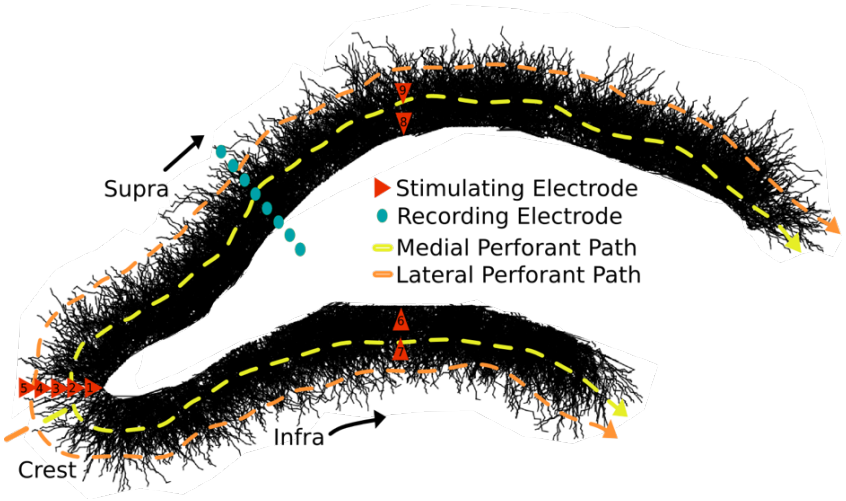

Figure 6.4. Rendering of the 1-million-plus dentate gyrus large-scale NEURON model with annotations showing electrode placement and approximate perforant path axon locations.

regions having higher resistivity. The anatomy of the dentate gyrus is similar to the CA sections, providing an applicable approximation of the bulk-tissue resistive properties. To justify using this heterogeneous model with somatic regions distinguished by their higher electrical resistivity (as compared to a simpler homogenous model that could be represented analytically), and to investigate the how error in this approximation of dentate gyrus resistivity based on CA measurements would affect electrical stimulation results, simulations were run varying the ratio of resistivity between the cell body and molecular regions. The original ratio of the cell body layer to molecular layer was 2.28 and that ratio was varied in a series of simulations from cell body layer/molecular layer = 1 to cell body layer/molecular layer = 5. These simulations were run with a pulse width of 1 ms and amplitude of 100 μA and no other parameters were changed from the control model. Simulations in the NEURON model were subsequently performed in order to determine how these differences in the extracellular voltage field might affect activation in the large-scale model.

6.4 Results

6.4.1 Field Distribution

A biphasic current stimulus with a magnitude of 100 μA and pulse width of 1 ms was applied to each bipolar pair of electrodes. Figure 6.5 shows a plot of the resulting voltages

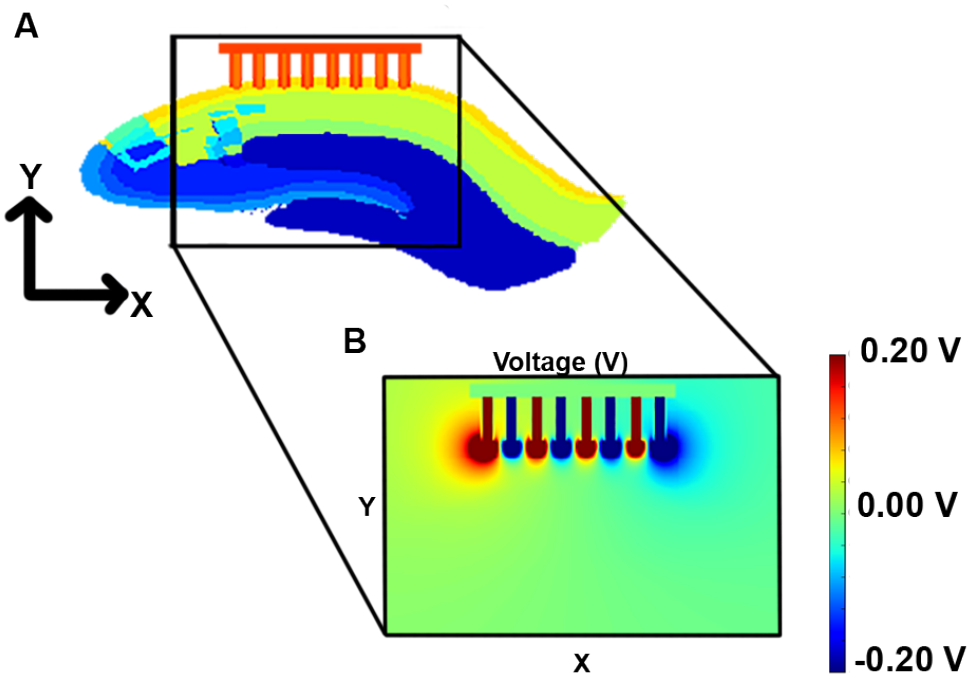

Figure 6.5. Admittance Method model. (a) Slice of the hippocampus model, showing the electrode geometry and placement with the surface exposed to the cell bodies in the CA1 section, and (b) a 2D slice of the voltage resulting from an Admittance Method simulation of current injection to bipolar pairs of electrodes in this model at a single timestep.

at a single timestep along the mediolateral plane through the center of the electrodes. This slice was chosen to show the maximum voltage levels and relationship between the electrodes. The voltage was high directly beneath the electrode surface, with a high electric field between each bipolar pair as was expected, and a focused strength that faded quickly in the surrounding material. The voltage was higher at the outside electrodes compared to those in the middle because of the lack of an oppositely polarized electrodes on both sides. The resulting maximum voltage of about 1V was as expected, based on results of experimental studies with rat hippocampus and similar electrode geometry and placement.

6.4.2 Stimulation Threshold vs. Depth

The stimulation threshold was computed for four depths into the CA1 section of the hippocampus, finding the lowest threshold to be at the surface of the hippocampal tissue.

The current magnitude required to stimulate this single CA1 pyramidal cell with a single biphasic 1-ms wide pulse increased with increased penetration into the hippocampus. The resulting magnitude ranges from about 8 μA to 87 μA, with the results shown in Figure 6.6. This is an encouraging result, as it is desired for this implanted device to be as minimally invasive as possible, and these results indicate that the lowest current threshold exists for the case in which the electrodes do not penetrate the hippocampus. This result makes sense intuitively. Inserting the electrodes further from the cell bodies pushes the electrode surface further from the cell bodies, making the location of initial stimulation being in the dendritic region, in which the size of the neural segments are much smaller than at the cell body, therefore being more difficult to stimulate. This also affects the stimulation timing, leading to a delay for the cell body to be stimulated due to the propagation delay and inability to directly stimulate the cell body, as shown in Figure 6.7.

6.4.3 Dentate Gyrus Electrode Placement

Simulations applying electrodes in the nine different locations in the dentate gyrus as shown in Figure 6.4, at various magnitudes ranging from 50 to 650 μA were run to estimate the electrode placement leading to the most efficient stimulation, providing the highest

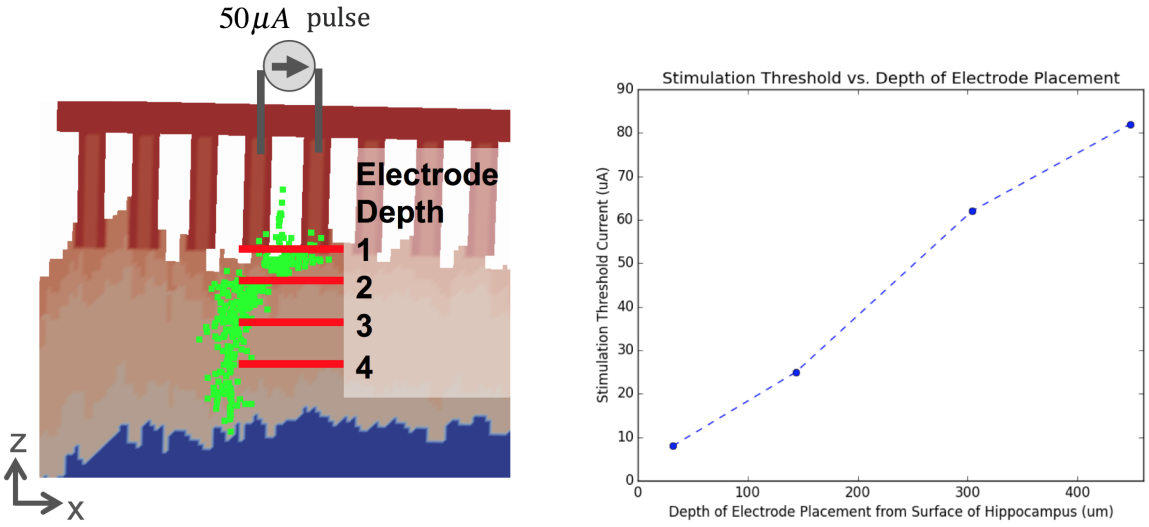

Figure 6.6. (Left) A slice of the 3D hippocampus model for the first electrode placement, with annotations defining the current source and subsequent electrode depths. The location of each compartment of the CA1 cell NEURON model is shown in green. (Right) Resulting current stimulation thresholds for the four different electrode placements.

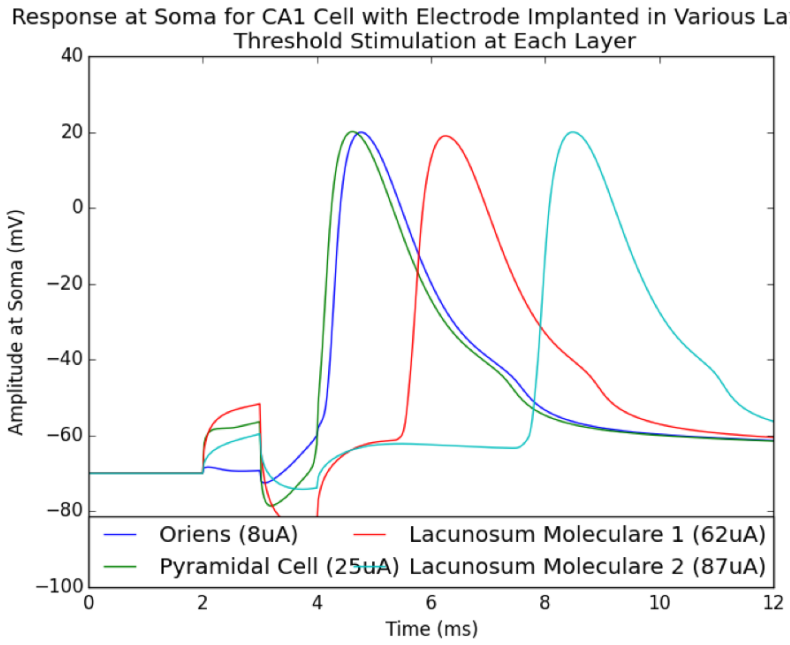

Figure 6.7. Membrane potential at the soma of the CA1 pyramidal cell when the threshold stimulation is applied to each of the four considered electrode placements, illustrating the latency of the response at the cell body in addition to change in stimulation thresholds.

quantity of stimulated cells for a given magnitude. This not only provided information on the number of cells stimulated near the electrode surface, but how the stimulation propagated along the dentate gyrus and proceeded to stimulate cells downstream via activation of perforant path axons, providing a nonlinear response of number of cells activated vs. magnitude of the current stimulus. An example of the spatio-temporal response to electrical stimulation at location 7 (as noted in Figure 6.4) is given in Figure 6.8, showing cells activating near the electrodes immediately after stimulation, which propagates around the dentate gyrus, leading to induced neural activity throughout the dentate gyrus within about 12 ms. The most amount of neural activity was found when stimulating near the crest of the dentate gyrus. When stimulating near the cell bodies with 100 μA, about 5.5% of the total cells in the large-scale model were stimulated, all of which were in close proximity to the electrodes. After about 12 ms, cells downstream in the hippocampus were activated, leading to activity in about 1% of the total cells. When shifting the electrodes closer to the edge of the dentate gyrus near the perforant path axons, and applying the same stimulus, about 5.5% of the cells in the model were stimulated. These results are shown in Figure 6.9.

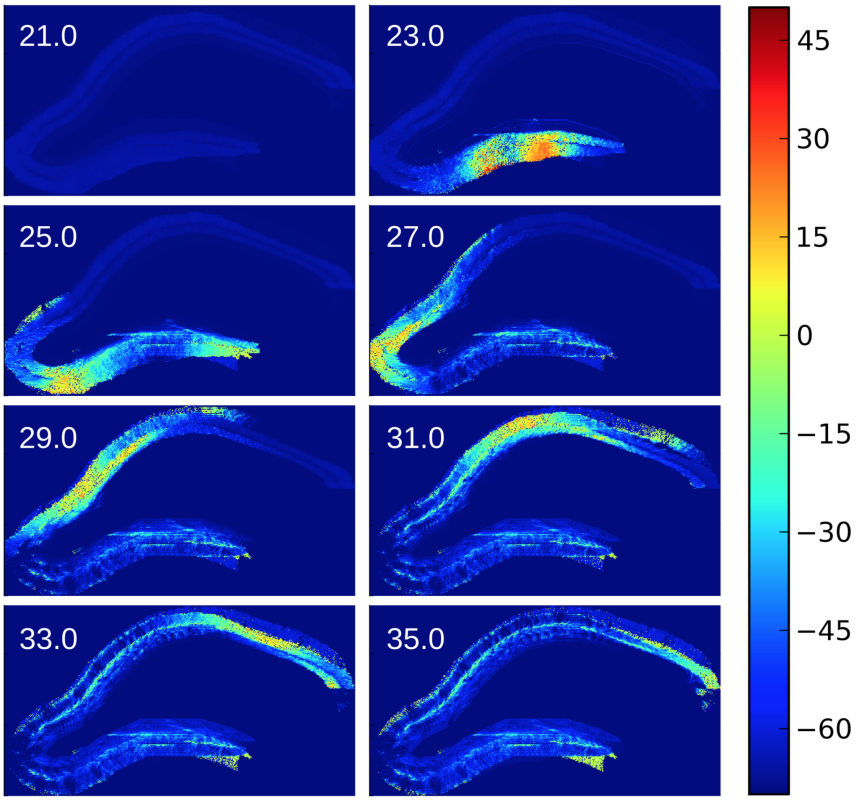

Figure 6.8. Simulated membrane potential in large-scale model of dentate gyrus over time resulting from perforant path stimulation via extracellular electrodes.

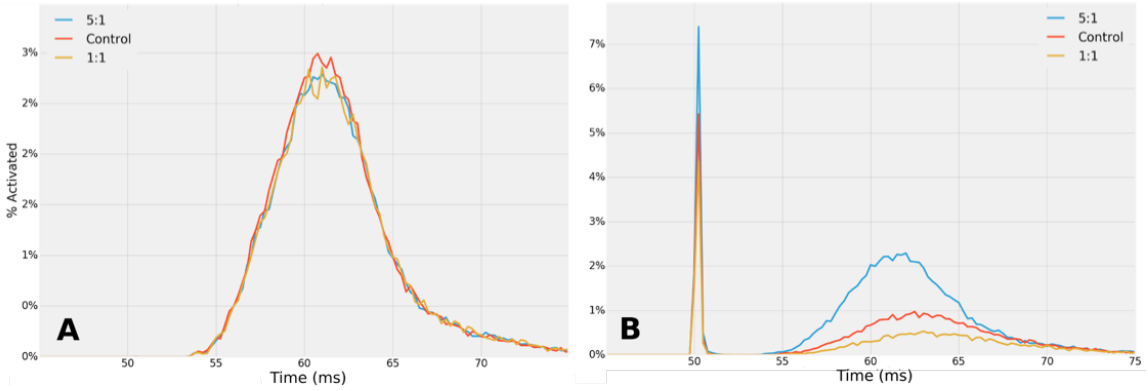

Figure 6.9. Resulting percent of total cells activated in the large-scale dentate gyrus neural network model due to a biphasic 1-ms wide 100 μA current stimulus applied to the crest of the dentate gyrus near (a) perforant path and (b) cell bodies. This is shown for three variations of the discretized bulk-tissue model, in which the entire hippocampus is described as a homogeneous medium (yellow), with resistivity discretization based on CA1 measurements in literature (Control, red), and with increased heterogeneity with a ratio in resistivity of 5:1 from the cell body to molecular regions (blue).

6.4.4 Heterogeneous Resistivity

The intrinsic heterogeneity of neural tissue naturally gives rise to heterogeneous resistivity; results from a resistivity ratio sensitivity analysis, presented in this study, demonstrate the large impact that changes of this property can have on the network level activity of a tissue system. As the relative resistivity of the cell body layer was raised, the conductive barrier became more apparent. A 5:1 resistivity ratio from the cell body layer to the molecular regions shows that a homogeneous resistivity profile would give inaccurate predictions of hilar and cell body layer electrical potentials which could result in shorting of the neural circuit if the potentials caused GC axons, mossy fibers, or other hilar cells to become directly activated by stimulating events. Indeed, the importance of resistive heterogeneity is amplified when stimulating near the cell body layer, where potentials are already larger due to proximity. Though the results are intuitive, it is important that our implementation of heterogeneous resistivity follows this intuition. The process undergone in this study illuminated the role the DG cell body layer could play in shielding hilar structures and how dynamic changes in resistivity could make this region more or less vulnerable to stimulating current penetration. Figure 6.9 gives an example of how the number of activated cells varied when changing the bulk-tissue discretization from homogeneous to having a 5:1 resistivity ratio between the cell bodies and molecular regions.

6.5 Conclusion

In this chapter, a multiscale model of hippocampus electrical stimulation was designed and constructed for the use as a predictive tool for increasing the effectivity of memory prosthetic devices. Utility of the model was presented through a computational study of predicted current stimulation threshold for prosthetic electrical stimulation of rat hippocampus, following an experimental study in literature in which such a device was shown to provide partial memory restoration. This provided recommendation of electrode depth and baseline stimulus parameters for future experiments. The modeling strategy was then expanded to incorporate a large-scale model of the dentate gyrus and used to study the spatio-temporal dynamics of induced neural activity for varying stimulation parameters. Results included predictions of the most efficient placement in the dentate gyrus, inducing the highest neural activity for a given stimulus.

CHAPTER 7

CLOSED-LOOP STRATEGY FOR SIMULATION OF ELECTRICAL STIMULATION OF NEURAL TISSUE

7.1 Introduction

Electrical stimulation used to evoke neural response has been studied extensively in computational modeling. In recent years, as computational ability increases, it has become common to couple modeling strategies into multiphysics approaches. This involves numerical techniques in electromagnetics, such as finite-difference-time-domain (FDTD), finite element method (FEM), or impedance or admittance method (IM or AM) for modeling electric or magnetic field induced in tissue by stimulating electrodes or magnetic coils. At a finer spatio-temporal scale, compartmentalized models of neurons, along with differential equation solvers are used to model neural activity for regions of neural tissue of interest, using tools such as NEURON [5] By coupling these two different computational techniques into a single simulation platform, the neural response to heterogeneous extracellular electric field based on the stimulation parameters and heterogeneous tissue can be approximated. Tools using this approach have been proposed for use as predictive tools for further innovating attempts at systematic neural stimulation, in both research for progressing models of cells and cellular networks, as well as rehabilitative techniques for treating neural disorders. An example is the case of a hippocampus prosthetic that is currently under development for enhancing or restoring memory for subjects with memory disorders such as Alzheimer's disease or dimentia. In this device, neural recordings in the hippocampus is used to predict the accuracy of memory creation. When a "weak" memory recollection is detected, stimulating electrodes are used to induce neural activity appropriately, following a multiinput multioutput (MIMO) model. Encouraging results have been presented in nonhuman primate and mice experiments. [11, 12] However, to

improve implementation towards clinical trials and identify the most advantageous electrode geometry and placement and stimulation waveform, computational techniques as mentioned in this section, are utilized here.

One commonality amongst such attempts at coupled multiphysics multiscale methodologies is an open-loop simulation setup. Typically the electric field in bulk-tissue is first computed using FEM or AM. This is then applied as the extracellular electric field to a model of a neuron or neural network to approximate the neural tissue's response to the stimulation. It is assumed that the extracellular electric field is solely due to the stimulating electronics, or that any changes to the extracellular space due to neural activity is negligible. However, this is not necessarily the case. There is constant electrical activity in neural tissue, all contributing to changes to the extracellular electric field, providing feedback to the cells themselves, as well as influencing their neighbors. In neural tissue with high cellular density like the hippocampus [13], such behavior is even more likely. Coupling between adjacent neurons due to their influence on the extracellular electric field has been observed experimentally, described with the term ephaptic coupling. An ephapse describes the coupling of adjacent cellular segments through electric field interactions, rather than a direct connection through synapse(s) or gap junction(s.) In neural tissue in the hippocampus, ephaptic coupling has been shown to play a role in population firing dynamics and have the ability to modulate spiking phase [90, 91]. However, the mechanisms by which ephaptic activity modulates neural activity and what role it plays is still not well understood. This is likely due to the difficulty of studying these phenomena experimentally. In in vivo experiments, an extracellular electric field is omnipresent, as there is always electrical activity in functioning neural tissue. In order to separate ephaptic activity from other neural processes, one would have to be able to monitor local field potentials as well as cellular membrane potential, while also inducing extracellular activity and minimizing the effects the recording probes and any stimulation circuitry may have on the measurements and induced activity [91]. This makes the use of computational modeling an attractive approach for further understanding such activity in the brain [92]. This can allow for the functionality of ephaptic coupling to be studied, in addition to investigating effects it has on attempts to electrically stimulate neural tissue for rehabilitative or therapeutic devices.

In this chapter, a strategy is proposed for closing the loop in computational modeling approaches coupling extracellular electric field and neural network models. In this simulation strategy the extracellular electric field is computed dynamically, taking into account the effects of neural electrical activity. This toolset is then used to study the change in results of electrical stimulation threshold predictions in a test simulation. Results from this test simulation include the ability of population spiking to induce a spike in an adjacent cell under subthreshold circumstances.

7.2 Initial Validation

Before taking on the task of modifying the computational tools to create the handshake between simulation platforms, as discussed in the introduction, a set of simulations were run to verify that nearby cells can in fact alter a given cell's membrane voltage and response to electrical stimulation. To do this, the model of hippocampus from the previous chapter was utilized. The CA1 pyramidal cell considered in that study was duplicated, creating a set of two cells. The second cell was translated to be directly adjacent to the first, remaining parallel with array of microwire electrodes. An Admittance Method (AM) simulation was run, as was done in the study in Chapter 6, considering a biphasic current stimulus applied to a bipolar pair of electrodes closest to the CA1 cell. The resulting node voltages were interpolated, providing an extracellular voltage to be applied to each compartment of the CA1 cell. These were applied as extracellular voltage sources in NEURON software. A NEURON simulation was then run, modeling the membrane potential in the CA1 cell that resulted from the extracellular stimulation.

In order to show the ability of a cell to affect its neighboring cell's excitability, the resulting membrane current from each compartment of the CA1 cell was exported in NEURON software. These current values were applied as current sources in a subsequent Admittance Method simulation, providing new voltage results in the bulk-tissue surrounding the CA1 cells due to neuron's electrical activity. The results were again interpolated, this time to provide extracellular voltage at the location of the adjacent CA1 cell. Using superposition, the voltage resulting from both simulations (current injection through a pair of electrodes and current injection from a neighboring CA1 cell) were summed and applied as extracellular sources. Finally, a subsequent NEURON simulation was run to

model the membrane potential of this second CA1 cell. The input current was scaled in order to find the stimulation threshold with and without the inclusion of the second AM simulation. A diagram outlining this approach is given in Figure 7.1. While not the most precise representation of how an adjacent cell can affect a cell's excitability, due to the coarse spatial resolution of the Admittance Method model of 16μm and the timestep of the simulation of 1ms being much wider than the changes in membrane current, this study provided a rough approximation. The results showed a 5.6% change in stimulation threshold, concluding the parameter to have a sufficient contribution to be included in our modeling efforts. Therefore, a new simulation platform was developed, linking the AM and NEURON, dynamically updating the current sources in the AM simulation and the extracellular voltage sources in NEURON. The next sections will discuss the details of this implementation.

7.3 Methods

7.3.1 Modeling Strategy

To allow for dynamically updated current sources due to neural electrical activity and/or electrical stimulation, modifications were required in the steps taken in the AM and NEURON solver. In this strategy, a timestep at which a "handshake" between the two

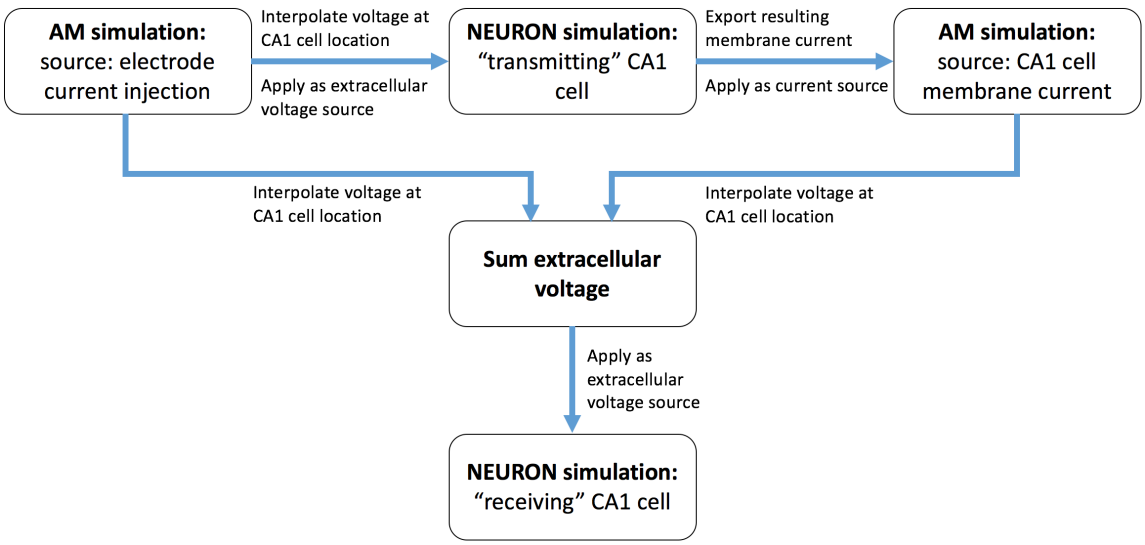

Figure 7.1. Diagram of the modeling strategy that includes cellular activity in the computation of extracellular electric field using superposition principle.

simulation tools is defined. The AM is initialized and runs the first timestep, after which the extracellular voltage at each node in the AM model is interpolated at the location of each compartment of the NEURON model and saved to file. The simulation then pauses. The NEURON simulation is initialized, these voltages are applied as extracellular sources, and NEURON runs for the length of the predefined timestep. The simulation then pauses, and exports the membrane current at each compartment. These current values are input to the AM as new sources and another timestep is run. This process is continued until the entire length of the simulation finishes. The remainder of this section discusses the modifications to the software that were necessary to execute this strategy.

7.3.2 Custom Admittance Method Implementation

The variant of the Admittance Method used is as discussed in [17, 66, 93]. This is a time-stepping quasi-static implementation. The setup is as shown in gray in the diagram in Figure 7.2. First, a discretized model must be built and meshed. The mesh is then discretized by tissue dielectric properties, considering each edge in the model as a lumped circuit of resistors and/or capacitors. Using this data, a circuital network is then defined. A set of linear equations is then constructed, of the form $G * V = I$, where G=conductance, I=input current, and V=voltage to be solved for. First, the I vector is initialized. For n

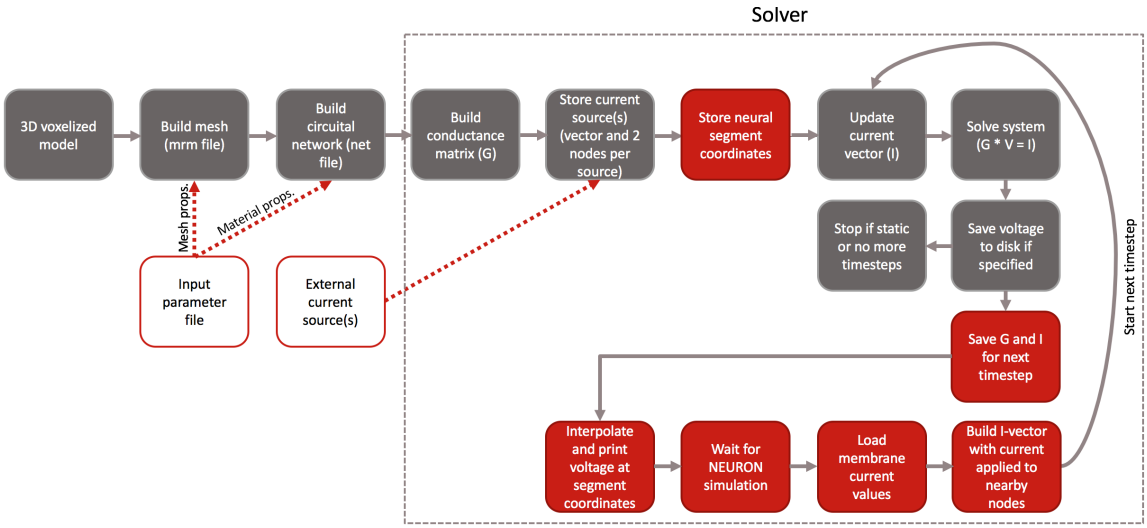

Figure 7.2. Diagram describing the steps taken in an Admittance Method simulation, with additional steps for including dynamically updated current sources due to neural activity highlighted in red.

nodes in the model, I has a length of n, with each value representing the current source applied to that node. G is a matrix, with dimensions of nxn. This is formed by the resistances in the circuital network. For a pair of nodes (a, b) in G, if $a = b$, then for M resistances, G_{ab} is as follows:

$$G_{ab} = \sum_{i=1}^{M} \frac{1}{R_i} \tag{7.1}$$

For $a \neq b$ and having M resistors between the two nodes, G_{ab} is:

$$G_{ab} = G_{ba} = \sum_{i=1}^{M} \frac{-1}{R_i} \tag{7.2}$$

The vector V containing the voltage at each node in the model can then be computed by solving the system of linear equations. This was accomplished with the biconjugate gradient method with a residue of 1E-08 as the stop criteria. At the end of each timestep, the energy in the system is stored in capacitors at each edge in the model. These are implemented as an equivalent conductance and current source, and are added to the G and I matrix and vector, respectively, at the beginning of the subsequent timestep. So, the resulting voltage from each timestep serves as an initial condition for the subsequent timestep, and the system is solved again. Further details are provided in [17].

In this work, this workflow was modified appropriately to update the current injected into the system to include neuronal activity, as shown in red in the diagram in Figure 7.2. With this setup, at the beginning of the simulation, the coordinates of the center of each neuronal compartment are stored into memory. A function was written to find the eight nodes surrounding each set of coordinates, in which the current magnitude is divided and applied to all eight. The magnitude at each node depends on the distance the coordinate is from that node, normalized to the total distance the compartment center is from all eight nodes. These current magnitudes are applied to the current vector, summing with the current values that are implemented as a result of current injection and/or the result from the previous timestep. The simulation is then run for the next timestep and pauses to wait for input from the NEURON simulation.

7.3.3 Model Construction

To test this new coupled AM-NEURON implementation, a simple model was constructed. The AM model was defined to have homogeneous tissue and a pair of electrodes,

as shown in Figure 7.3. The resolution of the model is 1 μm and the total size of the model is 20x30x100 μm. The electrodes were defined to have a diameter of 10 μm with a pitch of 60 μm. The space surrounding the electrodes was given a resistivity of 3.2 Ω-m, following the measurements of bulk resistivity of hippocampus from Chapter 6.

A NEURON model containing a bundle of 7 axons was defined parallel to the electrode surface, at a location centered 10 μm away from the electrodes. The axons were given a length of 50 μm and a diameter of 5 μm. The default Hodgkin-Huxley mechanism in NEURON was applied to each axon, giving the ability to spike.

7.3.4 Simulation Thresholds

Simulations were run using this test model under subthreshold conditions, applying a 1-ms biphasic pulse as was studied in Chapter 6 in the hippocampus, finding the dif-

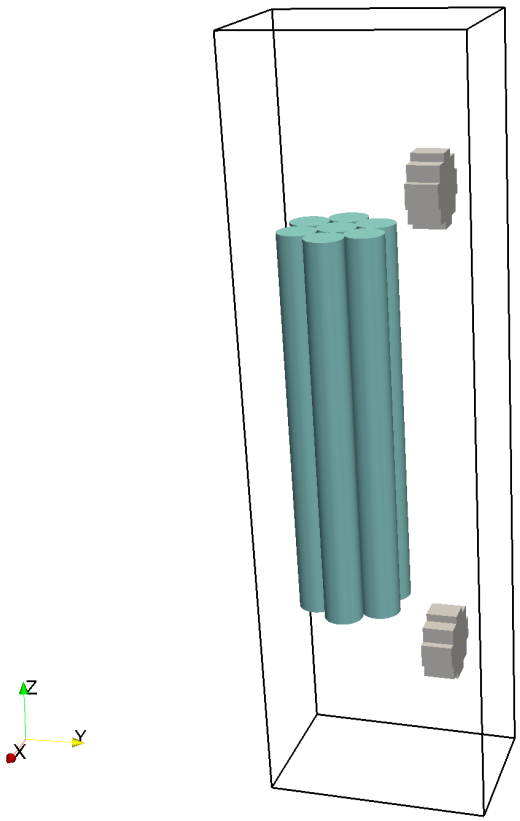

Figure 7.3. Rendering of the model used for testing the bidirectional AM-NEURON simulation setup, including the AM model space with electrodes shown in gray. A rendering of the NEURON model of seven axons is included in blue, showing the proximity to the stimulating electrodes.

ference in resulting membrane potential due to electrical activity in neighboring cells and comparing with values in literature. Then, spiking was induced in some of the cells to test the ability of nearby active cells to cause a cell to spike, with and without the application of subthreshold electrical stimulation. This was accomplished by adding current clamps to six of the cells, with a magnitude of 1 nA, duration of 1 ms, and set to occur at the same time as the extracellular current source applied to the electrodes. A timestep for the handshake between the two methodologies of 1 ms (matching the timestep of AM without this bidirectional communication) and 0.025 μs (matching the timestep of the NEURON simulation) were attempted.

7.4 Results

Resulting plots of the extracellular voltage, as computed by the AM, are shown in Figure 7.4. The first plot shows a slice of the voltage through the electrodes when a stimulus is applied to the pair of electrodes. There is a break in the voltage pattern at the location of the neural compartments. This is clearer in the second plot, which shows a slice of the voltage through the electrodes after the pulse has been applied, with the colorbar scaled to better visualize the effects neural activity has on the extracellular voltage.

The membrane voltage of all seven of the cells under subthreshold conditions, in which a 1 ms biphasic current stimulus of 100 nA magnitude was applied across the pair of bipolar electrodes, is given in the top of Figure 7.5. In this figure, the communication between the AM and NEURON was updated every 1 ms. There are clear changes in the membrane potential at every timestep. The changes were less than 1 mV. However, this can be sufficient difference to modulate activity in dense neural tissue [91]. When a spike was induced in all cells except cell 2 (the cell closest to the firing electrodes), and the same stimulus that resulted in the subthreshold response in the first plot in Figure 7.5, an action potential was observed in cell 2. This shows that the input of nearby cells can indeed affect bulk firing in conditions similar to this bundle of axons, as well as alter the predicted stimulation threshold.

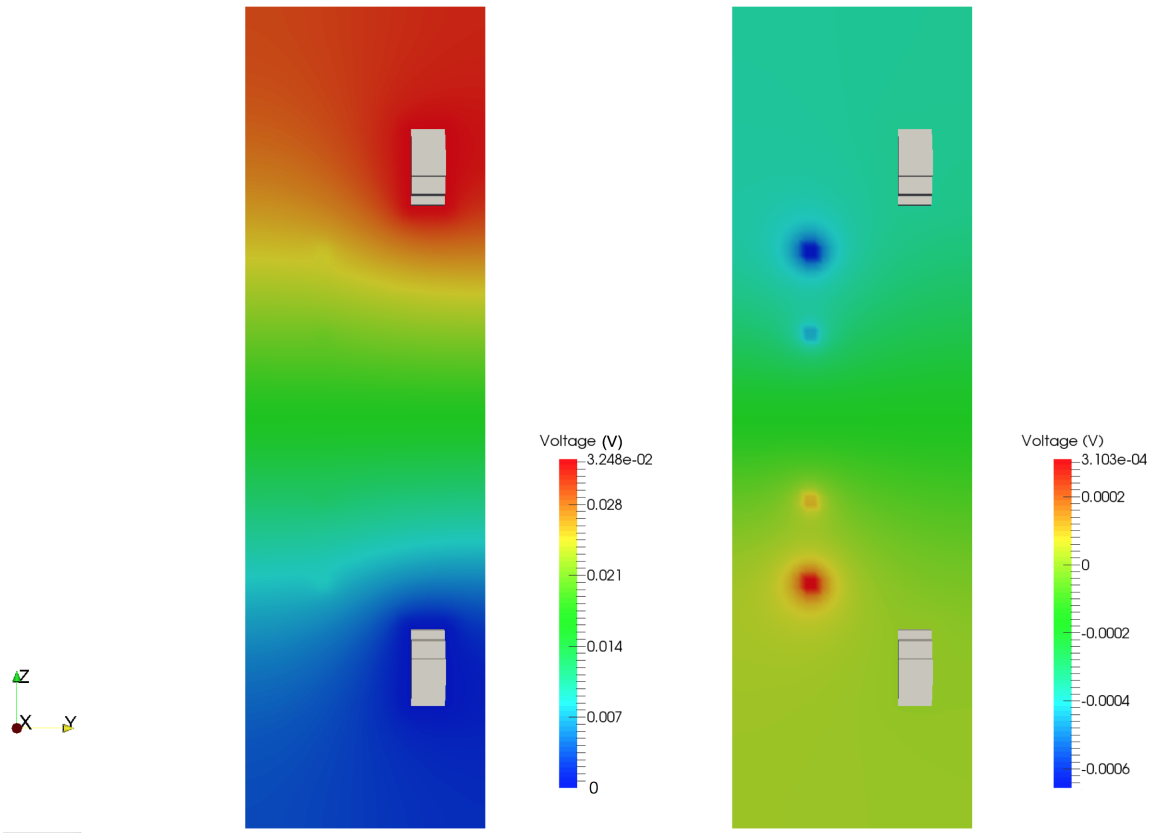

Figure 7.4. 2D slices of the voltage resulting from the AM simulation at two different timetseps: (left) during applied electrical stimulation of 100 nA and (right) 1 ms after the electrical stimulation is applied, showing the change in the extracellular field due to both current injected into electrodes and electrical activity of the neural segments.

7.5 Discussion

7.5.1 Model Limitations

The model presented here is a simplified case meant to provide a proof-of-concept on how the inclusion of ephaptic effects can influence induced spiking via electrical stimulation, and serve as a test for the software implementation of bidirectional communication between the AM and NEURON. The volume of tissue considered in the AM volume conductor model is considered to have homogeneous dielectric properties as well as covering a limited amount of space of neural tissue. In addition, the axons considered are modeled as ideal straight cylinders with the default Hodgkin-Huxley model applied. These are strictly limitations of the presented model for focusing on ephaptic effects and the closed-loop simulation platform, and not limitations of the methodology. This toolset may be

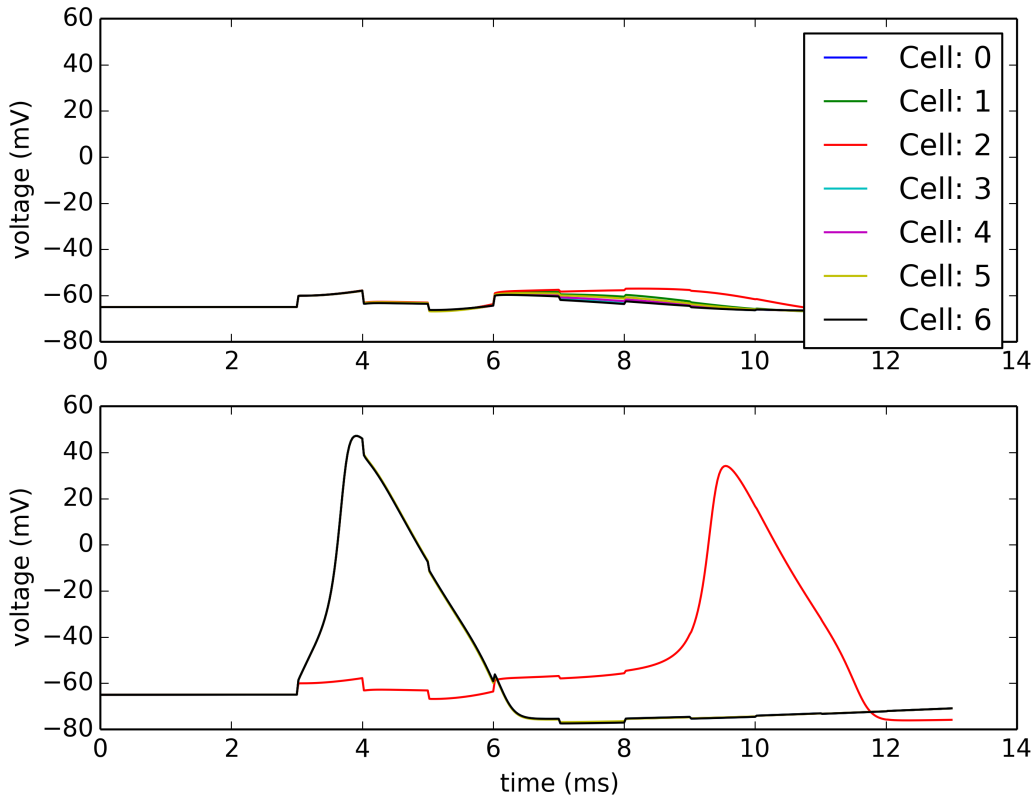

Figure 7.5. Membrane potential at the center of each of the cells in the NEURON model. (Top) During subthreshold electrical stimulation in which a 1 ms biphasic pulse with a magnitude of 100 nA was applied to the pair of electrodes, and (Bottom) when this simulation was repeated with all cells except cell 2 having induced spikes. This shows that under subthreshold conditions, the activity of nearby cells can induce neural activation.

applied to the larger, more complex models presented previously in this dissertation.

Another major implementation of this methodology is the added computational time. In this setup, the AM simulation requires the system to be solved every timestep. By increasing the temporal resolution, the amount of computation time is then increased at a relatively linear rate, with the added time being close to the number of added timesteps. This is not too relevant for the simulation in the test case presented here due to the small size of the simulation domain. However, when applying to larger models as presented earlier in this dissertation, this can heavily impact the computational time. There are factors that can be investigated to reduce the time taken. First, the system is currently storing the voltage resulting from the AM to file after every timestep, and NEURON is saving the membrane current to file after every timestep. This was done in order to

have transparency in the process and be able to view the data resulting from every step of the simulation. Removing the input/output overhead would increase the efficiency of the simulation. In addition, the larger hippocampus NEURON simulations presented in Chapter 6 use a parallelized simulation setup, which further increases the simulation efficiency.

7.5.2 Influences of Neural Network

In synaptically connected neural networks, electric field is developed within the synaptic cleft itself [91]. As described by Koch et al., this can modify the membrane potential of the pre- and postsynaptic cells and modify their ionic flux, further influencing synaptic activity and cellular dynamics. The toolset presented in this paper can be expanded to larger networks to investigate such phenomena of cells influencing their own dynamics, rather than considering purely ephaptic activity.

7.6 Conclusion

In this chapter, a methodology for coupling NEURON with the AM, allowing for bidirectional communication between the two simulation tools was proposed. This allowed for the study of how ephaptic coupling affects the stimulation of neural segments and how it can induce population spiking that is otherwise neglected in traditional EM-NEURON simulation setups. This toolset can provide increased predictability in studies as presented in Chapter 6, in which computational tools are being used to design electrical stimulation setups for inducing population firing. In addition to studying electrical stimulation for artificially inducing firing in cells, this type of modeling approach can be useful in understanding dynamics within dense neural tissue and the functional role of ephaptic coupling.

CHAPTER 8

CONCLUSION

In neuroprosthetic devices that interface with neural tissue and induce activity in attempt to mimic natural functionality, a thorough understanding of the tissue being stimulated is required in order to attempt to restore it in an implanted biomimetic device. Additionally, knowledge of the tissue's response to electrical stimulation is necessary to confidently stimulate the tissue as desired without adverse effects. Computational modeling provides a means to investigate both neural functionality as well as the response to electrical stimulation. In this work, a multiscale simulation strategy for modeling the response of retina and hippocampus tissue to electrical stimulation in neuroprosthetic devices was proposed, aiding in the innovation and understanding of existing devices used to restore partial vision to patients blinded by retinal degenerative diseases and memory functionality to those with memory disorders, respectively. In doing so, this work contributes models that can be used in future studies for further improving prosthetic devices. In the retina, a highly detailed model of retina neural network based on a connectome and electrophysiological and anatomical studies of degenerating retina was constructed, providing the most complete and precise model of degenerated retina to date. Combining this with a model of bulk-tissue and electronics has created a new test bench for testing the next generation of stimulating electrodes. In hippocampus, a similar model that is coupled with the most detailed neural network model of dentate gyrus to date was constructed, allowing for the response of over one million cells to electrical stimulation to be simulated and used to predict the most advantageous stimulation parameters.

In addition to the contribution of models for use with improving future devices, simulation tools themselves were proposed and constructed. A new methodology for computing bulk-tissue resistive properties for cases in which there are no measurements provided in literature, or in which measurements are inaccurate. This provides a means for more

precise computational models of other neural tissues. By linking the Admittance Method with NEURON in a closed-loop fashion, a new methodology for simulating how neurons' electrical activity affect their own dynamics as well as the cells around them was proposed. These tools and modeling approaches can scale beyond the specific retina and hippocampus prosthetic devices discussed in this dissertation, with the aim of helping advance neuroprosthetic electrical stimulation.

REFERENCES

[1] H. Kasi, R. Meissner, A. Babalian, H. Van Lintel, A. Bertsch, and P. Renaud, "Direct localised measurement of electrical resistivity profile in rat and embryonic chick retinas using a microprobe," *J. Electr. Bioimpedance*, vol. 1, no. 1, pp. 84–92, 2011.

[2] C. J. Karwoski, D. Frambach, and L. M. Proenza, "Laminar profile of resistivity in frog retina," *J. Neurophysiol.*, vol. 54, no. 6, pp. 1607–1619, 1985.

[3] H. Choi, L. Zhang, M. S. Cembrowski, C. F. Sabottke, A. L. Markowitz, D. A. Butts, W. L. Kath, J. H. Singer, and H. Riecke, "Intrinsic bursting of AII amacrine cells underlies oscillations in the rd1 mouse retina." *J. Neurophysiol.*, vol. 112, no. 6, pp. 1491–504, 2014.

[4] F. Rattay, "Analysis of models for external stimulation of axons," *IEEE Trans. Biomed. Eng.*, no. 10, pp. 974–977, 1986.

[5] N. T. Carnevale and M. L. Hines, *The NEURON Book*. Cambridge, U.K.: Cambridge Univ. Press, 2006.

[6] A. K. Ahuja, J. Yeoh, J. D. Dorn, A. Caspi, V. Wuyyuru, M. J. McMahon, M. S. Humayun, R. J. Greenberg, and L. Dacruz, "Factors affecting perceptual threshold in argus ii retinal prosthesis subjects," *Transl. Vis. Sci. Technol.*, vol. 2, no. 4, p. 1, 2013.

[7] K. Loizos, G. Lazzi, R. Marc, and C. Cela, "Virtual electrode design for increasing spatial resolution in retinal prosthesis," *IET Healthcare Tech. Lett.*, vol. 3, no. 2, pp. 93–97, 2016.

[8] M. R. Behrend, A. K. Ahuja, M. S. Humayun, R. H. Chow, and J. D. Weiland, "Resolution of the epiretinal prosthesis is not limited by electrode size," *IEEE Trans. Neural Syst. Rehabil. Eng.*, vol. 19, no. 4, pp. 436–442, 2011.

[9] S. Nirenberg and C. Pandarinath, "Retinal prosthetic strategy with the capacity to restore normal vision." *Proc. Natl. Acad. Sci.*, vol. 109, no. 37, pp. 15 012–7, 2012.

[10] S. I. Fried, H. A. Hsueh, and F. S. Werblin, "A method for generating precise temporal patterns of retinal spiking using prosthetic stimulation," *J. Neurophysiol.*, vol. 95, no. 2, pp. 970–978, 2006.

[11] T. W. Berger, R. E. Hampson, D. Song, A. Goonawardena, V. Z. Marmarelis, and S. A. Deadwyler, "A cortical neural prosthesis for restoring and enhancing memory," *J. Neural Eng.*, vol. 8, no. 4, June 2011.

[12] R. E. Hampson, D. Song, I. Opris, L. M. Santos, D. C. Shin, G. A. Gerhardt, V. Z. Marmarelis, T. W. Berger, and S. A. Deadwyler, "Facilitation of memory encoding in primate hippocampus by a neuroprosthesis that promotes task-specific neural firing," *J. Neural Eng.*, vol. 10, no. 6, p. 066013, 2013.

[13] P. J. Hendrickson, G. Yu, D. Song, and T. W. Berger, "A million-plus neuron model of the hippocampal dentate gyrus: critical role for topography in determining spatiotemporal network dynamics," *IEEE Trans. Biomed. Eng.*, vol. 63, no. 1, pp. 199–209, 2016.

[14] J. D. Weiland and M. S. Humayun, "Retinal Prosthesis," *Annu. Rev. Biomed. Eng.*, vol. 61, no. 5, pp. 1412–24, 2014.

[15] M. Mahadevappa, J. D. Weiland, D. Yanai, I. Fine, R. J. Greenberg, and M. S. Humayun, "Perceptual thresholds and electrode impedance in three retinal prosthesis subjects," *IEEE Trans. Neural Syst. Rehabil. Eng.*, vol. 13, no. 2, pp. 201–206, 2005.

[16] E. R. Kandel, J. H. Schwartz, T. M. Jessell, S. A. Siegelbaum, and A. Hudspeth, *Principles of Neural Science*. New York: McGraw-Hill, 2000, vol. 4.

[17] C. J. Cela, R. C. Lee, and G. Lazzi, "Modeling cellular lysis in skeletal muscle due to electric shock," *IEEE Trans. Biomed. Eng.*, vol. 58, no. 5, pp. 1286–1293, 2011.

[18] J. Anderson, S. Mohammed, B. Grimm, B. Jones, P. Koshevoy, T. Tasdizen, R. Whitaker, and R. Marc, "The viking viewer for connectomics: scalable multi-user annotation and summarization of large volume data sets," *J. Microsc.*, vol. 241, no. 1, pp. 13–28, 2011.

[19] V. M. Spitzer and D. G. Whitlock, "The visible human dataset: the anatomical platform for human simulation," *Anat. Rec.*, vol. 253, no. 2, pp. 49–57, 1998.

[20] A. K. Ahuja and M. R. Behrend, "The Argus II retinal prosthesis: Factors affecting patient selection for implantation," *Prog. Retin. Eye Res.*, vol. 36, pp. 1–23, 2013.

[21] R. E. Marc, B. W. Jones, C. B. Watt, J. R. Anderson, C. Sigulinsky, and S. Lauritzen, "Retinal connectomics: Towards complete, accurate networks," *Prog. Retin. Eye Res.*, vol. 37, pp. 141–162, 2013.

[22] J. R. Anderson, B. W. Jones, C. B. Watt, M. V. Shaw, J.-H. Yang, D. DeMill, J. S. Lauritzen, Y. Lin, K. D. Rapp, D. Mastronarde *et al.*, "Exploring the retinal connectome," *Mol. Vis.*, vol. 17, pp. 355–379, 2011.

[23] D. K. Freeman, J. S. Jeng, S. K. Kelly, E. Hartveit, and S. I. Fried, "Calcium channel dynamics limit synaptic release in response to prosthetic stimulation with sinusoidal waveforms." *J. Neural Eng.*, vol. 8, no. 4, 2011.

[24] J.-M. Bouteiller, S. Allam, E. Hu, R. Greget, N. Ambert, A. Keller, S. Bischoff, M. Baudry, and T. Berger, "Integrated multiscale modeling of the nervous system: Predicting changes in hippocampal network activity by a positive ampa receptor modulator," *IEEE Trans. Biomed. Eng.*, vol. 58, no. 10, pp. 3008–3011, Oct 2011.

[25] R. E. Marc, B. W. Jones, C. B. Watt, and E. Strettoi, "Neural remodeling in retinal degeneration," *Prog. Retin. Eye Res.*, vol. 22, no. 5, pp. 607–655, 2003.

[26] R. J. Greenberg, T. J. Velte, M. S. Humayun, G. N. Scarlatis, and E. de Juan Jr, "A computational model of electrical stimulation of the retinal ganglion cell," *IEEE Trans. Biomed. Eng.*, vol. 46, no. 5, pp. 505–514, 1999.

[27] S. Usui, A. Ishihara, Y. Kamiyama, and H. Ishii, "Ionic current model of bipolar cells in the lower vertebrate retina," *Vis. Res.*, vol. 36, no. 24, pp. 4069–4076, 1996.

[28] T. Kameneva, H. Meffin, and A. N. Burkitt, "Modelling intrinsic electrophysiological properties of ON and OFF retinal ganglion cells," *J. Comput. Neurosci.*, vol. 31, no. 3, pp. 547–561, 2011.

[29] M. A. Schiefer and W. M. Grill, "Sites of neuronal excitation by epiretinal electrical stimulation," *IEEE Trans. Neural Syst. Rehabil. Eng.*, vol. 14, no. 1, pp. 5–13, 2006.

[30] J. F. Fohlmeister, E. D. Cohen, and E. A. Newman, "Mechanisms and distribution of ion channels in retinal ganglion cells: using temperature as an independent variable," *J. Neurophysiol.*, vol. 103, no. 3, pp. 1357–1374, 2010.

[31] R. Publio, R. F. Oliveira, and A. C. Roque, "A computational study on the role of gap junctions and rod ih conductance in the enhancement of the dynamic range of the retina," *PLoS One*, vol. 4, no. 9, pp. 1–7, 2009.

[32] R. Publio, C. C. Ceballos, and A. C. Roque, "Dynamic range of vertebrate retina ganglion cells: Importance of active dendrites and coupling by electrical synapses," *PLoS One*, vol. 7, no. 10, pp. 1–9, 2012.

[33] L. Wang, S. Liu, and S. Ou, "Numerical simulation of neuronal spike patterns in a retinal network model," *Neural Regen. Res.*, vol. 6, no. 16, 2011.

[34] G. K. Moghaddam, N. H. Lovell, R. G. Wilke, G. J. Suaning, and S. Dokos, "Performance optimization of current focusing and virtual electrode strategies in retinal implants," *Comput. Methods Programs Biomed.*, vol. 117, no. 2, pp. 334–342, 2014.

[35] F. Rattay and S. Resatz, "Effective electrode configuration for selective stimulation with inner eye prostheses," *IEEE Trans. Biomed. Eng.*, vol. 51, no. 9, pp. 1659–1664, 2004.

[36] J. Xie, G.-J. Wang, L. Yow, C. J. Cela, M. Humayun, J. Weiland, G. Lazzi, and H. Jadvar, "Modeling and percept of transcorneal electrical stimulation in humans," *IEEE Trans. Biomed. Eng.*, vol. 58, no. 7, pp. 1932–1939, 2011.

[37] H. Meffin, B. Tahayori, E. N. Sergeev, I. M. Mareels, D. B. Grayden, and A. N. Burkitt, "Modelling extracellular electrical stimulation: III. derivation and interpretation of neural tissue equations," *J. Neural Eng.*, vol. 11, no. 6, pp. 1–22, 2014.

[38] B. Tahayori, H. Meffin, E. N. Sergeev, I. M. Mareels, A. N. Burkitt, and D. B. Grayden, "Modelling extracellular electrical stimulation: IV. effect of the cellular composition of neural tissue on its spatio-temporal filtering properties," *J. Neural Eng.*, vol. 11, no. 6, pp. 1–21, 2014.

[39] D. Tsai, S. Chen, D. A. Protti, J. W. Morley, G. J. Suaning, and N. H. Lovell, "Responses of retinal ganglion cells to extracellular electrical stimulation, from single cell to population: Model-based analysis," *PLoS One*, vol. 7, no. 12, 2012.

[40] M. Abramian, N. H. Lovell, J. W. Morley, G. J. Suaning, and S. Dokos, "Activation and inhibition of retinal ganglion cells in response to epiretinal electrical stimulation: a computational modelling study." *J. Neural Eng.*, vol. 12, no. 1, pp. 1–17, 2015.

[41] K. Loizos, G. Lazzi, J. S. Lauritzen, J. Anderson, B. W. Jones, and R. Marc, "A multiscale computational model for the study of retinal prosthetic stimulation," in *Proc. IEEE 36th Eng. Med. Biol. Soc. Conf.*, 2014, pp. 6100–6103.

[42] D. Stroud, "The effective medium approximations: Some recent developments," *Superlattices Microstruct.*, vol. 23, no. 3, pp. 567–573, 1998.

[43] B. Wang and J. D. Weiland, "Resistivity profiles of wild-type, rd1, and rd10 mouse retina," *Proc. IEEE 37th Eng. Med. Biol. Soc. Conf.*, 2015.

[44] C. J. Cela, "A multiresolution admittance method for large-scale bioelectromagnetic interactions," Ph.D. Dissertation, North Carolina State Univ., Raleigh, NC, 2010.

[45] D. D. Zhou, J. D. Dorn, and R. J. Greenberg, "Argus® II retinal prosthesis system: An overview," in *IEEE Conf. Multimedia Expo*, P. I. 36th Eng. Med. Biol. Soc. Conf., Ed. IEEE, 2013, pp. 1–6.

[46] S. G. Parker and C. R. Johnson, "Scirun: a scientific programming environment for computational steering," in *Proc. ACM/IEEE Conf. Supercomput.*, 1995, p. 52.

[47] C. de Balthasar, S. Patel, A. Roy, R. Freda, S. Greenwald, A. Horsager, M. Mahadevappa, D. Yanai, M. J. McMahon, M. S. Humayun *et al.*, "Factors affecting perceptual thresholds in epiretinal prostheses," *Invest. Ophthalmol. Vis. Sci.*, vol. 49, no. 6, pp. 2303–2314, 2008.

[48] P. Hendrickson, G. Yu, D. Song, and T. Berger, "Interactions between inhibitory interneurons and excitatory associational circuitry in determining spatio-temporal dynamics of hippocampal dentate granule cells: A large-scale computational study," *Front. Syst. Neurosci.*, vol. 9, pp. 1–22, 2015.

[49] A. C. Ho, M. S. Humayun, J. D. Dorn, L. Da Cruz, G. Dagnelie, J. Handa, P. O. Barale, J. A. Sahel, P. E. Stanga, F. Hafezi, A. B. Safran, J. Salzmann, A. Santos, D. Birch, R. Spencer, A. V. Cideciyan, E. De Juan, J. L. Duncan, D. Eliott, A. Fawzi, L. C. Olmos De Koo, G. C. Brown, J. A. Haller, C. D. Regillo, L. V. Del Priore, A. Arditi, D. R. Geruschat, and R. J. Greenberg, "Long-term results from an epiretinal prosthesis to restore sight to the blind," *Ophthalmol.*, vol. 122, no. 8, pp. 1547–1554, 2015.

[50] A. C. Weitz, M. R. Behrend, A. K. Ahuja, P. Christopher, J. Wei, V. Wuyyuru, U. Patel, R. J. Greenberg, M. S. Humayun, R. H. Chow, and J. D. Weiland, "Interphase gap as a means to reduce electrical stimulation thresholds for epiretinal prostheses," *J. Neural Eng.*, vol. 11, pp. 1–9, 2014.

[51] A. E. Hadjinicolaou, C. O. Savage, N. V. Apollo, D. J. Garrett, S. L. Cloherty, M. R. Ibbotson, and B. J. O'Brien, "Optimizing the electrical stimulation of retinal ganglion cells," *IEEE Trans. Neural Syst. Rehabil. Eng.*, vol. 23, no. 2, pp. 169–178, 2015.

[52] L. H. Jepson, P. Hottowy, K. Mathieson, D. E. Gunning, W. Dabrowski, A. M. Litke, and E. Chichilnisky, "Spatially patterned electrical stimulation to enhance resolution of retinal prostheses," *J. Neurosci.*, vol. 34, no. 14, pp. 4871–4881, 2014.

[53] D. K. Freeman, D. K. Eddington, J. F. Rizzo III, S. I. Fried, and J. F. Rizzo, "Selective activation of neuronal targets with sinusoidal electric stimulation," *J. Neurophysiol.*, vol. 104, pp. 2778–2791, 2010.

[54] P. Twyford, C. Cai, and S. Fried, "Differential responses to high-frequency electrical stimulation in ON and OFF retinal ganglion cells." *J. Neural Eng.*, vol. 11, no. 2, 2014.

[55] T. Guo, N. H. Lovell, D. Tsai, S. Fried, J. W. Morley, and G. J. Suaning, "Selective activation of ON and OFF retinal ganglion cells to high-frequency electrical stimulation: a computational modeling study," *Proc. IEEE 36th Eng. Med. Biol. Soc. Conf.*, no. 1, pp. 6108–6111, 2014.

[56] L. H. Jepson, P. Hottowy, K. Mathieson, D. E. Gunning, W. Dabrowski, a. M. Litke, and E. J. Chichilnisky, "Focal electrical stimulation of major ganglion cell types in the primate retina for the design of visual prostheses," *J. Neurosci.*, vol. 33, no. 17, pp. 7194–7205, 2013.

[57] H. Kasi, W. Hasenkamp, G. Cosendai, A. Bertsch, and P. Renaud, "Simulation of epiretinal prostheses - evaluation of geometrical factors affecting stimulation thresholds." *J. Neuroeng. Rehabil.*, vol. 8, no. 44, 2011.

[58] J. F. Fohlmeister and R. F. Miller, "Impulse encoding mechanisms of ganglion cells in the tiger salamander retina," *J. Neurophysiol.*, vol. 78, no. 4, pp. 1935–1947, 1997.

[59] R. Barhoum, G. Martínez-Navarrete, S. Corrochano, F. Germain, L. Fernandez-Sanchez, E. J. de la Rosa, P. de la Villa, and N. Cuenca, "Functional and structural modifications during retinal degeneration in the rd10 mouse," *Neurosci.*, vol. 155, no. 3, pp. 698–713, 2008.

[60] B. W. Jones, M. Kondo, H. Terasaki, C. B. Watt, K. Rapp, J. Anderson, Y. Lin, M. V. Shaw, J.-H. Yang, and R. E. Marc, "Retinal remodeling in the tg p347l rabbit, a large-eye model of retinal degeneration," *J. Comp. Neurol.*, vol. 519, no. 14, pp. 2713–33, Oct 2011.

[61] B. W. Jones, C. B. Watt, J. M. Frederick, W. Baehr, C.-K. Chen, E. M. Levine, A. H. Milam, M. M. Lavail, and R. E. Marc, "Retinal remodeling triggered by photoreceptor degenerations," *J. Comp. Neurol.*, vol. 464, no. 1, pp. 1–16, 2003.

[62] B. W. Jones, R. L. Pfeiffer, W. D. Ferrell, C. B. Watt, J. Tucker, and R. E. Marc, "Retinal remodeling and metabolic alterations in human amd," *Front. Cell. Neurosci.*, vol. 10, 2016.

[63] A. H. Toychiev, E. Ivanova, C. W. Yee, and B. T. Sagdullaev, "Block of gap junctions eliminates aberrant activity and restores light responses during retinal degeneration," *J. Neurosci.*, vol. 33, no. 35, pp. 13 972–13 977, 2013.

[64] S. Trenholm and G. B. Awatramani, "Origins of spontaneous activity in the degenerating retina." *Front. Cell. Neurosci.*, vol. 9, no. 277, pp. 1–7, 2015.

[65] J. Borowska, S. Trenholm, and G. B. Awatramani, "An intrinsic neural oscillator in the degenerating mouse retina," *J. Neurosci.*, vol. 31, no. 13, pp. 5000–5012, 2011.

[66] K. Loizos, A. K. RamRakhyani, J. Anderson, R. Marc, and G. Lazzi, "On the computation of a retina resistivity profile for applications in multi-scale modeling of electrical stimulation and absorption," *Phys. Med. Biol.*, vol. 61, no. 12, pp. 4491–4505, 2016.

[67] C. Gabriel, "Compilation of the dielectric properties of body tissues at rf and microwave frequencies." DTIC Document, Tech. Rep., 1996.

[68] H. Cheng, G. Nair, T. a. Walker, M. K. Kim, M. T. Pardue, P. M. Thulé, D. E. Olson, and T. Q. Duong, "Structural and functional MRI reveals multiple retinal layers." *Proc. Natl. Acad. Sci.*, vol. 103, no. 46, pp. 17 525–17 530, 2006.

[69] M. A. Sikora, J. Gottesman, and R. F. Miller, "A computational model of the ribbon synapse," *J. Neurosci. Methods*, vol. 145, no. 1-2, pp. 47–61, 2005.

[70] C. Sekirnjak, C. Hulse, L. H. Jepson, P. Hottowy, A. Sher, W. Dabrowski, A. M. Litke, and E. Chichilnisky, "Loss of responses to visual but not electrical stimulation in ganglion cells of rats with severe photoreceptor degeneration," *J. Neurophysiol.*, vol. 102, no. 6, pp. 3260–3269, 2009.

[71] R. E. Marc, J. R. Anderson, B. W. Jones, C. L. Sigulinsky, and J. S. Lauritzen, "The AII amacrine cell connectome: a dense network hub," *Front. Neural Circuits*, vol. 8, pp. 1–13, 2014.

[72] R. V. Shannon, "A model of safe levels for electrical stimulation," *IEEE Trans. Biomed. Eng.*, vol. 39, no. 4, pp. 424–426, 1992.

[73] D. B. McCreery, W. F. Agnew, T. G. H. Yuen, and L. Bullara, "Charge density and charge per phase as cofactors in neural injury induced by electrical stimulation," *IEEE Trans. Biomed. Eng.*, vol. 37, no. 10, pp. 996–1001, 1990.

[74] H. Hoshi, L. M. Tian, S. C. Massey, and S. L. Mills, "Two distinct types of ON directionally selective ganglion cells in the rabbit retina," *J. Comp. Neurol.*, vol. 519, no. 13, pp. 2509–2521, 2011.

[75] R. L. Pfeiffer, R. E. Marc, M. Kondo, H. Terasaki, and B. W. Jones, "Müller cell metabolic chaos during retinal degeneration," *Exp. Eye Res.*, vol. 150, pp. 62–70, 2016.

[76] R. W. Thompson, G. D. Barnett, M. S. Humayun, and G. Dagnelie, "Facial recognition using simulated prosthetic pixelized vision," *Invest. Ophthalmol. Vis. Sci.*, vol. 44, no. 11, pp. 5035–5042, 2003.

[77] S. Shah, A. Hines, D. Zhou, R. J. Greenberg, M. S. Humayun, and J. D. Weiland, "Electrical properties of retinal–electrode interface," *J. Neural Eng.*, vol. 4, no. 1, pp. S24–S29, 2007.

[78] R. Wilke, G. K. Moghadam, N. Lovell, G. Suaning, and S. Dokos, "Electric crosstalk impairs spatial resolution of multi-electrode arrays in retinal implants," *J. Neural Eng.*, vol. 8, no. 4, pp. 1–11, 2011.

[79] C. J. Cela, K. Loizos, and G. Lazzi, "Virtual electrodes: Increasing spatial resolution of neural interfaces beyond the actual electrode count," in *URSI Natl. Radio Sci. Conf.*, 2012.

[80] I. Cassar, T. Davis, Y.-K. Lo, and W. Liu, "A virtual electrode through summation of time offset pulses," *J. Med. Health Biomed. Pharm. Eng.*, vol. 8, no. 9, 2014.

[81] J. K. Mueller and W. M. Grill, "Model-based analysis of multiple electrode array stimulation for epiretinal visual prostheses," *J. Neural Eng.*, vol. 10, no. 3, pp. 1–13, 2013.

[82] B. W. Sheasby and J. F. Fohlmeister, "Impulse encoding across the dendritic morphologies of retinal ganglion cells," *J. Neurophysiol.*, vol. 81, no. 4, pp. 1685–1698, 1999.

[83] D. Ropireddy, R. Scorcioni, B. Lasher, G. Buzsáki, and G. A. Ascoli, "Axonal morphometry of hippocampal pyramidal neurons semi-automatically reconstructed after in-vivo labeling in different CA3 locations," *Brain Struct. Funct.*, vol. 216, no. 1, March 2011.

[84] D. Ropireddy, S. E. Bachus, and G. A. Ascoli, "Non-homogeneous stereological properties of the rat hippocampus from high-resolution 3D serial reconstruction of thin histological sections," *Neurosci.*, vol. 205, pp. 91–111, 2012.

[85] G. A. Johnson, E. Calabrese, A. Badea, G. Paxinos, and C. Watson, "A multidimensional magnetic resonance histology atlas of the rat brain," *Neuroimage*, vol. 62, no. 3, pp. 1848–1856, September 2012.

[86] C. Bingham, K. Loizos, Y. Guo, G. J. Yu, P. Hendrickson, J.-M. C. Bouteiller, G. Lazzi, and T. Berger, "Multi-scale simulation of extracellular electrode stimulation in the dentate gyrus," in *Soc. Neurosci. Conf.*, Washington D. C., 2013.

[87] L. López-Aguado, J. Ibarz, and O. Herreras, "Activity-dependent changes of tissue resistivity in the ca1 region in vivo are layer-specific: modulation of evoked potentials," *Neurosci.*, vol. 108, no. 2, pp. 249–262, 2001.

[88] H. Xu, M. Hsiao, D. Song, and T. W. Berger, "Recording place cells from multiple sub-regions of the rat hippocampus with a customized micro-electrode array," in *Proc. IEEE 36th Eng. Med. Biol. Soc. Conf.*, Chicago, Il, 2014.

[89] P. Poirazi, T. Brannon, and B. W. Mel, "Arithmetic of subthreshold synaptic summation in a model CA1 pyramidal cell," *Neuron*, vol. 37, no. 6, pp. 977–987, 2003.

[90] C. P. Taylor and F. E. Dudek, "Excitation of hippocampal pyramidal cells by an electrical field effect," *J. Neurophysiol.*, vol. 52, no. 1, pp. 126–142, 1984.

[91] C. A. Anastassiou, R. Perin, H. Markram, and C. Koch, "Ephaptic coupling of cortical neurons," *Nat. neurosci.*, vol. 14, no. 2, pp. 217–223, 2011.

[92] H. Bokil, N. Laaris, K. Blinder, M. Ennis, and A. Keller, "Ephaptic interactions in the mammalian olfactory system," *J. Neurosci.*, vol. 21, pp. 1–5, 2001.

[93] C. J. Cela and G. Lazzi, "Numerical prediction of neural activation in electrically stimulated retina," *Proc. ATEM/URSI 13th Intl. Symp.*, pp. 9–11, 2009.